On the Prediction of Macrosegregation in Vacuum Arc Remelted Ingots

K. Mramor, T. Quatravaux, H. Combeau, Alain Jardy, Miha Založnik, I. Crassous, A. Gaillac

On the prediction of macrosegregation in Vacuum Arc Remelted ingots

K. Mramor[a] , T. Quatravaux[a*], H. Combeau[a], A. Jardy [a], M. Založnik[a], I. Crassous[b], A. Gaillac[b]

[a] Institut Jean Lamour – UMR 7198 CNRS/Université de Lorraine, Laboratory of Excellence DAMAS, Campus ARTEM, 2 allée André Guinier, BP 50840, F-54011 NANCY, France

[b] Framatome, Components Research Center, Avenue Paul Girod, F-73403 UGINE, FRANCE

*corresponding author: thibault.quatravaux@univ-lorraine.fr, +33 (0)372742900

katarina.mramor@fs.uni-lj.si, herve.combeau@univ-lorraine.fr, alain.jardy@univ-lorraine.fr, miha.zaloznik@univ-lorraine.fr, isabelle.crassous@framatome.com, alexis.gaillac@framatome.com

Abstract

The chemical homogeneity and metallurgical structure of vacuum arc remelted (VAR) zirconium ingots are directly responsible for product quality. It is therefore important to understand the relationship between these properties and the operating conditions. An in-depth analysis of the modelling of solidification phenomena during the VAR was carried out.

Such model, solves a coupled set of transient equations for heat, momentum, solute transport and turbulence in an axisymmetric geometry. The remelting and cooling of a cylindrical ingot are calculated for time-dependent operating parameters.

The solidification mechanisms implemented in the model can be applied to multi-component industrial alloys such as Zircaloy-4, which provides information on the macrosegregation phenomena studied in this paper.

The model results were validated, based on the remelting of a specially designed chemically homogeneous Zircaloy-4 electrode. The results illustrate the importance of thermal

and solute convection, the importance of the permeability of the partially solid material and the weak influence of nuclei density and solute diffusion in the solid phase on the prediction of macrosegregation in Zircaloy-4 ingots.

Keywords: Numerical solution; Solidification; Zirconium alloys; Macrosegregation; Vacuum Arc Remelting, Secondary Metallurgy

Nomenclature

B	magnetic field (T)
D	diffusion coefficient of solute in the liquid or the solid phase ($m^2.s^{-1}$)
F_{el}	electromagnetic force (N)
g	gravitational acceleration ($m.s^{-2}$)
g_l	volume fraction of the liquid phase
g_s	volume fraction of the solid phase
h	specific enthalpy ($J.kg^{-1}$)
J	melting current density ($A.m^{-2}$)
J	interfacial species transfer rate per unit volume ($kg.m^{-3}.s^{-1}$)
J^{ji}	interfacial species transfer rate per unit volume due to diffusion ($kg.m^{-3}.s^{-1}$)
$J^{\Gamma i}$	interfacial species transfer rate per unit volume due to the phase change ($kg.m^{-3}.s^{-1}$)
k	turbulent kinetic energy ($m^2.s^{-2}$)
K	permeability (m^2)
K_0	permeability constant of the Blake-Kozeny law (m^2)
N_0	nuclei density (m^{-3})
N_g	grain density (m^{-3})

48	p	pressure (Pa)
49	$\bar{\mathbf{u}}_\mathbf{l}$	average velocity of the liquid phase ($m.s^{-1}$)
50	Pr_t	turbulent Prandtl number
51	Sc_t	turbulent Schmidt number
52	**u'**	turbulent velocity of the liquid metal ($m.s^{-1}$)
53		
54	*Greek symbols*	
55	β_S	solutal expansion coefficient ($wt\%^{-1}$)
56	β_T	thermal expansion coefficient (K^{-1})
57	ε	dissipation rate of turbulent kinetic energy ($m^2.s^{-3}$)
58	λ	thermal conductivity ($W.m^{-1}.K^{-1}$)
59	λ_{DAS}	characteristic length of the dendritic structure (m)
60	μ	dynamic viscosity ($kg.m^{-1}.s^{-1}$)
61	σ	electric conductivity ($\Omega^{-1}.m^{-1}$)
62	φ	electric potential (V)
63	ρ	density ($kg.m^{-3}$)
64	ω	solute mass fraction (wt%)
65	Φ	mass production rate per unit volume due to nucleation ($kg.m^{-3}.s^{-1}$)
66	Γ	interfacial phase change rate per unit volume ($kg.m^{-3}.s^{-1}$)
67	*Subscripts*	
68	g	grain density (m^{-3})
69	l	liquid
70	m	mixture

r	radial direction
s	solid
t	turbulent
z	axial direction
θ	orthoradial direction

1 Introduction

The fuel assembly components, including Zirconium alloys, are one of the key elements in the production process in nuclear reactors. Refinement of the metallurgical structure and improvement of the cleanness of Zr alloy ingots are generally achieved by the Vacuum Arc Remelting (VAR) process. The high quality and good performance of the final product are ensured by this manufacturing process, which enables the regulation of the chemical homogeneity

The VAR process, as illustrated in Fig. 1, consists in continuously remelting a consumable electrode. In order to obtain a high quality structural ingot, the composition of the electrode must comply with strict standards. A high power direct current, applied under vacuum, provides an electric arc between the tip of the electrode and the baseplate of a water-cooled copper mold. The intense heat generated by the arc melts the electrode tips that fall into the crucible. The secondary ingot is gradually formed from the liquid metal that falls through the arc plasma. The secondary ingot consists of a liquid metal pool above the solidified part and a mushy zone where solidification takes place.

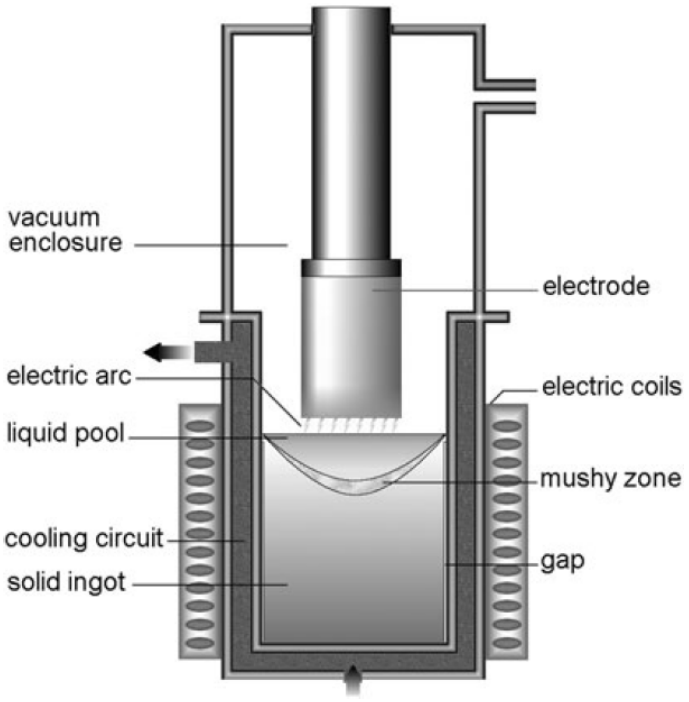

Fig. 1. Schematic representation of a VAR furnace.

In addition, VAR is generally used in the remelting cycles of high quality special steels, as well as Nickel and Titanium alloys.

In the case of Zr or Ti remelting, the arc length is several centimeters. To prevent side-arcing due to these operating conditions, an axial magnetic field is generated by external induction coils. A periodical reversal of the coil current creates a magnetic field that can provide complex electromagnetic stirring of the melt pool. For the standard production of superior-quality Zr alloys for nuclear applications, a VAR operation cycle is applied (up to three times), where each secondary ingot feeds the next remelting as a new consumable electrode.

During solidification, chemical heterogeneities eventually appear in the mushy zone. One of the main challenges in the production of Zr alloys is to control macrosegregation in the VAR process for an optimal quality of the final ingots. Macrosegregation refers to chemical

heterogeneity at the ingot scale and is a combination of microsegregation, i.e. concentration gradient between the solid and liquid phases at the dendritic microscale, and the solute convective transport caused by the liquid metal flow within the mushy zone.

Several numerical models have already been developed to calculate the hydrodynamics of the melt pool in a VAR ingot, including the 2D SOLAR code, as described by Jardy and Ablitzer[1]. The extension of this CFD code forms the basis for the present study.

In addition, an extensive work has also been done to anticipate solidification defects in the remelting products. The SOLAR code was successfully used for simulating VAR and ESR (ElectroSlag Remelting) processes, to predict the risks of white spot and freckle occurrence in the ingot, using a Rayleigh number criterium[2]. The numerical results highlighted the positive impact of an optimized melting rate to minimize the occurrence of freckles.

Wilson and Jardy[3] used the SOLAR model to determine the influence of the alternated electromagnetic stirring sequence on the remelting of Titanium alloys. They presented in-depth numerical studies on several magnetic field stirring patterns during remelting. These numerical results were lately validated by Venkatesh et al.[4] with an industrial campaign dedicated to the remelting of Titanium alloys. The numerical results were successfully validated, based on the measured positions of tungsten markers inside the ingots, providing cavity locations and liquid pool depth for different stirring sequences.

Besides, Chapelle et al.[5] determined the effect of electromagnetic stirring on melt pool free surface dynamics during the remelting of a Zirconium alloy. They observed the behavior of the free surface of the pool for undirectional and alternated stirring. They thus showed that the free surface deformation can affect the quality of the surface of the VAR ingot.

From all these previous studies, it is now well established that the sources of in-place (r, z) motion of the molten pool of a VAR ingot are:

- thermal convection (buoyancy force due to thermal gradients) which tends to favour a flow in a clockwise direction (symmetry axis being on the left),
- the Lorenz force resulting from the interaction between the melting current and the self-induced magnetic field that causes a counterclockwise flow,
- the centrifugal force resulting from the azimuthal motion caused by the interaction between the melting current and the external stirring field. The latter generates a clockwise flow in the (r,z) plane.

Moreover, Revil-Baudard et al.[6] identified the additional potential effect of solute-driven buoyancy force resulting from microsegregation, on macrosegregation.

This paper presents the recent implementation of an improved solidification modelling, based on work of Combeau et al.[7], to provide an enhanced description of macrosegregation phenomena in the ingot.

2 Full-scale VAR trial

For this study, a 2.6 ton Zircaloy-4 (Zy4: Zr-1.3Sn-0.2Fe-0.1O-0.1Cr) VAR ingot of standard size was processed at the Framatome plant (Ugine, France). First, a dedicated electrode was entirely manufactured from recycled materials of the same grade, in order to avoid any chemical heterogeneity. It was noticeable that the mechanical strength of this electrode made of scraps was sufficient throughout the remelting process, so that the trial was carried out without any technical hitch.

The actual recordings of a highly non-standard melting sequence are presented in Figs. 2 and 3, in terms of melting rate and stirring coil current. During the trial, the stirring sequence was carried out in two successive steps: a strong alternating stirring was used to remelt the first 60 %

of the electrode, followed by a weak continuous stirring until the end of the melting process. The magnitude of the alternating stirring was about 4.5 times higher than the continuous stirring one.

Additionally, a strong continuous stirring has been briefly applied at three moments during the alternated stirring stage, in order to mark different pools in the ingot, as such temporary change caused a local change in the grain structure of the solidified material. The profiles of the marked melt pool are clearly visible on calculated composition maps presented in figure 3.c.

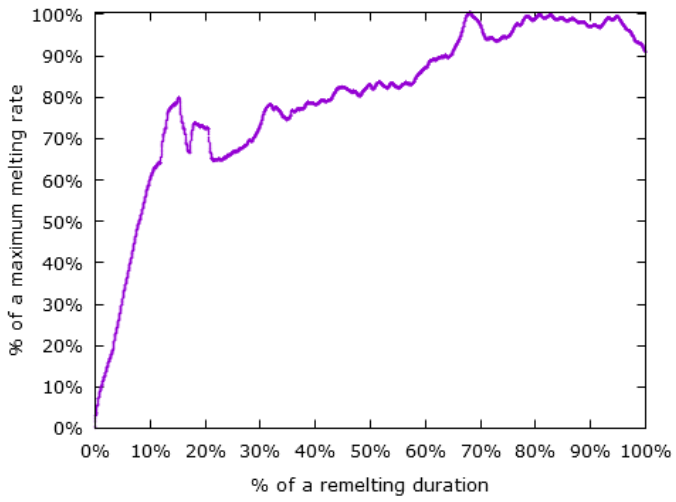

Fig. 2. Melting rate of the full-scale Zy4 remelting trial.

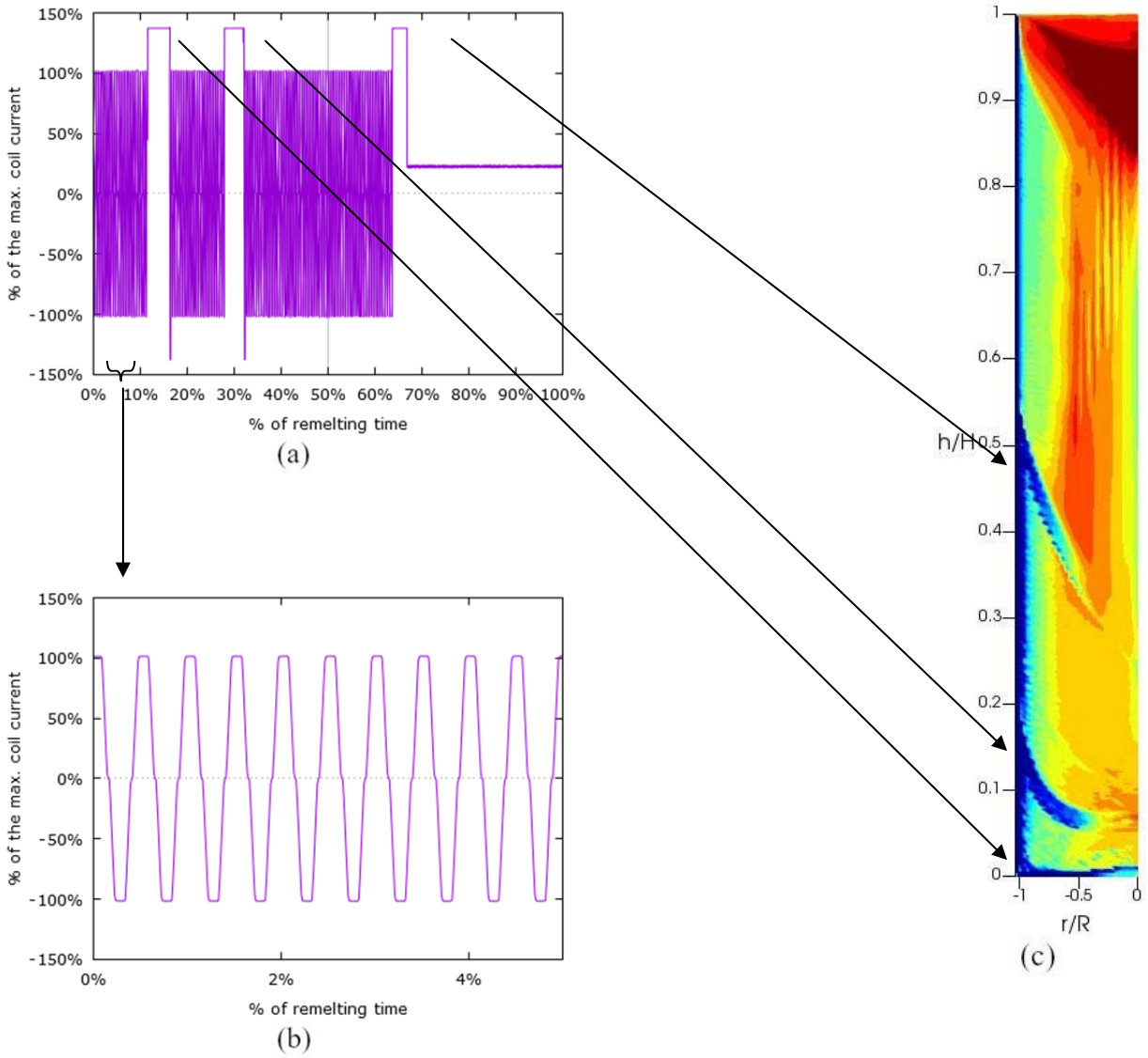

160 **Fig. 3**. Stirring sequence of the full-scale Zy4 remelting trial. (a) Coil current throughout the
161 melt. (b) Detailed alternating stirring sequence. (c) Example of a computed composition map (Zr
162 content), highlighting the melt pool markings in the remelted ingot.

163

164 The remelted ingot was cut longitudinally along its entire length in order to perform
165 chemical analyses and characterize the grain structure. Furthermore, chemical analyses were
166 carried out along several radii at different heights of the ingot, ranging from 0.25 H to 0.88 H,

where H is the total height of the ingot. These measurements are used in section 4 to validate the numerical results.

3 SOLAR model description

3.1 The CFD macromodel

As discussed in section 1, SOLAR is a 2D axisymmetric finite volume model of the VAR process, with the complete set of macroscopic equations presented in Table 1. At a macroscopic scale, the model (Eqs. (1 to 19)) takes into account the transport of heat and solutes coupled with the turbulent flow driven by the electromagnetic stirring, as well as thermal and solute natural convection.

The electromagnetic force $\boldsymbol{F}$ results from the interaction between the melting current $\boldsymbol{J}$, and the magnetic field $\boldsymbol{B}$**.** The latter includes the self-induced magnetic field $B_\theta \boldsymbol{e}_\theta$, and the magnetic field created by the external induction coils $B_{z,ext}\boldsymbol{e}_z$. The current density is in turn calculated from Laplace's conservation equation (Eq. 8) and Ohm's law (Eq. 11). It is important to note that the effect of EM stirring on the free surface dynamics is not considered here, in accordance with the results of Chapelle et al.[5], who show a second-order effect of EM stirring on the deformation of the melt pool free surface. Thermal buoyancy and solutal buoyancy are taken into account by using a conventional Boussinesq approximation (Eq. 12) to describe the variations in density of the liquid phase in the gravity term of the momentum balance equation. In the mushy zone, the solid phase forms a porous matrix, modelled by a Darcy term in the momentum equation (Eq. 4). Permeability is estimated by the Blake-Kozeny law (Eq. 13), where the Asai and Muchi formula is used to describe the permeability constant K_0 (Eq. 17).

190

191 **Table 1.** Main constitutive equations of the CFD macromodel

Averaged total mass balance
$\frac{\partial}{\partial t}(\rho_m) + \nabla \cdot (\rho_l g_l \overline{\boldsymbol{u_l}}) = 0$ (1)
Averaged mass balance of the solid phase
$\frac{\partial}{\partial t}(\rho g_s) = \Gamma_s + \Phi_s\,, \qquad \rho = const$ (2)
Averaged total heat balance
$\frac{\partial}{\partial t}\left(\rho g_s \overline{h_s} + \rho g_l \overline{h_l}\right) + \nabla \cdot \left(\rho g_l \boldsymbol{u_l} \overline{h_l}\right) = \nabla \cdot [(\lambda + g_l \lambda_t) \nabla \bar{T}]$ (3)
Averaged momentum balance for the liquid phase: fluid flow
$\frac{\partial}{\partial t}(\rho g_l \overline{\boldsymbol{u_l}}) + \nabla \cdot (\rho g_l \overline{\boldsymbol{u_l}}\,\overline{\boldsymbol{u_l}}) = -g_l \nabla p^* + \nabla \cdot [(\mu + \mu_t) g_l (\nabla \overline{\boldsymbol{u_l}} + (\nabla \overline{\boldsymbol{u_l}})^T)] - \frac{g_l^2 \mu}{K} \overline{\boldsymbol{u_l}} + g_l \boldsymbol{g} \overline{\rho_l^b} + g_l \boldsymbol{F}_{\mathbf{el}}$ (4)
Averaged solute mass balance for species i in the solid phase
$\frac{\partial}{\partial t}\left(\rho g_s \overline{\omega_s^i}\right) = J_s^{j^i} + J_s^{\Gamma^i}$ (5)
Averaged solute mass balance for species i in the liquid phase
$\frac{\partial}{\partial t}\left(\rho g_l \overline{\omega_l^i}\right) + \nabla \cdot \left(\rho g_l \overline{\boldsymbol{u_l}}\,\overline{\omega_l^i}\right) = \nabla \cdot \left[\left(D_l^i + D_t\right) g_l \nabla \overline{\omega_l^i}\right] + J_l^{j^i} + J_l^{\Gamma^i}$ (6)
Averaged $k - \varepsilon$ turbulence model

$$\frac{\partial}{\partial t}(\rho g_l k) + \nabla \cdot (\rho g_l \boldsymbol{u_l} k) = \nabla \cdot \left[\left(\mu + \frac{\mu_t}{\sigma_k}\right) g_l \nabla k\right] + P_k + D_k + G_k^T + G_k^S - \rho g_l \varepsilon \tag{7}$$

$$\frac{\partial}{\partial t}(\rho g_l \varepsilon) + \nabla \cdot (\rho g_l \boldsymbol{u_l} \varepsilon)$$

$$= \nabla \cdot \left[\left(\mu + \frac{\mu_t}{\sigma_\varepsilon}\right) g_l \nabla \varepsilon\right] + \frac{\varepsilon}{k}[c_1 P_k + c_2 D_k + c_1 c_3 (G_k^T + G_k^S) - c_2 \rho g_l \varepsilon]$$

Laplace conservation equation

$$\nabla^2 \varphi = 0 \tag{8}$$

Mass balance equation at the solid-liquid interface

$$\Gamma_s + \Gamma_l = 0 \tag{9}$$

Solute mass balance at the solid-liquid interface

$$J_s^{j^i} + J_s^{\Gamma^i} + J_l^{j^i} + J_l^{\Gamma^i} = 0 \tag{10}$$

Ohm's law and Lorentz force

$$\boldsymbol{J} = -\sigma \nabla \varphi \qquad \boldsymbol{F_{el}} = \boldsymbol{J} \wedge \boldsymbol{B} = -J_z B_\theta \boldsymbol{e_r} + J_r B_{ext,z} \boldsymbol{e_\theta} + J_r B_\theta \boldsymbol{e_z} \tag{11}$$

Liquid density in the buoyancy force

$$\overline{\rho_l^b} = \rho_{ref}[1 - \beta_T(\overline{T} - T_{ref}) - \sum_i \beta_S^i(\overline{\omega_l^i} - \omega_{ref}^i)] \tag{12}$$

Permeability law

$$K = \frac{g_l^3}{(1 - g_l^2)} K_0 \tag{13}$$

Production rate P_k due to gradients of u_l and dissipation rate D_k due to liquid-solid interaction

$$P_k = -\rho g_l \overline{\boldsymbol{u_i'} \boldsymbol{u_j'}} \frac{\partial}{\partial x_j}(g_l \overline{u_i}) \qquad D_k = -\frac{2\mu g_l^2}{K} k \tag{14}$$

Generation rate due to thermal and solutal buoyancy

$$G_k^T = \beta_T g_l \frac{\mu_t}{Pr_t}\, \boldsymbol{g} \cdot \nabla \overline{T} \qquad G_k^S = \sum_i \beta_S^i g_l \frac{\mu_t}{Sc_t}\, \boldsymbol{g} \cdot \nabla \overline{\omega_l}^i \tag{15}$$

Macroscopic $k-\varepsilon$ model constants

$$Pr_t = 0.85 \quad \sigma_k = 1.0 \quad c_\mu = 0.09 \quad c_3 = \tanh\left(\frac{|\overline{\boldsymbol{u}_{l,z}}|}{\sqrt{\overline{\boldsymbol{u}_{l,\theta}}^2 + \overline{\boldsymbol{u}_{l,r}}^2}}\right) \tag{16}$$

$$Sc_t = 0.7 \quad \sigma_\varepsilon = 1.3 \quad c_1 = 1.44$$

$$c_2 = 1.92$$

Permeability constants of the model

$$K_0 = \frac{\lambda_{DAS}^2}{180} \tag{17}$$

Pressure

$$p^* = \overline{p}_l + \frac{2}{3}\rho k \tag{18}$$

Turbulent parameters

$$\mu_t = c_\mu \rho \frac{k^2}{\varepsilon} \qquad \lambda_t = \frac{c_p \mu}{Pr_t} \qquad D_t = \frac{\mu_t}{\rho Sc_t} \tag{19}$$

A macroscopic RANS two-equation $k-\varepsilon$ model (Eq. 7) is adopted to describe the turbulence of the liquid flow. The transport equations for the mean turbulent kinetic energy k and its corresponding mean dissipation rate ε include:

- turbulence production due to mean velocity gradients P_k (Eq. 14),
- dissipation of turbulence due to the liquid/solid interaction in the mushy zone D_k (Eq. 14),
- production or dissipation of turbulence caused by vertical thermal G_k^T and solute content G_k^S gradients (Eq. 15).

The constants used for closure (Eq. 16) correspond to the standard $k-\varepsilon$ model originally developed by Launder and Spalding[8] for a fully liquid medium ($g_l = 1$, hence $K \to \infty$). This approach is suitable for a wide variety of turbulent flows.

The closure of such model in the mushy zone, considered as a porous medium, is solved through the formulation of the dissipation term D_k of the turbulence model [9–12]. Precisely, the Prescott and Incropera approach was implemented in the model (eq. 14).

The model simulates the direct radiation of the electric arc by the implementation of a heat source as well as a current density on the top face of the secondary ingot.

All boundary conditions are discussed in the PhD theses by Hans[13], Quatravaux[14] and Revil-Baudard[15].

The mesh used for all simulations reported in this paper is a structured one. The number of cells must increase during the simulation to follow the ingot growth, as the material input from the electrode melting is modeled by an advection-like term, i.e. a cell split and growth method. The resulting mesh is scalable, both in size and number of cells, describing at each time step the ingot growth in a continuous way. More details are available in Quatravaux's Ph D thesis[14].

3.2 The solidification micromodel

The solidification micromodel is derived from the approach of Beckerman and Viskanta[16]. They proposed a mathematical formulation for dendritic solidification in a binary mixture. Their micro-model was based on a two-phase volume-averaged formulation and results were compared to shadowgraph images of the experimental solidification of an ammonium chloride solution in water. Although the numerical results were qualitatively close to

221 experimental measurements, the quantitative values for temperature and concentrations showed
222 considerable differences.

223 Lately, an improved model was presented by Wang and Beckerman[17]. They described
224 equiaxed dendritic solidification by considering the convection and solid phase transport. This
225 model accounts for the nucleation, grain growth and dendrite morphology by solving a set of
226 transport equations for solid, interdendritic, and extradendritic phases. However, the model was
227 only validated at the laboratory scale.

228 A similar approach, based on decoupling physical phenomena according to the micro and
229 macro time-scale, was presented by Zaloznik and Combeau[18] for a real industrial size ingot. The
230 constitutive equations of the models were obtained by introducing a Representative Elementary
231 Volume (REV), averaging the transport equations of heat, mass, and momentum over the
232 individual (liquid, solid) phases. The process model considers mass transfer, turbulent fluid flow,
233 heat transfer, electromagnetism and phase change using the following main assumptions:
234 - the local thermal equilibrium is assumed in each mesh cell, which behaves as a REV;
235 - the solidification shrinkage is not considered, because the densities of both phases are equal and
236 constant, except for the buoyancy terms where the Boussinesq approximation is applied;
237 - the solid phase is considered rigid and fixed;
238 - the thermophysical properties of all alloys are constant; in particular, partition coefficients and
239 liquidus slopes are independent of the temperature and composition.

240 An operator splitting scheme, described in detail in Založnik and Combeau[18], was used
241 to define the transport and growth stages. In the first one, the convective/diffusive macroscopic
242 transport partial differential equations were solved globally by neglecting nucleation and growth
243 terms, while in the second one, the contributions of nucleation and growth were solved locally
244 and initialized from the transport stage. The grain growth model was highly nonlinear and

therefore required special attention. The advantage of this approach was the decoupling of macro and micro time scales, which allows the grain growth model to be solved separately.

The microscopic terms that described the grain nucleation and growth were treated locally within each mesh cell where the interfacial chemical and thermal equilibrium were assumed to be reached: $T_s = T_l = T$ and $\omega_s^{i^*} = k_p \omega_l^{i^*}$. The interfacial compositions and temperatures are correlated by considering a simplified multicomponent phase diagram, where the liquidus temperature is described with a linear dependence on all alloy components. Both the liquidus slopes m_l^i and partition coefficient k_p^i are constant. Therefore, the solidification process starts when the enthalpy of a cell falls below the liquidus enthalpy h_{liq},

$$h_{liq} = c_p\left(T_m + \sum_{i=1}^{n_{sol}} m_L^i \omega_l^i\right) + L_f \tag{20}$$

and stops when the temperature drops below a fixed temperature T_{sol0} or when the solid fraction reaches $g_s = 1$ due to the primary growth as explained by Založnik and Combeau[18].

In the solidification interval, where the liquid and solid phases co-exist in the same REV ($0 < g_s < 1$), the solidification micromodel takes into account finite solute diffusion in both phases and considers two separate regions: the solid phase and the extra-dendritic liquid. In the mushy zone, grains are assumed to be spherical, the velocity of the extra-dendritic phase to be equal to the averaged velocity of the liquid, and the diffusivity of each solute to be constant in each phase. Grain generation is modelled by an instantaneous nucleation model, which assumes that a predefined number of grains per unit volume N_g with an initial radius R^* nucleate when the local temperature becomes lower than the local liquidus temperature (see Eq. 25 in Table 2). The

transfer of the interfacial solute due to the phase change (solidification or melting) is given in Eq. 21:

$$\left(k_p^i - 1\right)\omega_l^{i*}\frac{\Gamma_s}{\rho} + \omega_l^{i*}\left(\frac{S_v D_l^n}{\delta_l} + k_p^n\frac{S_v D_s^n}{\delta_s}\right) = \omega_l^i\frac{S_v D_l^n}{\delta_l} + \omega_s^i\frac{S_v D_s^n}{\delta_s}. \quad (21)$$

During primary solidification, the diffusion flux at the solid/liquid interface is described by a simplified model: solute gradients are calculated by dividing the difference of the solute mass fraction at the interface $\omega_k^{*,i}$ and the average mass fraction ω_k^i, by a diffusion length δ_k. An approximation is used to estimate the boundary layer thickness in the solid phase while a stagnant film model is used to describe the boundary layer thickness in the liquid phase. This solidification micromodel, whose main equations are given in Table 2 (Eqs. 22-28), is described in detail by Tveito et al.[19]. It must be stated here that its implementation in SOLAR software represents an innovative approach over the previous versions used to simulate the VAR process.

Table 2. Main equations of the solidification micromodel.

Geometrical relations and surface area
$R^* = \left(\frac{3g_s}{4\pi N_g}\right)^{\frac{1}{3}}$ $\quad R_f = \left(\frac{3}{4\pi N_g}\right)^{\frac{1}{3}}$ $\quad S_v^* = 4\pi R^{*2} N_g$ (22)
Dendrite tip kinetics
$\Omega_i = \frac{\omega_l^{*,i} - \left[<\omega_s^i>^e\right]^{gr}}{\omega_l^{*,i}\left(1 - k_p^i\right)}$ $\quad V = \frac{\partial R^*}{\partial t}$ $\quad \Gamma_s = \rho_s S_v^* V$ (23)
Boundary layer thickness

$$\delta_i^l = \frac{d_i}{\left(\frac{d_i}{R^*} - \frac{f(R^*,\Delta_i)+g(R_f,R^*,\Delta_i)}{d_i(R^*+d_i-(R^*-\Delta_i+d_i)exp^{-\frac{\Delta_i}{d_i}})-f(R^*,\Delta_i)+(exp^{-\frac{\Delta_i}{d_i}}-1)g(R_f,R^*,\Delta_i)}\right)} \quad (24)$$

$$\delta_i^s = \frac{R^*}{5} \qquad g\left(R_f,R^*,\Delta_i\right) = \frac{R_f^3-(R^*+\Delta_i)^3}{3(R^*+\Delta_i)} \qquad d_i = \frac{D_l^i}{V}$$

$$Sh_i = \frac{2}{3(1-g_s)} Sc_i^{\frac{1}{3}} Re^{n(Re)} \qquad f(R^*,\Delta_i) = \frac{1}{2}((R^*+\Delta_i)^2-(R^*)^2) \qquad \Delta_i = \frac{2R^*}{Sh_i}$$

$$Re = \frac{\rho_l(1-g_s)2R^*}{\mu_l}|\overline{\boldsymbol{u_l}}| \qquad n(Re) = \frac{2Re^{0.28}+4.65}{3(Re^{0.28}+4.65)} \qquad Sc_i = \frac{\mu_l}{\rho_l D_l^i}$$

Thermodynamics

$$\omega_{s-d}^{*,i} = \omega_l^{*,i} k_p^i \qquad T_l = T_m + \sum_i m_l^i \omega_l^{*,i} \quad (25)$$

Nucleation

$$\Phi_s = \begin{cases} \rho \frac{\pi R^{*3}}{6} N_g \delta(t-t_0); \text{ if } T_l < T_m + \sum_i m_l^i \omega_l^{*,i} \text{ and } g_s = 0 \\ 0; \text{ else} \end{cases} \qquad \Phi_s = -\Phi_l \quad (26)$$

Solute fluxes due to phase change

$$J_s^{\Gamma^i} = \omega_s^{*,i}\Gamma_s \qquad J_l^{\Gamma^i} = \omega_l^{*,i}\Gamma_l \qquad \omega_s^{*,i} = k_p^i \omega_l^{*,i} \quad (27)$$

Solute fluxes due to diffusion

$$J_s^{j,i} = \frac{S_v^* \rho_s D_s^i}{\delta_s}(\omega_s^{*,i} - \omega_s^i) \qquad J_l^{j,i} = \frac{S_v^* \rho_l D_l^i}{\delta_l}(\omega_l^{*,i} - \omega_l^i) \quad (28)$$

4 Numerical results and discussion

The full-scale melt of a Zy4 electrode (see Section 2) was simulated using the model fully described in Section 3. A complete set of process operating parameters (melting rate, arc voltage, melting current and current in the external induction coils) was previously recorded during the

282 industrial trial to feed all simulations presented in this section. The operating parameters were
283 entered by means of data files containing these records (see Figures 2 and 3).

284 The thermophysical properties of Zy4 used in the simulations are given in Table 3. Note
285 that the solidification properties (partition coefficients and liquidus slopes) have been extracted
286 from the binary phase diagrams for Zr-X alloys[20]. Unless otherwise specified, the values of β_S^{Sn}
287 and λ_{DAS} used in the simulations (default values) are also reported in Table 3.

288

289

290 **Table 3.** Thermophysical properties of Zy4 used in the simulations

Nominal compositions	Sn	ω_0^{Sn}	[wt%]	1.3
	Fe	ω_0^{Fe}	[wt%]	0.2
	O	ω_0^{O}	[wt%]	0.1
	Cr	ω_0^{Cr}	[wt%]	0.1
Melting temperature of pure Zr		T_m	[°C]	1855
Liquidus slopes	Sn	m_l^{Sn}	[°C(wt%)$^{-1}$]	-11
	Fe	m_L^{Fe}	[°C(wt%)$^{-1}$]	-57
	O	m_L^{O}	[°C(wt%)$^{-1}$]	147
	Cr	m_L^{Cr}	[°C(wt%)$^{-1}$]	-26
Partition Coefficients	Sn	k_p^{Sn}	[-]	0.27
	Fe	k_p^{Fe}	[-]	0.25
	O	k_p^{O}	[-]	2.32

	Cr	k_p^{Cr}	[-]	0.15
Diffusion coefficients in the liquid	Sn	D_l^{Sn}	[$m^2.s^{-1}$]	$1 \cdot 10^{-8}$
	Fe	D_l^{Fe}	[$m^2.s^{-1}$]	$1 \cdot 10^{-8}$
	O	D_l^{O}	[$m^2.s^{-1}$]	$1 \cdot 10^{-8}$
	Cr	D_l^{Cr}	[$m^2.s^{-1}$]	$1 \cdot 10^{-8}$
Diffusion coefficients in the solid	Sn	D_s^{Sn}	[$m^2.s^{-1}$]	$4.9 \cdot 10^{-11}$
	Fe	D_s^{Fe}	[$m^2.s^{-1}$]	$1.5 \cdot 10^{-9}$
	O	D_s^{O}	[$m^2.s^{-1}$]	$3.8 \cdot 10^{-9}$
	Cr	D_s^{Cr}	[$m^2.s^{-1}$]	$1.3 \cdot 10^{-9}$
Temp. of end of solidification		T_{sol}	[°C]	1592
Latent heat		L_f	[$J.kg^{-1}$]	$2.42 \cdot 10^{5}$
Reference density		ρ_0	[$kg.m^{-3}$]	6210
Dynamic viscosity		μ	[Pa.s]	$4.59 \cdot 10^{-3}$
Thermal conductivity		λ	[$W.m^{-1}.°C^{-1}$]	36.5
Thermal expansion coefficient		β_T	[$°C^{-1}$]	$4 \cdot 10^{-5}$
Specific heat		c_p	[$J.kg^{-1}.°C^{-1}$]	435
Electric conductivity		σ	[$m^{-1}.\Omega^{-1}$]	$6.8 \cdot 10^{5}$
Solute expansion coefficients	Sn	β_S^{Sn}	[$(wt\%)^{-1}$]	$3 \cdot 10^{-2}$
	Fe	β_S^{Fe}	[$(wt\%)^{-1}$]	0
	O	β_S^{O}	[$(wt\%)^{-1}$]	0
	Cr	β_S^{Cr}	[$(wt\%)^{-1}$]	0
Characteristic length of the		λ_{DAS}	[m]	$134 \cdot 10^{-6}$

dendritic structures

For all simulations reported in the present paper, the average cell size was approximately 9 mm wide and 6 mm height. Mesh refinement was applied with a geometrical reason of 0.8 on the five nodes closest to the mold as well as to the free surface. The time-step was fixed to 0.025 s.

The computational time required for simulating a full melt depends on the computer. In the IJL facility, the total CPU time was around 72 hours.

In several previous publications [2,21–23], the authors have detailed some CFD macromodel results when applied to various remelting situations. In this paper, the attention will be focused on the fluid flow in the liquid pool and the mushy zone, as well as the resulting macrosegregation.

4.1 Hydrodynamics in the liquid metal pool

The purpose of this section is to numerically study the influence of the thermal and solutal buoyancy forces on the flow in the liquid bath during remelting. Mean velocity field, turbulence generation are therefore investigated. Only the effect of local Sn content on solutal buoyancy was considered, as the concentrations in all other alloying elements are negligible.

4.1.1. Assumptions on the thermal and solutal buoyancy forces

During solidification, a buoyancy driving force can be generated either by the thermal or solutal buoyancy effects, that can be collaborating or opposing [24]. Both buoyancy effects are modelled by the Boussinesq approximation (Eq. 12), therefore both the thermal and the solutal expansion coefficients had to be estimated.

Unfortunately, values for the solutal and thermal expansion coefficient for Zy-4 alloy and its alloying elements are not readily available in the literature.

The thermal expansion has been estimated from values measured by Paradis and Rhim[25] on pure Zr. Moreover, other pertaining physical properties, such as reference density, come from this reference.

Figures 4 and 5 below show the evolution of Zr density and Sn density with the temperature.

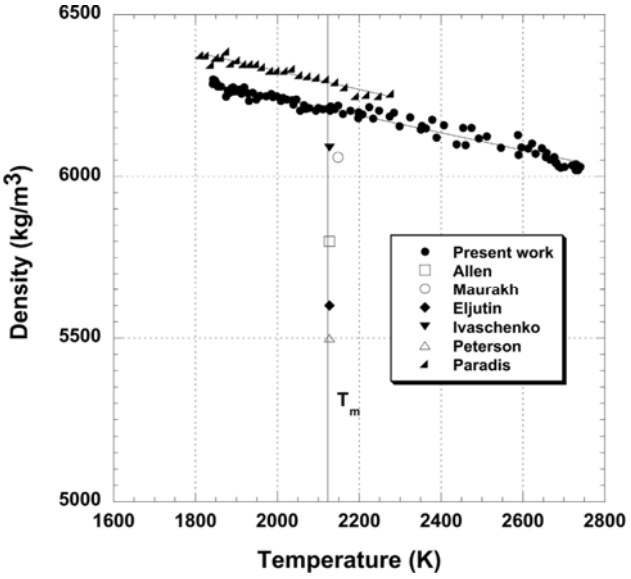

Fig. 4. Density of Zr as a function of temperature, from [26] (the vertical bar corresponds to Zr melting point).

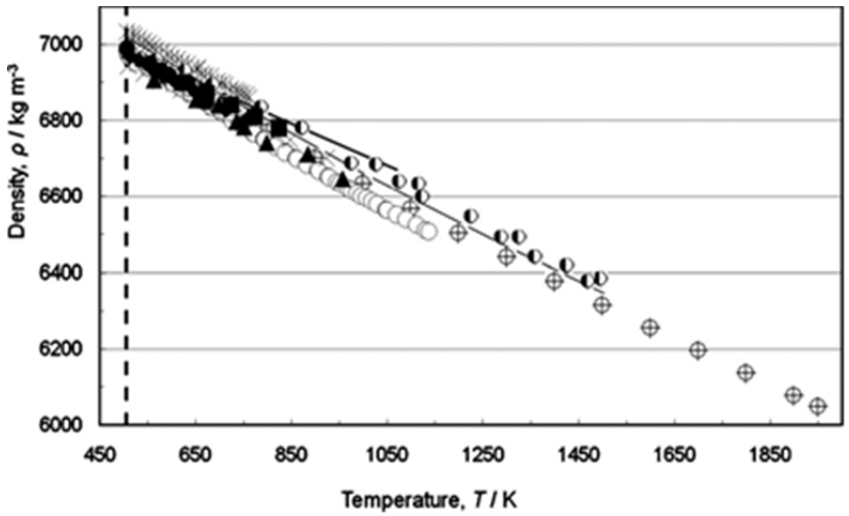

322

323 **Fig. 5.** Density of Sn as a function of temperature, from [27] (the vertical bar corresponds to Sn
324 melting point).

325

326 From these figures, it is not possible to decide with a great confidence whether Sn should
327 be considered as heavier or lighter than Zr at high temperature, around 2128 K, i.e. Zr melting
328 temperature. Clearly, the value of the solutal expansion coefficient cannot be readily given.

329 In order to examine the influence of thermo-solutal convection, four simulations have
330 been run, as shown in Table 4. In Case A, both buoyancy terms were null, which means that the
331 flow is only driven by the forced convection generated by the electromagnetic field. In case B,
332 thermal expansion coefficient for pure Zr has been used, while no solutal buoyancy was applied.
333 Cases C and D take into account solutal buoyancy, with a negative (case C) and positive (case D)
334 value of the Sn expansion coefficient. The negative coefficient $\beta_S^{Sn} = -1 \cdot 10^{-2}(wt\%)^{-1}$,
335 defined in case C, was chosen to investigate on the consequences of cooperating buoyancy
336 forces. On the contrary, the positive value in case D implies opposing buoyancy forces.

337

338 **Table 4.** Definition of the four simulations run to study the effect of thermo-solute convection

case	$\beta_T\ [°C^{-1}\ ]$	$\beta_S^{Sn}[wt\%^{-1}]$
A	0	0
B	$4 \cdot 10^{-5}$	0
C	$4 \cdot 10^{-5}$	$-1 \cdot 10^{-2}$
D	$4 \cdot 10^{-5}$	$3 \cdot 10^{-2}$

339

340 **4.1.2 Characteristics of the liquid metal pool**

341 The metal flow in the melt pool and mushy zone has been investigated at instants
342 corresponding to alternated or continuous stirring periods applied during the melt. In the latter
343 case, the hydrodynamics in the (r, z) plane is quite stationary, whereas in the former one, two
344 different moments have been considered during the stirring sequence:

345 - time t_1 is characterized by a low azimuthal velocity of the liquid, hence a low centrifugal force

346 - time t_2 is characterized by a high azimuthal velocity of the liquid, hence a high centrifugal force.

347 Flows during the continuous stirring stage (time t_3) and at time t_2 are similar, since the
348 azimuthal velocity in both cases is high (see Fig. 6). However, as can be seen in Fig. 6,
349 the transition from alternated to continuous stirring changes the depth and shape of the
350 liquid pool as well as the size of the mushy zone. In the case of alternated stirring, the
351 liquid pool is shallower and more parabolic in shape, whereas in the case of continuous
352 stirring, the pool is deeper and cone-shaped, with a larger mushy zone.

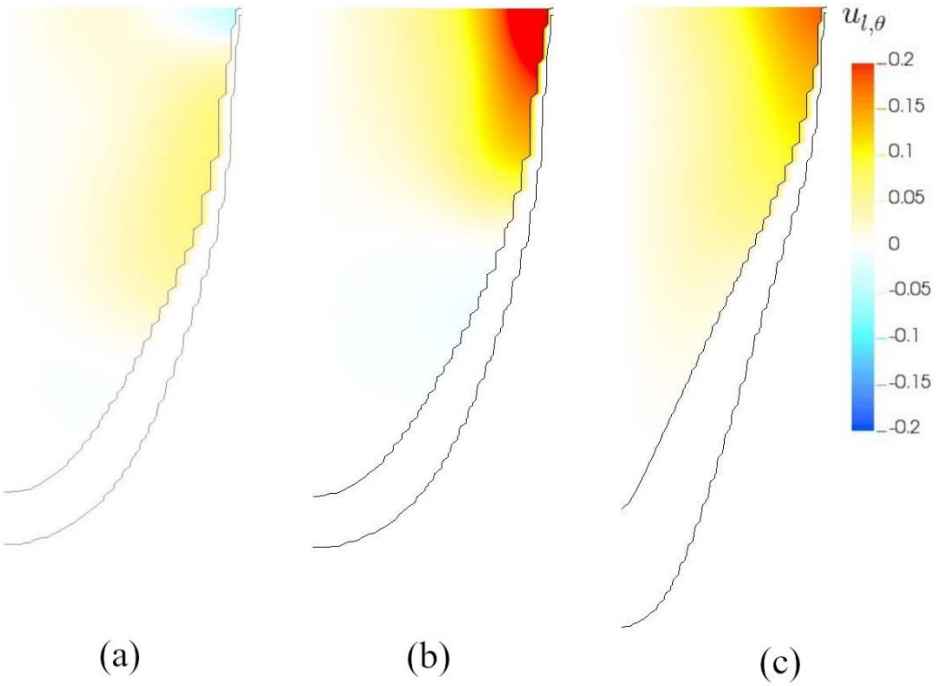

353 **Fig. 6.** Case A – Computed pool profile and azimuthal velocity ($m.s^{-1}$) map in the melt pool at 3
354 different moments during the melt. (a) Time t_1 - alternated stirring, low azimuthal velocity. (b)
355 Time t_2 - alternated stirring, high azimuthal velocity. (c) Time t_3 - continuous stirring, high
356 azimuthal velocity.

357

358 The hydrodynamic behavior at time t_1 (low azimuthal velocity) is the object of Fig. 7. The
359 turbulence intensity is represented by the μ_t/μ viscosity ratio and the velocity field by velocity
360 vectors in the upper part of the melt pool where velocities are high and by streamlines in the
361 lower part of the melt pool and in the mushy zone, where velocities are significantly lower.
362 Without any buoyancy phenomena, the electromagnetic force causes two recirculation
363 loops (Fig. 7 (a)). The interaction between the melting current and the self-induced magnetic field
364 generates centripetal forces localized in the near-surface region, at the origin of a counter-

365 clockwise recirculation flow of the liquid metal in the upper part of the pool. In the mid-height
366 zone of the pool, stirring centrifugal forces prevail, reinforcing the upper recirculation flow and
367 creating a second clockwise loop in the lower part of the pool.

368 When thermal buoyancy is added (case B), it can be seen in fig. 7(b) that the two
369 recirculation loops remain qualitatively identical. The major modification is a strong decrease in
370 the turbulence intensity in the near-surface region, as the high vertical thermal stratification
371 strongly dissipates turbulence (eq. 15).

372 Turbulence characteristics of the flow is almost identical to case B when solute buoyancy
373 is added (cases C and D).

374 The collaborating solute buoyancy has a negligible impact on the “two recirculation
375 loops” system observed for cases A and B. However, in case D, the opposing solute buoyancy
376 leads to the apparition of a third counter-clockwise recirculation flow in the bottom of the pool
377 and in the mushy zone. As Sn partition ratio is lower than unity, solute redistribution during
378 solidification causes a liquid enrichment in solute in the mushy zone. This enrichment causes a
379 decrease in liquid density due to the positive solutal expansion coefficient. Finally, the resulting
380 solutal buoyancy force, localized in the mushy zone, promotes an upward flow along the
381 solidification front, inducing the observed third bottom loop.
382

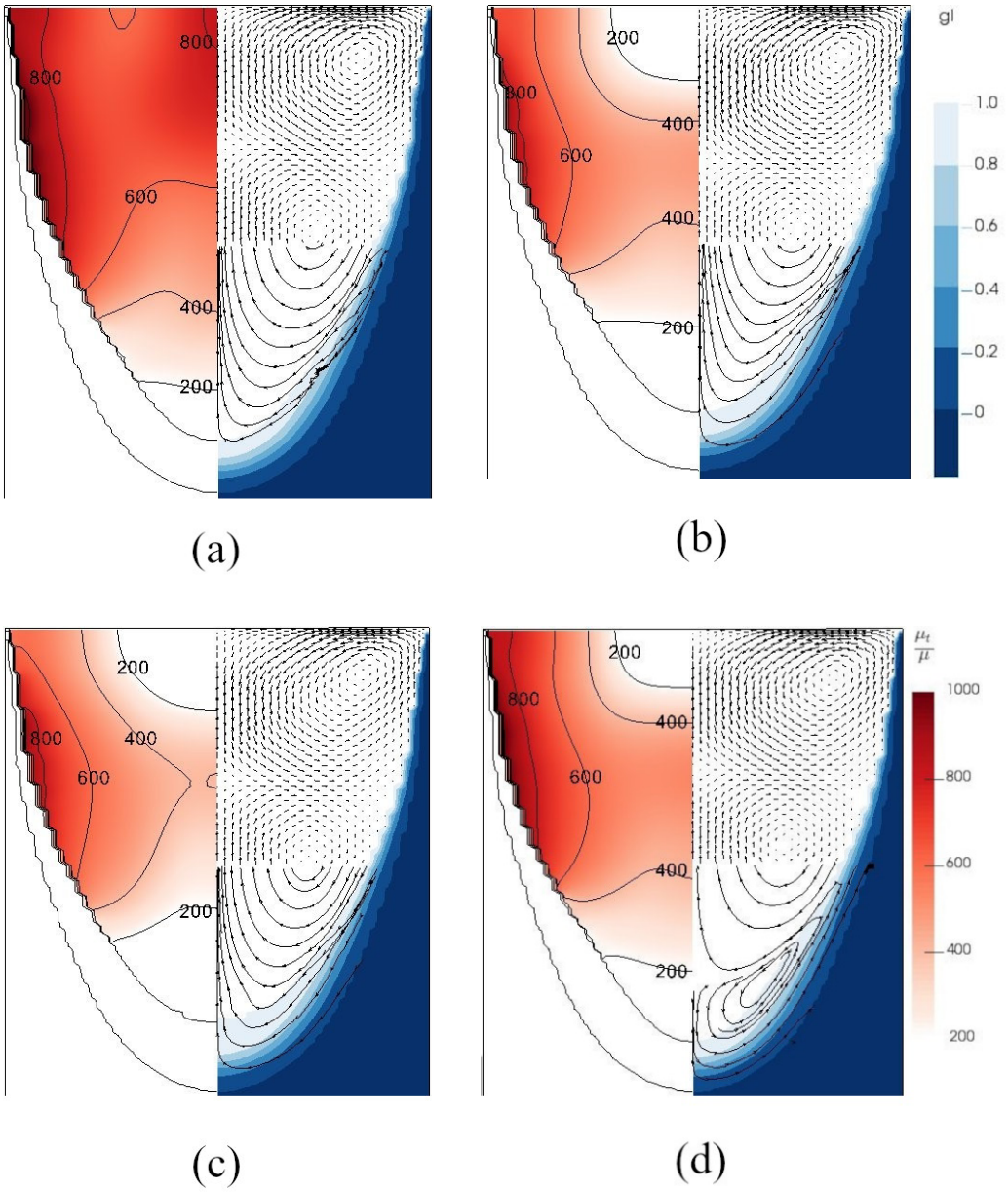

383 **Fig. 7**. Computed flow in the melt pool and mushy zone at time t_l (alternated stirring, low
384 azimuthal velocity). Left side is the turbulence intensity and right side is the mean flow
385 represented by vectors (pool upper part) or streamlines (pool lower part and mushy zone) and the
386 liquid fraction map. (a) Case A: $\beta_T = 0$, $\beta_S^{Sn} = 0$, $v_{max} = 2.03$ cm.s^{-1}. (b) Case B: $\beta_T = 4 \cdot$
387 10^{-5} °C^{-1}, $\beta_S^{Sn} = 0$, $v_{max} = 1.60$ cm.s^{-1}. (c) Case C: $\beta_T = 4 \cdot 10^{-5}$ °C^{-1}, $\beta_S^{Sn} = -1 \cdot$

10^{-2} $wt\%^{-1}$, $v_{max} = 1.82$ cm.s^{-1}. (d) Case D: $\beta_T = 4 \cdot 10^{-5}\ °C^{-1}$, $\beta_S^{Sn} = 3 \cdot 10^{-2}$ $wt\%^{-1}$, $v_{max} = 1.61$ cm.s^{-1}.

The influence of a high azimuthal velocity on the in-plane velocity field and turbulence intensity in the melt pool and mushy zone is shown in Figs. 8 and 9, for instants t_2 during the alternated stirring and t_3 during the continuous stirring.

Compared to the previous case, azimuthal velocity generated by the stirring is 60 % higher, implying an increase in centrifugal forces of 156 %. Therefore, the self-induced forces become of second order and, thus, the circulation counter-clockwise loop in the near surface region disappears.

Similar to previous simulations, the introduction of thermal buoyancy forces considerably reduces the intensity of turbulence in the near-surface area (cases B, C and D).

A collaborative solutal buoyancy slightly decreases turbulence intensity in the bottom of the pool in case C in the frame of a strong alternated stirring (Fig. 8(c)). This is due to the local vertical solute stratification, in the same way as the effects of thermal buoyancy near the free surface.

Finally, an opposite solutal buoyancy generates an additional recirculation loop in the bottom of the pool for all stirring conditions (Fig. 8(d) and Fig. 9(d)).

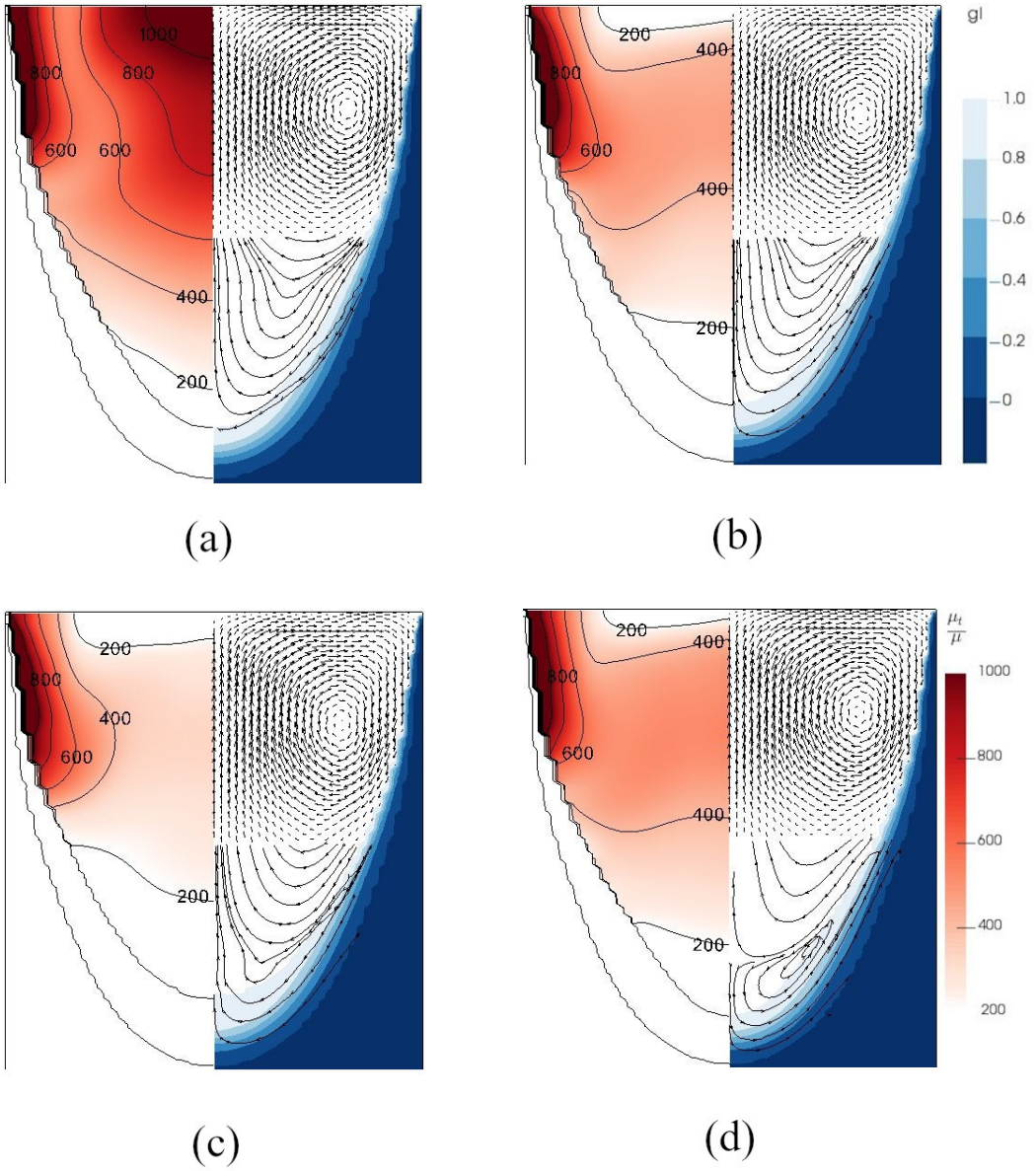

409 **Fig. 8**. Computed flow in the melt pool and mushy zone at time t_2 (alternated stirring, high
410 azimuthal velocity). Left side is the turbulence intensity and right side is the mean flow
411 represented by vectors (pool upper part) or streamlines (pool lower part and mushy zone) and the
412 liquid fraction map. (a) Case A: $\beta_T = 0$, $\beta_S^{Sn} = 0$, $v_{max} = 2.53$ cm.s^{-1}. (b) Case B: $\beta_T = 4 \cdot$
413 10^{-5} °C^{-1}, $\beta_S^{Sn} = 0$, $v_{max} = 2.53$ cm.s^{-1}. (c) Case C: $\beta_T = 4 \cdot 10^{-5}$ °C^{-1}, $\beta_S^{Sn} = -1 \cdot$

414 10^{-2} wt%$^{-1}$, $v_{max} = 2.50$ cm.s^{-1}. (d) Case D: $\beta_T = 4 \cdot 10^{-5}$ °C^{-1}, $\beta_S^{Sn} = 3 \cdot 10^{-2}$ wt%$^{-1}$,

415 $v_{max} = 2.51$ cm.s^{-1}.

416

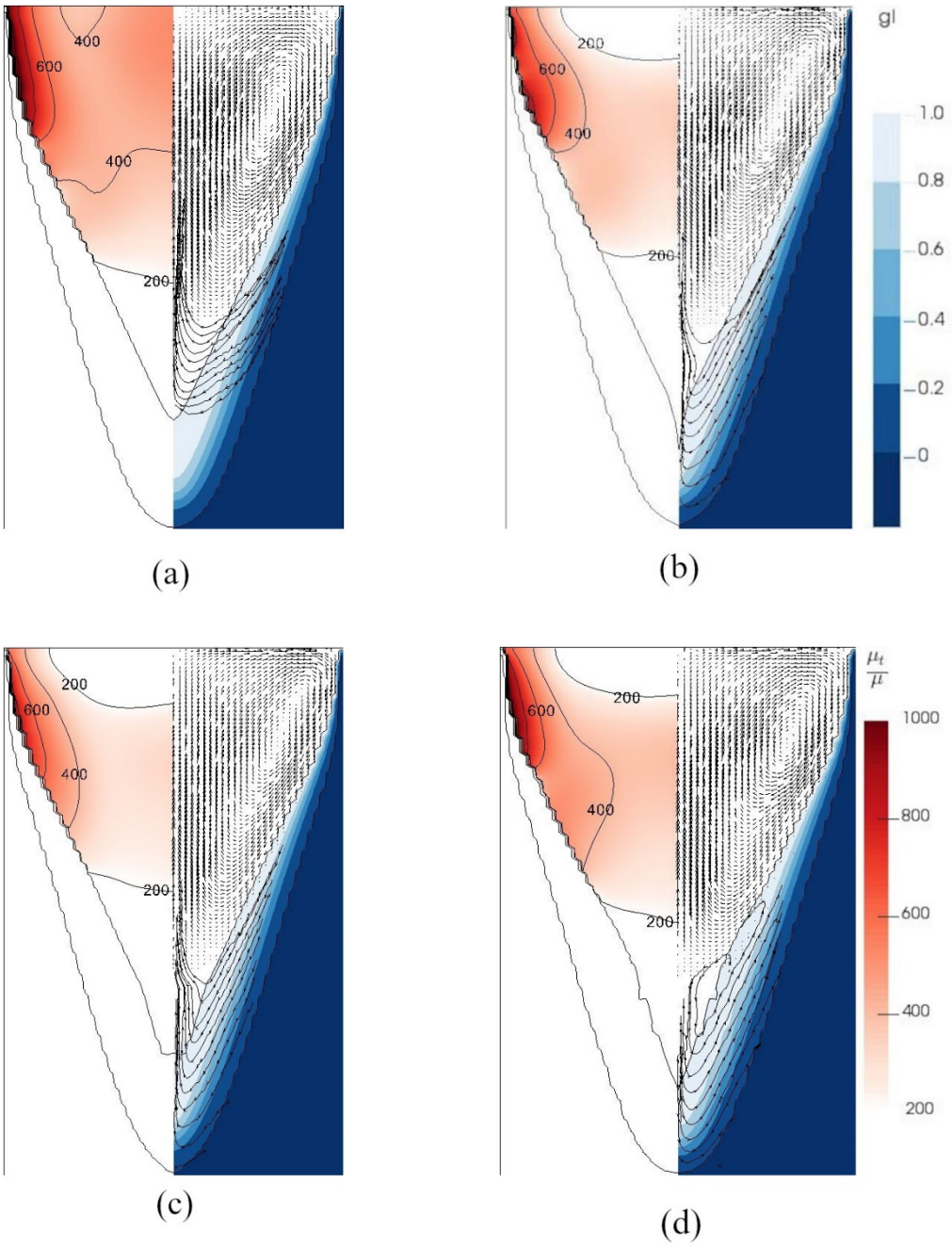

417 **Fig. 9**. Computed flow in the melt pool and mushy zone at time t_3 (continuous stirring, high

418 azimuthal velocity). Left side is the turbulence intensity and right side is the mean flow

represented by vectors (pool upper part) or streamlines (pool lower part and mushy zone) and the liquid fraction map. (a) Case A: $\beta_T = 0$, $\beta_S^{Sn} = 0$, $v_{max} = 2.02$ cm.s^{-1}. (b) Case B: $\beta_T = 4 \cdot 10^{-5}\ °C^{-1}$, $\beta_S^{Sn} = 0$, $v_{max} = 1.93$ cm.s^{-1}. (c) Case C: $\beta_T = 4 \cdot 10^{-5}\ °C^{-1}$, $\beta_S^{Sn} = -1 \cdot 10^{-2}\ wt\%^{-1}$, $v_{max} = 1.83$ cm.s^{-1}. (d) Case D: $\beta_T = 4 \cdot 10^{-5}\ °C^{-1}$, $\beta_S^{Sn} = 3 \cdot 10^{-2}\ wt\%^{-1}$, $v_{max} = 2.00$ cm.s^{-1}.

4.2. Macrosegregation

Macrosegregation behaviour of the remelted product is now numerically investigated. Particular attention is paid to the influence of the thermophysical properties defined in the macromodel, such as thermal and solutal buoyancy forces, as well as the solidification properties implemented in the micromodel, such as dendrite arm spacing and grain growth kinetics.

As computed results differed only slightly from previous calculations[28], where a simplified solidification model assumed complete diffusion of all solutes in both liquid and solid phases (i.e. lever rule), it appears that the use of a detailed solidification micromodel confirmed the trends which had been highlighted with a simplified lever-rule based model.

4.2.1. Influence of the thermo-solutal convection

The computed maps of Sn content in the final ingot are shown in Fig. 10. As discussed previously, the two declined Sn-depleted bands are a consequence of the strong electromagnetic stirring (see Fig. 3 (b)) that was applied to mark the melt pool profile in the ingot macrostructure. The average concentration of Sn in the liquid pool increases as the ingot grows because the

partition coefficient k_p^{Sn} is lower than 1. Solidification of the last liquid pool causes a local enrichment at the top of the ingot. A strong negative segregation is predicted at the lateral surface and at the bottom of the ingot. However, results at the periphery must be handled with care because the segregation calculated there is very sensitive to mesh size.

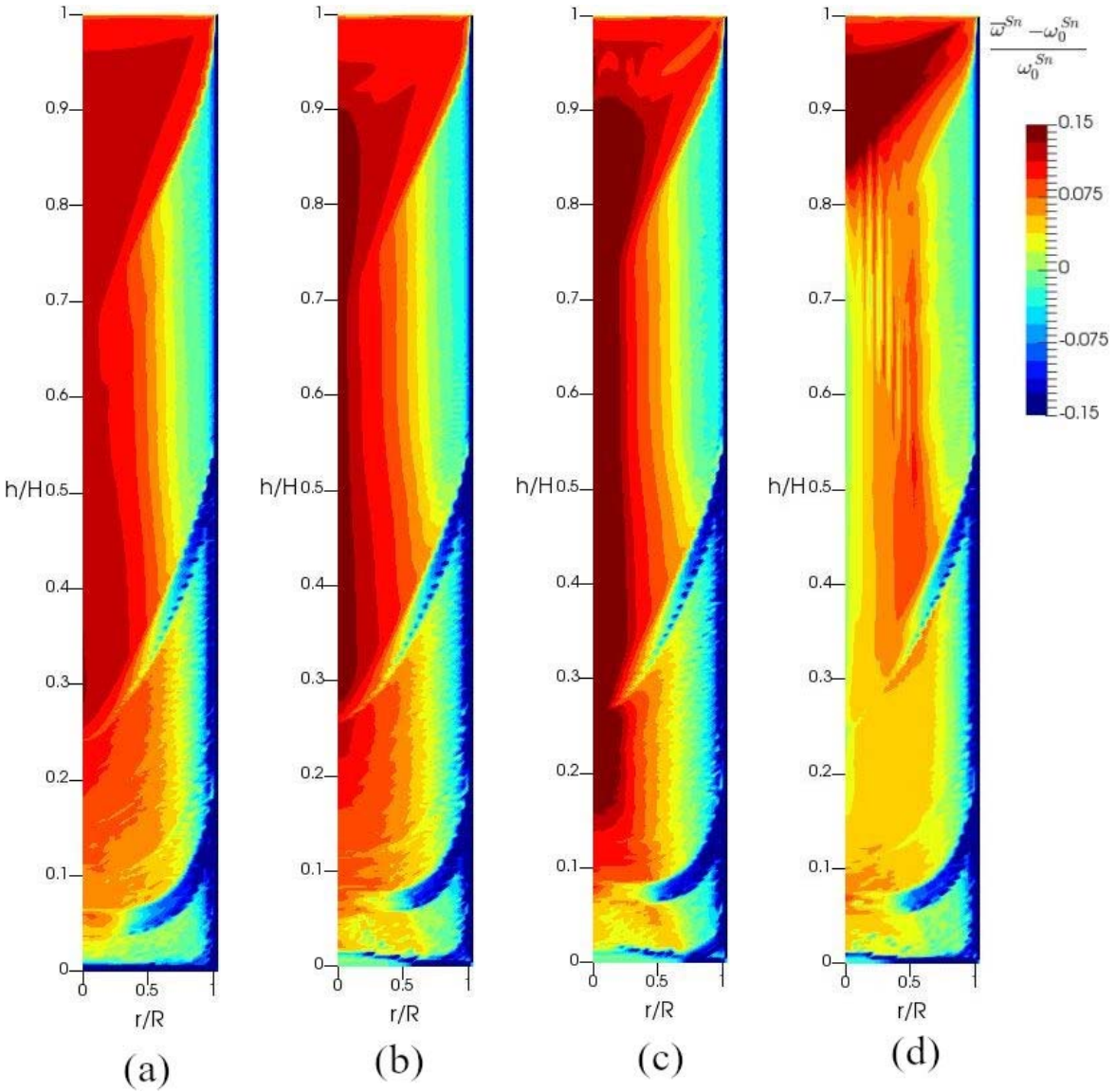

Fig. 10. Computed Sn content map in the remelted ingot. (a) Case A: $\beta_T = 0$, $\beta_S^{Sn} = 0$. (b) Case B: $\beta_T = 4 \cdot 10^{-5}\ °C^{-1}$, $\beta_S^{Sn} = 0$. (c) Case C: $\beta_T = 4 \cdot 10^{-5}\ °C^{-1}$, $\beta_S^{Sn} = -1 \cdot\ 10^{-2}\ wt\%^{-1}$. (d) Case D: $\beta_T = 4 \cdot 10^{-5}\ °C^{-1}$, $\beta_S^{Sn} = 3 \cdot 10^{-2}\ wt\%^{-1}$.

In the absence of buoyancy (case A), the model predicts a Sn enrichment in the ingot centre for the two stirring regimes used during the melt. This is the result of the clockwise flow measurement cell discussed in the previous section. The liquid flows down along the solidification front. As a result, the liquid enriched in Sn piles up in the mushy zone and at the bottom of the melt pool, resulting in a positive segregation on the axis of symmetry. As shown in Fig. 10, radial macrosegregation is weaker with alternating stirring than with continuous stirring.

The addition of thermal convection (case B) slightly increases the radial macrosegregation for both stirring sequences. The centrifugal force is reinforced by thermal buoyancy, which causes more intense circulation in the mushy zone and greater transport of enriched liquid to the central axis.

The convection effects induced by the solutal buoyancy are presented in Figs. 10 (c) and 10 (d). They prevail in the central part of the mushy zone and have an impact on segregation. In case C, the segregation at the central axis is notably amplified by the cooperation of solutal and thermal buoyancy. The opposite effect is observed in case D, where the effects of solutal and thermal buoyancy are opposed: the segregation at the central axis is considerably reduced, due to the upward flow in the mushy region. A positive segregation band is therefore located at $r/R \sim 0.5$.

Moreover, in case D, during the continuous stirring sequence, a series of vertical channels appear in the enriched segregation part. Fig. 11 details this effect. The Sn-enriched liquid

accumulated near the centerline is transported outward under the influence of solutal convection. This transport of solute is effective for a liquid fraction $g_l > 0.6$. When $g_l < 0.6$, the permeability of the porous media decreases rapidly as the drag forces dominate inertial and buoyancy forces and macrosegregation evolution is stopped.

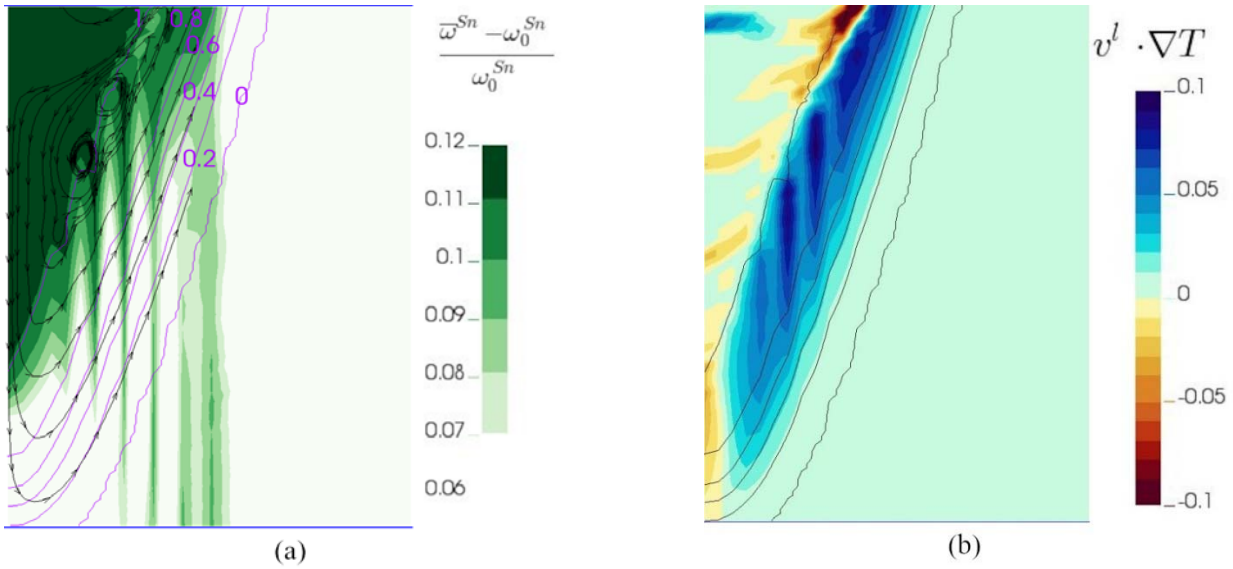

Fig. 11. Zoom visualization of the influence of solute-driven convection at time t_3 - continuous stirring, high azimuthal velocity. Case D - $\beta_T = 4 \cdot 10^{-5}\ °C^{-1}$, $\beta_S^{Sn} = 3 \cdot 10^{-2}\ wt\%^{-1}$. (a) Liquid fraction, streamlines and Sn content. (b) Liquid fraction and convective $v^l.\nabla T$ term.

In Fig. 12, the predicted radial Sn segregation profiles are plotted at two different heights and compared to experimental measurements. Those heights are representative for the alternated stirring ($h/H = 0.25$) and continuous stirring ($h/H = 0.75$) stages. Comparison of the simulation results with the experimental measurements confirms the importance of solutal convection in the mushy zone. At $h/H = 0.75$, the measured Sn concentration continuously increases in the inner part of the ingot until it reaches its maximum at $r/R = 0.5$. The simulated results show the same tendency only in case D, where solutal convection is opposed to thermal

481 one. Among the calculations, case D, where the solute coefficient $\beta_S^{Sn} = 3 \cdot 10^{-2}(wt\%)^{-1}$, has
482 the best fit to the measured data and was therefore chosen for subsequent simulations.

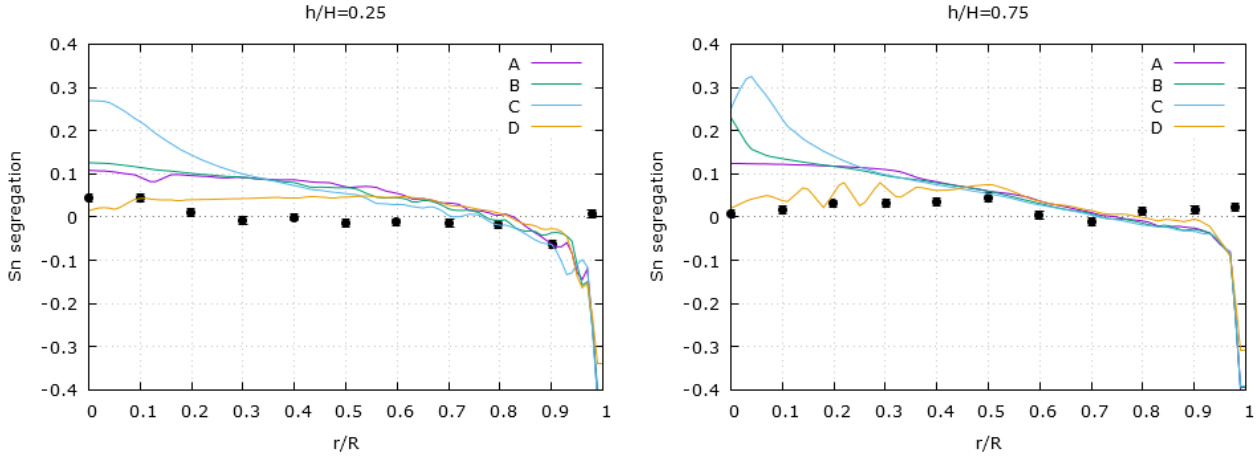

483 **Fig. 12**. Radial profiles of Sn segregation $(\overline{\omega}^{Sn} - \omega_0^{Sn})/\omega_0^{Sn}$ at 2 heights in the remelted ingot.
484 Experimental (•) and model (-) results. Letters A, B, C, D correspond to cases listed in Table 4.

485

486 The computed profiles of the radially averaged longitudinal Sn content are shown in
487 Fig. 13. Thermo-solutal convection has no significant effect on the overall longitudinal
488 segregation. Although the comparison of simulated results with experimental measurements
489 should be interpreted with caution, due to the limited number of measurements along the ingot
490 height, the results show a fairly good agreement.

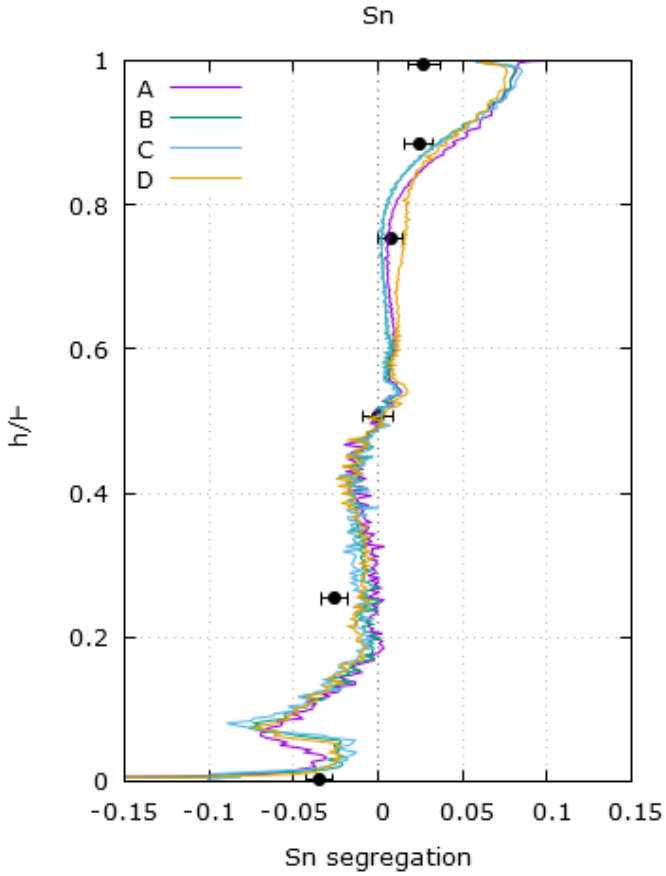

491 **Fig. 13.** Radially-averaged longitudinal profiles of Sn segregation $(\overline{\omega}^{Sn} - \omega_0^{Sn})/\omega_0^{Sn}$ in the
492 remelted ingot. Experimental (•) and model (-) results. Letters A, B, C, D correspond to cases
493 listed in Table 4.

494 For a given thermo-solutal convection (case D), Fig. 14 shows the longitudinal content
495 profiles for Sn and other alloying elements, namely Fe, O and Cr. The results for all elements are
496 quite similar (it must be stated that the oxygen partition coefficient k_O is larger than 1) and in
497 fairly good agreement with measurements, except in the bottom part of the ingot. At this location,
498 in addition to a possible effect of dendrite arm spacing (see section 4.2), it could be argued that
499 the discrepancy between the measured chemistry and the predicted segregation is related to the
500 motion of equiaxed grains. [7] showed that the sedimentation of free floating equiaxed grains can

501 significantly affect macrosegregation. Decantation of these grains in the bottom of the melt pool
502 during its solidification could balance the macrosegregation induced by thermo-solutal
503 convection, resulting in a flat segregation profile.

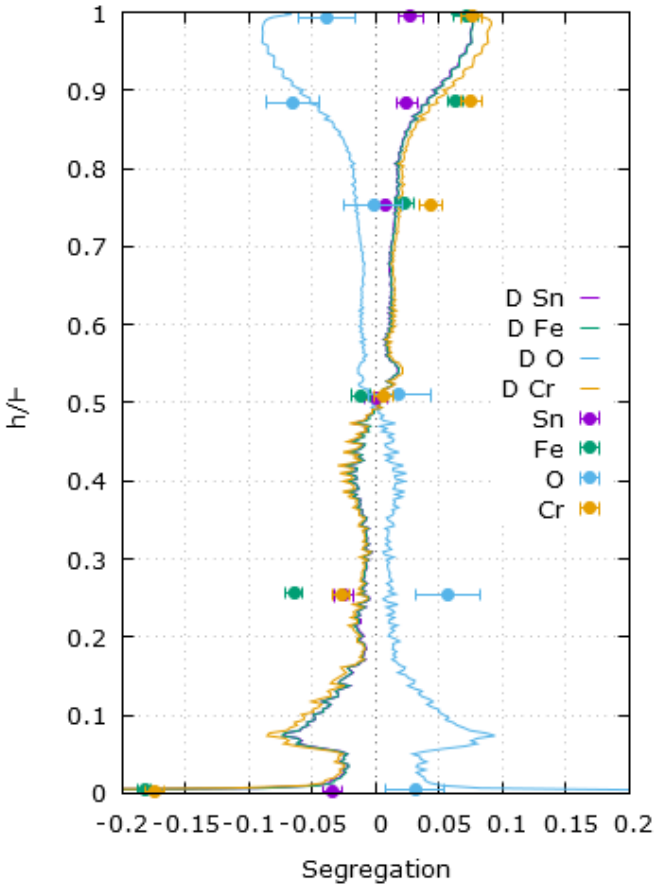

504 **Fig. 14**. Radially-averaged longitudinal profiles of chemical segregation $(\overline{\omega}^{n} - \omega_0^{n})/\omega_0^{n}$ in the
505 remelted ingot for elements Sn, Fe, O and Cr. Experimental (•) and model (-) results. Case D -
506 $\beta_T = 4 \cdot 10^{-5}\ °C^{-1}$, $\beta_S^{Sn} = 3 \cdot 10^{-2}\ wt\%^{-1}$.

507

508 **4.2.2. Influence of the dendrite arm spacing**

509 As discussed in section 3, the solidifying mushy zone is modelled as a porous medium
510 and is characterized by its local permeability which depends on the liquid volume fraction g_l and

511 the dendrite arm spacing λ_{DAS} (Eqs.13 and 17 in Table 1). Unfortunately, it is very difficult to
512 obtain a true value of λ_{DAS} from a conventional metallographic analysis due to the solid state
513 transformation $\beta(\mathrm{cc}) \rightarrow \alpha(\mathrm{hcp})$ that occurs during the cooling of Zirconium alloys. In order to
514 assess the role of the permeability in macrosegregation prediction, three cases were tested for
515 each of the solidification models and are presented in Table 5. The value
516 $\beta_S^{Sn} = 3 \cdot 10^{-2}(wt\%)^{-1}$ (corresponding to case D, see above) was adopted for all calculations.
517

518 **Table 5.** Definition of the three simulations run to study the effect of dendrite arm spacing.

case	λ_{DAS} [μm]	$K_0[\mathrm{m}^2]$
D'	67	$2.5 \cdot 10^{-11}$
D	134	10^{-10}
D''	268	$4 \cdot 10^{-10}$

519

520 The computed Sn macrosegregation maps are shown in Fig. 15. It can be observed that
521 the intensity of macrosegregation increases with λ_{DAS}. To explain this phenomenon, the
522 amplitude of the liquid velocity in the mushy zone during the continuous stirring stage (time t_3) is
523 plotted in Fig. 16 as a function of the liquid fraction. It is obvious that a large λ_{DAS} increases the
524 velocity of the interdendritic liquid flow, thus promoting macrosegregation.

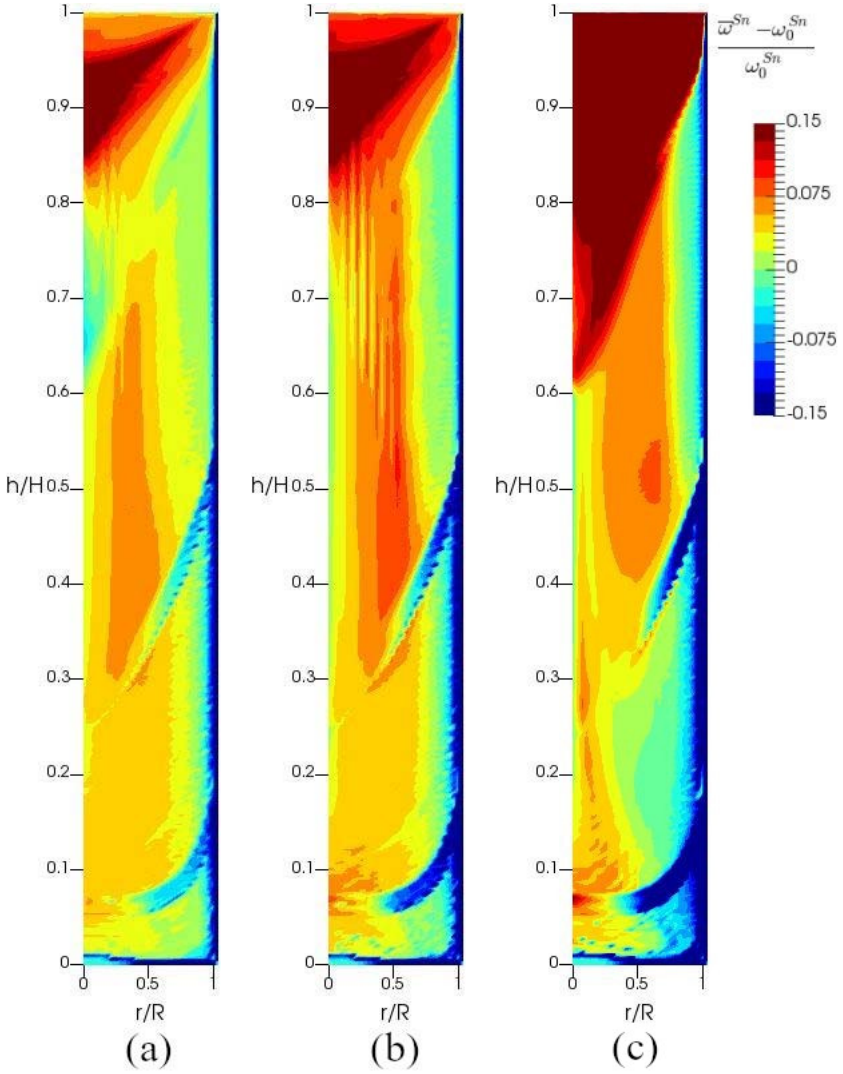

a) b) c)

525 **Fig. 15**. Influence of the dendrite arm spacing λ_{DAS} on the computed Sn macrosegregation map in
526 the remelted ingot. (a) Case D': $\lambda_{DAS} = 67$ µm. (b) Case D: $\lambda_{DAS} = 134$ µm. (c) Case D'':
527 $\lambda_{DAS} = 268$ µm.

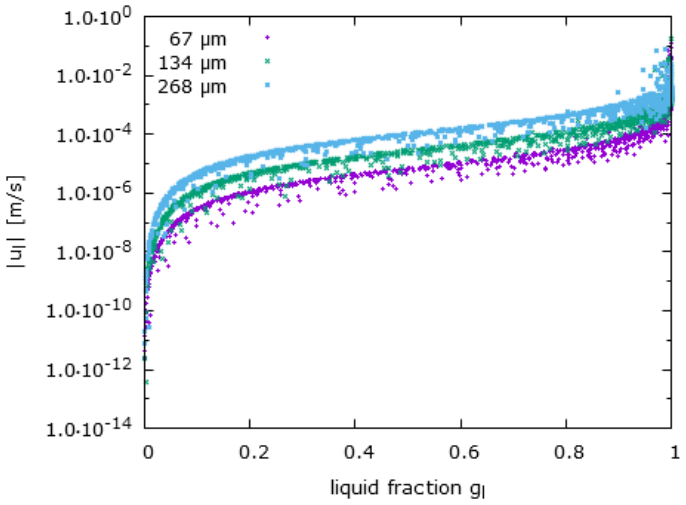

528

529 **Fig. 16**. Magnitude of the liquid velocity in the mushy zone as a function of liquid fraction at
530 time t3 (continuous stirring stage).

531 In Fig. 17, the simulated macrosegregation of Sn is compared to experimental
532 measurements at two different heights ($h/H = 0.25$) and ($h/H = 0.75$). The profiles calculated
533 for $\lambda_{DAS} = 67$ µm and $\lambda_{DAS} = 134$ µm are similar at $h/H = 0.25$. These profiles are quite flat
534 up to $r/R = 0.6$, after which point the Sn concentration gradually decreases. Although the
535 difference between the simulated results and the experimental measurements is not high, it should
536 be noted that the predicted segregation in the mid-radius zone is positive while the experimental
537 segregation is negative. The agreement is much better when λ_{DAS} is increased to 268 µm, because
538 the predictions for this case anticipate the negative Sn segregation values from $r/R = 0.5$ on. At
539 $h/H = 0.75$, on the contrary, a better agreement was found when λ_{DAS} was reduced (case D').

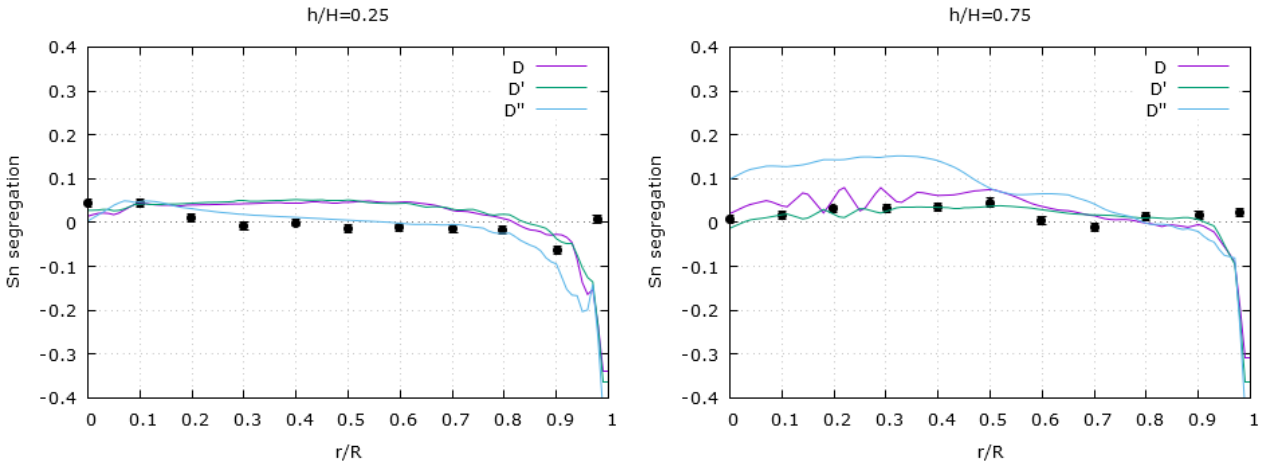

Fig. 17. Radial profiles of Sn segregation $(\overline{\omega}^{Sn} - \omega_0^{Sn})/\omega_0^{Sn}$ at 2 heights in the remelted ingot. Experimental (•) and model results. Letters D, D' and D'' correspond to cases listed in Table 5.

4.2.3. Influence of the grain growth kinetics

The effect of grain growth kinetics on macrosegregation was investigated numerically by examining four different cases listed in Table 6. The default values presented in Table 3 were used for the diffusion coefficients of alloy elements, thermal and solutal expansion coefficients, nucleat+ion density, and secondary dendrite arm spacing, unless otherwise specified. Case D, as usual, represents the case with default values. In case E, the nucleation density N_0 was increased to 10^{12} m^{-3}. In cases F and G, the diffusion coefficient of Sn in the solid phase was reduced to $4.9 \cdot 10^{-15}$ m^2/s for a nucleation density equal to 10^{12} m^{-3} and 10^{10} m^{-3}, respectively.

Table 6. Definition of the four simulations run to study the effect of grain growth kinetics

case	N_0 [m^{-3}]	D_S^{Sn}[m^2/s]

D	10^{10}	$4.9 \cdot 10^{-11}$
E	10^{12}	$4.9 \cdot 10^{-11}$
F	10^{12}	$4.9 \cdot 10^{-15}$
G	10^{10}	$4.9 \cdot 10^{-15}$

553

554 Fig. 18 shows the final macrosegregation maps of Sn computed in all four cases.
555 Although the solidification process differs quantitatively, the comparison of the maps reveals
556 only small differences in the calculated macrosegregation. As apparent from Fig. 18, nucleation
557 density and solute diffusivity did not seem to play an important role in the chemistry of the
558 remelted ingot. Nevertheless, it can be noted that the macrosegregation was slightly less intense
559 in case E.

560 The small differences observed between these different cases can be explained by
561 studying the value of the Fourier number in order to characterize the diffusion of solute in the
562 solid and liquid phases in the central part of the ingot. The Fourier number associated to a given
563 phase (solid or liquid) is defined as the ratio $o = \frac{D \cdot t_{ls}}{R_g^2}$. In this relationship, D is the solute
564 diffusion coefficient in the considered phase, t_s is the local solidification time, and R_g is the final
565 average grain radius as defined in equation (22) in Table 2. As it can be seen in this equation, the
566 final grain radius is only dependent of the grain density which is an input of the model. If the
567 value of the Fourier number is greater than 1 the composition profile of the alloying element can
568 be considered as uniform in the phase, while if it is smaller than 1 the composition profile is non
569 uniform. The values of the Fourier numbers for the liquid and solid phases are reported in Table 7
570 considering two local solidification times (t_{ls}), respectively 10 and 1260 s. The first value
571 corresponds to the solidification time at a point close to the skin while the second one stands for a

location in the central part of the ingot. These points have been chosen along a line at mid-height of the ingot. They are considered to be representative of extreme values of the Fourier numbers in the solid and liquid phases.

Table 7. Values of the Fourier number in the liquid and solid phases for the four cases (D, E, F, G). These Fourier numbers are estimated for two local solidification times (10 s and 1260 s). These values correspond to points located close to the skin of the ingot and for the second one to a point located at the center of the ingot. Both of them are considered at mid-height of the ingot.

	t_{ls} = 10 s		t_{ls} = 1260 s)	
	Fo_l^{Sn}	Fo_S^{Sn}	Fo_l^{Sn}	Fo_S^{Sn}
D	1.2	0.006	150	0.75
E	2.6	0.127	3270	16
F	2.6	10^{-5}	3270	0.0016
G	1.2	$6\ 10^{-7}$	150	$7.5\ 10^{-5}$

For the two points and all 4 cases, the Fourier number values in the liquid phase are greater than 1, thus the solute profile at the microscopic scale was uniform in the liquid phase during almost all the solidification. Considering the point close to the skin, the Fourier number in the solid phase is lower than 1 in all cases. This means that there is no diffusion of solute in the solid phase at the microscopic scale in all cases for the point close to the skin. The skin is thus a region for which all cases correspond to the same situation at the microscopic scale: perfect diffusion of solute in the liquid and no diffusion of solute in the solid. This is why the macrosegregation is very similar for all the cases in the region of the skin of the ingot.

589 Considering the point located at mid-height in the center of the ingot, for cases D, F and G, the
590 Fourier number value in the solid phase is lower than 1 while it is greater than 1 for case E. These
591 results show that for cases D, F and G, solidification proceeds in such a way that the solute
592 diffuses perfectly in the liquid phase and very little in the solid phase. For case E, the diffusion of
593 the solute is perfect in the solid and liquid phases. For all cases, the diffusion is perfect in the
594 liquid phase, only the diffusion of the solute in the solid phase is different. It has already been
595 shown that solute diffusion in the solid phase has very little influence on macrosegregation[29].
596 This can explain why cases D, E, F, G lead to similar macrosegregation.

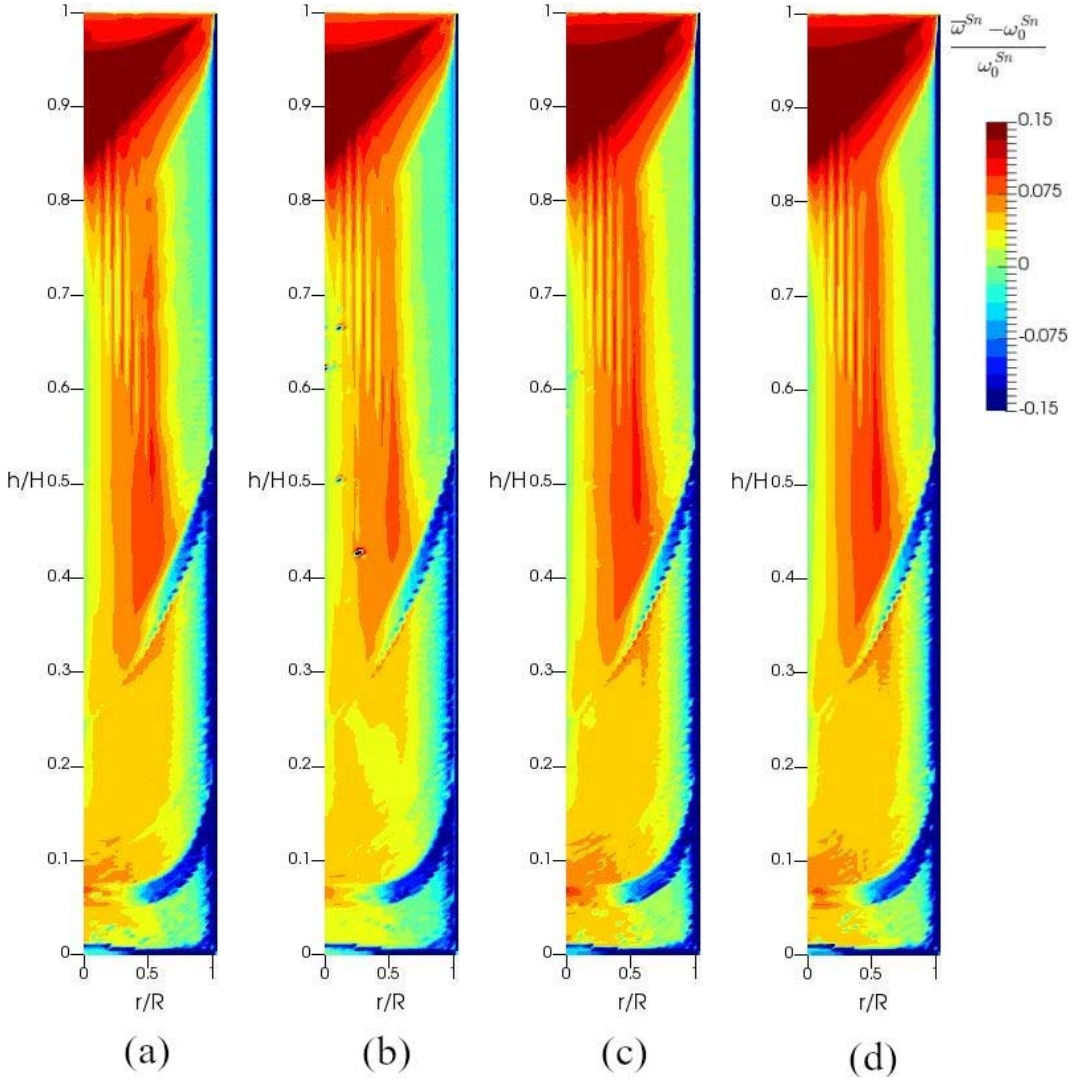

597 **Fig. 18**. Computed Sn content map in the remelted ingot, (a) case D, (b) case E, (c) case F and (d)
598 case G. Letters D, E, F, G correspond to cases listed in Table 6.

599

600 **5 Conclusions and prospects**

601 A two-scale model was used to simulate the solidification of the remelting of an
602 experimental chemically homogeneous Zy-4 electrode in a production furnace. The effects of
603 thermal and solutal convection on ingot macrosegregation, as well as the influence of dendrite
604 arm spacing (i.e. the permeability of the mushy region) were studied and analyzed. In addition,
605 the influence of grain growth kinetics was investigated numerically.

606 The results show that it is necessary to take into account the thermal and solutal buoyancy
607 forces in order to obtain an accurate simulation of hydrodynamics and consequently the
608 macrosegregation in VAR ingots. Comparing the experimental measurements with the simulated
609 results, it is concluded that solutal-driven convection may promote an upward flow along the
610 solidification front in the mushy zone and thus be partially responsible for macrosegregation in
611 the central part of the ingot. Furthermore, the simulations have shown that the macrosegregation
612 predicted by the model depends on the dendrite arm spacing value used to calculate local
613 permeability in the mushy zone. However, the model is still unable to predict some of the trends
614 observed in experimental measurements.

615 In future work, the transport of free-floating grains and the flow induced by the
616 solidification shrinkage will be implemented in the SOLAR code. Such additions could
617 significantly affect the predicted hydrodynamic behaviour, resulting in macrosegregation.

618

Acknowledgments

As a part of the OPERAS (Optimizing Processes based on Electrode Remelting with Arc or Slag) Project, this work has been partly supported by the French National Research Agency (ANR-08-MAPR-0006-04).

Conflict of interest

On behalf of all authors, the corresponding author states that there is no conflict of interest.

References

1 A. Jardy and D. Ablitzer: *Xiyou Jinshu Cailiao Yu GongchengRare Met. Mater. Eng.*, 2006, vol. 35, pp. 119–122.
2 A. Jardy and D. Ablitzer: *Mater. Sci. Technol.*, 2009, vol. 25, pp. 163–9.
3 A. Wilson and A. Jardy: in *A numerical study of the influence of stirring parameters on titanium ingot quality using SOLAR v4.2*, vol. 1, The Japan Institute of Metals, Kyoto, Japan, 2007.
4 V. Venkatesh, A. Wilson, M. Kamal, M. Thomas, and D. Lambert: *JOM*, 2009, vol. 61, pp. 45–50.
5 P. Chapelle, A. Jardy, J.P. Bellot, and M. Minvielle: *J. Mater. Sci.*, 2008, vol. 43, pp. 5734–46.
6 M. Revil-Baudard, A. Jardy, F. Leclerc, M. Zaloznik, V. Rebeyrolle, and H. Combeau: in *CFD Modeling and Simulation in Materials Processing*, John Wiley & Sons, Ltd, 2012, pp. 107–14.
7 H. Combeau, M. Založnik, S. Hans, and P.E. Richy: *Metall. Mater. Trans. B*, 2009, vol. 40, pp. 289–304.
8 B.E. Launder and D.B. Spalding: *Comput. Methods Appl. Mech. Eng.*, 1974, vol. 3, pp. 269–89.
9 P.J. Prescott and F.P. Incropera: *J. Heat Transf.*, 1995, vol. 117, pp. 716–24.
10 B.V. Antohe and J.L. Lage: *Int. J. Heat Mass Transf.*, 1997, vol. 40, pp. 3013–24.
11 A. Nakayama and F. Kuwahara: *J. Fluids Eng.*, 1999, vol. 121, pp. 427–33.
12 M.H.J. Pedras and M.J.S. de Lemos: *Int. J. Heat Mass Transf.*, 2001, vol. 44, pp. 1081–93.
13 S. Hans: PhD thesis (in French), Institut National Polytechnique de Lorraine, 1995.
14 T. Quatravaux: PhD thesis (in French), Institut National Polytechnique de Lorraine, 2004.
15 M. Revil-Baudard: PhD thesis (in French), Université de Lorraine, 2012.
16 C. Beckermann and R. Viskanta: *Physicochem. Hydrodyn.*, 1988, vol. 10, pp. 195–213.
17 C.Y. Wang and C. Beckermann: *Metall. Mater. Trans. A*, 1996, vol. 27, pp. 2754–64.
18 M. Založnik and H. Combeau: *Comput. Mater. Sci.*, 2010, vol. 48, pp. 1–10.
19 K. Tveito, M. Bedel, M. Založnik, H. Combeau, and M. M'Hamdi: vol. 27, IOP Publishing, 2012, p. 012040.
20 T.B. Massalski, H. Okamoto, P. Subramanian, L. Kacprzak, and W.W. Scott: *Binary Alloy Phase Diagrams*, vol. 1, American society for metals Metals Park, OH, 1986.
21 T. Quatravaux, S. Ryberon, S. Hans, A. Jardy, B. Lusson, P.E. Richy, and D. Ablitzer: *J. Mater. Sci.*, 2004, vol. 39, pp. 7183–91.
22 G. Ghazal, A. Jardy, P. Chapelle, and Y. Millet: *Metall. Mater. Trans. B*, 2010, vol. 41, pp. 646–59.

23 A. Jardy, F. Leclerc, M. Revil-Baudard, P. Guerin, H. Combeau, and V. Rebeyrolle: *J. ASTM Intern.*, DOI:10.1520/JAI102992.
24 M. Založnik and H. Combeau: *Int. J. Therm. Sci.*, 2010, vol. 49, pp. 1500–9.
25 P.-F. Paradis and W.-K. Rhim: *J. Mater. Res.*, 1999, vol. 14, pp. 3713–9.
26 T. Ishikawa and P.-F. Paradis: *J. Electron. Mater.*, 2005, vol. 34, pp. 1526–32.
27 M.J. Assael, A.E. Kalyva, K.D. Antoniadis, R. Michael Banish, I. Egry, J. Wu, E. Kaschnitz, and W.A. Wakeham: *J. Phys. Chem. Ref. Data*, 2010, vol. 39, p. 033105.
28 M. Revil-Baudard, A. Jardy, H. Combeau, F. Leclerc, and V. Rebeyrolle: *Metall. Mater. Trans. B*, 2014, vol. 45, pp. 51–7.
29 M.C. Schneider and C. Beckermann: *Int. J. Heat Mass Transf.*, 1995, vol. 38, pp. 3455–73.

List of figures

List of tables

On the prediction of macrosegregation in Vacuum Arc Remelted ingots

K. Mramor[a] , T. Quatravaux[a*], H. Combeau[a], A. Jardy [a], M. Založnik[a], I. Crassous[b], A. Gaillac[b]

[a] Institut Jean Lamour – UMR 7198 CNRS/Université de Lorraine, Laboratory of Excellence DAMAS, Campus ARTEM, 2 allée André Guinier, BP 50840, F-54011 NANCY, France

[b] Framatome, Components Research Center, Avenue Paul Girod, F-73403 UGINE, FRANCE

*corresponding author: thibault.quatravaux@univ-lorraine.fr, +33 (0)372742900

katarina.mramor@fs.uni-lj.si, herve.combeau@univ-lorraine.fr, alain.jardy@univ-lorraine.fr, miha.zaloznik@univ-lorraine.fr, isabelle.crassous@framatome.com, alexis.gaillac@framatome.com

Abstract

The chemical homogeneity and metallurgical structure of vacuum arc remelted (VAR) zirconium ingots are directly responsible for product quality. It is therefore important to understand the relationship between these properties and the operating conditions. An in-depth analysis of the modelling of solidification phenomena during the VAR was carried out.

Such model, solves a coupled set of transient equations for heat, momentum, solute transport and turbulence in an axisymmetric geometry. The remelting and cooling of a cylindrical ingot are calculated for time-dependent operating parameters.

The solidification mechanisms implemented in the model can be applied to multi-component industrial alloys such as Zircaloy-4, which provides information on the macrosegregation phenomena studied in this paper.

The model results were validated, based on the remelting of a specially designed chemically homogeneous Zircaloy-4 electrode. The results illustrate the importance of thermal

and solute convection, the importance of the permeability of the partially solid material and the weak influence of nuclei density and solute diffusion in the solid phase on the prediction of macrosegregation in Zircaloy-4 ingots.

Keywords: Numerical solution; Solidification; Zirconium alloys; Macrosegregation; Vacuum Arc Remelting, Secondary Metallurgy

Nomenclature

B	magnetic field (T)
D	diffusion coefficient of solute in the liquid or the solid phase ($m^2.s^{-1}$)
F_{el}	electromagnetic force (N)
g	gravitational acceleration ($m.s^{-2}$)
g_l	volume fraction of the liquid phase
g_s	volume fraction of the solid phase
h	specific enthalpy ($J.kg^{-1}$)
J	melting current density ($A.m^{-2}$)
J	interfacial species transfer rate per unit volume ($kg.m^{-3}.s^{-1}$)
J^{ji}	interfacial species transfer rate per unit volume due to diffusion ($kg.m^{-3}.s^{-1}$)
$J^{\Gamma i}$	interfacial species transfer rate per unit volume due to the phase change ($kg.m^{-3}.s^{-1}$)
k	turbulent kinetic energy ($m^2.s^{-2}$)
K	permeability (m^2)
K_0	permeability constant of the Blake-Kozeny law (m^2)
N_0	nuclei density (m^{-3})
N_g	grain density (m^{-3})

48	p	pressure (Pa)
49	$\bar{\mathbf{u}}_\mathbf{l}$	average velocity of the liquid phase ($m.s^{-1}$)
50	Pr_t	turbulent Prandtl number
51	Sc_t	turbulent Schmidt number
52	**u'**	turbulent velocity of the liquid metal ($m.s^{-1}$)
53		
54	*Greek symbols*	
55	β_S	solutal expansion coefficient ($wt\%^{-1}$)
56	β_T	thermal expansion coefficient (K^{-1})
57	ε	dissipation rate of turbulent kinetic energy ($m^2.s^{-3}$)
58	λ	thermal conductivity ($W.m^{-1}.K^{-1}$)
59	λ_{DAS}	characteristic length of the dendritic structure (m)
60	μ	dynamic viscosity ($kg.m^{-1}.s^{-1}$)
61	σ	electric conductivity ($\Omega^{-1}.m^{-1}$)
62	φ	electric potential (V)
63	ρ	density ($kg.m^{-3}$)
64	ω	solute mass fraction (wt%)
65	Φ	mass production rate per unit volume due to nucleation ($kg.m^{-3}.s^{-1}$)
66	Γ	interfacial phase change rate per unit volume ($kg.m^{-3}.s^{-1}$)
67	*Subscripts*	
68	g	grain density (m^{-3})
69	l	liquid
70	m	mixture

r	radial direction
s	solid
t	turbulent
z	axial direction
θ	orthoradial direction

1 Introduction

The fuel assembly components, including Zirconium alloys, are one of the key elements in the production process in nuclear reactors. Refinement of the metallurgical structure and improvement of the cleanness of Zr alloy ingots are generally achieved by the Vacuum Arc Remelting (VAR) process. The high quality and good performance of the final product are ensured by this manufacturing process, which enables the regulation of the chemical homogeneity

The VAR process, as illustrated in Fig. 1, consists in continuously remelting a consumable electrode. In order to obtain a high quality structural ingot, the composition of the electrode must comply with strict standards. A high power direct current, applied under vacuum, provides an electric arc between the tip of the electrode and the baseplate of a water-cooled copper mold. The intense heat generated by the arc melts the electrode tips that fall into the crucible. The secondary ingot is gradually formed from the liquid metal that falls through the arc plasma. The secondary ingot consists of a liquid metal pool above the solidified part and a mushy zone where solidification takes place.

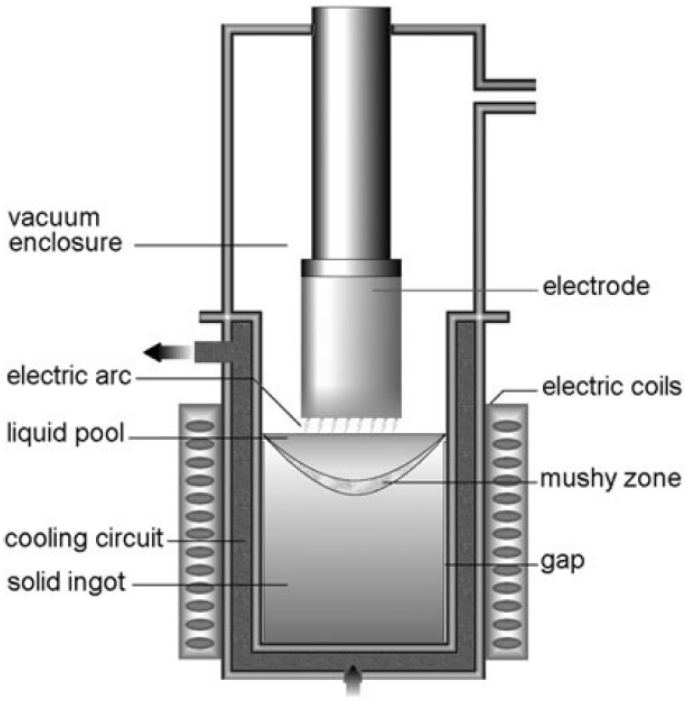

Fig. 1. Schematic representation of a VAR furnace.

In addition, VAR is generally used in the remelting cycles of high quality special steels, as well as Nickel and Titanium alloys.

In the case of Zr or Ti remelting, the arc length is several centimeters. To prevent side-arcing due to these operating conditions, an axial magnetic field is generated by external induction coils. A periodical reversal of the coil current creates a magnetic field that can provide complex electromagnetic stirring of the melt pool. For the standard production of superior-quality Zr alloys for nuclear applications, a VAR operation cycle is applied (up to three times), where each secondary ingot feeds the next remelting as a new consumable electrode.

During solidification, chemical heterogeneities eventually appear in the mushy zone. One of the main challenges in the production of Zr alloys is to control macrosegregation in the VAR process for an optimal quality of the final ingots. Macrosegregation refers to chemical

heterogeneity at the ingot scale and is a combination of microsegregation, i.e. concentration gradient between the solid and liquid phases at the dendritic microscale, and the solute convective transport caused by the liquid metal flow within the mushy zone.

Several numerical models have already been developed to calculate the hydrodynamics of the melt pool in a VAR ingot, including the 2D SOLAR code, as described by Jardy and Ablitzer[1]. The extension of this CFD code forms the basis for the present study.

In addition, an extensive work has also been done to anticipate solidification defects in the remelting products. The SOLAR code was successfully used for simulating VAR and ESR (ElectroSlag Remelting) processes, to predict the risks of white spot and freckle occurrence in the ingot, using a Rayleigh number criterium[2]. The numerical results highlighted the positive impact of an optimized melting rate to minimize the occurrence of freckles.

Wilson and Jardy[3] used the SOLAR model to determine the influence of the alternated electromagnetic stirring sequence on the remelting of Titanium alloys. They presented in-depth numerical studies on several magnetic field stirring patterns during remelting. These numerical results were lately validated by Venkatesh et al.[4] with an industrial campaign dedicated to the remelting of Titanium alloys. The numerical results were successfully validated, based on the measured positions of tungsten markers inside the ingots, providing cavity locations and liquid pool depth for different stirring sequences.

Besides, Chapelle et al.[5] determined the effect of electromagnetic stirring on melt pool free surface dynamics during the remelting of a Zirconium alloy. They observed the behavior of the free surface of the pool for undirectional and alternated stirring. They thus showed that the free surface deformation can affect the quality of the surface of the VAR ingot.

From all these previous studies, it is now well established that the sources of in-place (r, z) motion of the molten pool of a VAR ingot are:

- thermal convection (buoyancy force due to thermal gradients) which tends to favour a flow in a clockwise direction (symmetry axis being on the left),
- the Lorenz force resulting from the interaction between the melting current and the self-induced magnetic field that causes a counterclockwise flow,
- the centrifugal force resulting from the azimuthal motion caused by the interaction between the melting current and the external stirring field. The latter generates a clockwise flow in the (r,z) plane.

Moreover, Revil-Baudard et al.[6] identified the additional potential effect of solute-driven buoyancy force resulting from microsegregation, on macrosegregation.

This paper presents the recent implementation of an improved solidification modelling, based on work of Combeau et al.[7], to provide an enhanced description of macrosegregation phenomena in the ingot.

2 Full-scale VAR trial

For this study, a 2.6 ton Zircaloy-4 (Zy4: Zr-1.3Sn-0.2Fe-0.1O-0.1Cr) VAR ingot of standard size was processed at the Framatome plant (Ugine, France). First, a dedicated electrode was entirely manufactured from recycled materials of the same grade, in order to avoid any chemical heterogeneity. It was noticeable that the mechanical strength of this electrode made of scraps was sufficient throughout the remelting process, so that the trial was carried out without any technical hitch.

The actual recordings of a highly non-standard melting sequence are presented in Figs. 2 and 3, in terms of melting rate and stirring coil current. During the trial, the stirring sequence was carried out in two successive steps: a strong alternating stirring was used to remelt the first 60 %

of the electrode, followed by a weak continuous stirring until the end of the melting process. The magnitude of the alternating stirring was about 4.5 times higher than the continuous stirring one.

Additionally, a strong continuous stirring has been briefly applied at three moments during the alternated stirring stage, in order to mark different pools in the ingot, as such temporary change caused a local change in the grain structure of the solidified material. The profiles of the marked melt pool are clearly visible on calculated composition maps presented in figure 3.c.

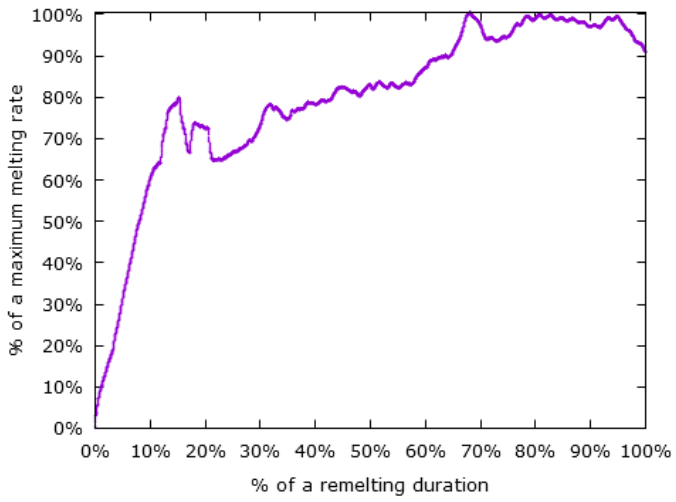

Fig. 2. Melting rate of the full-scale Zy4 remelting trial.

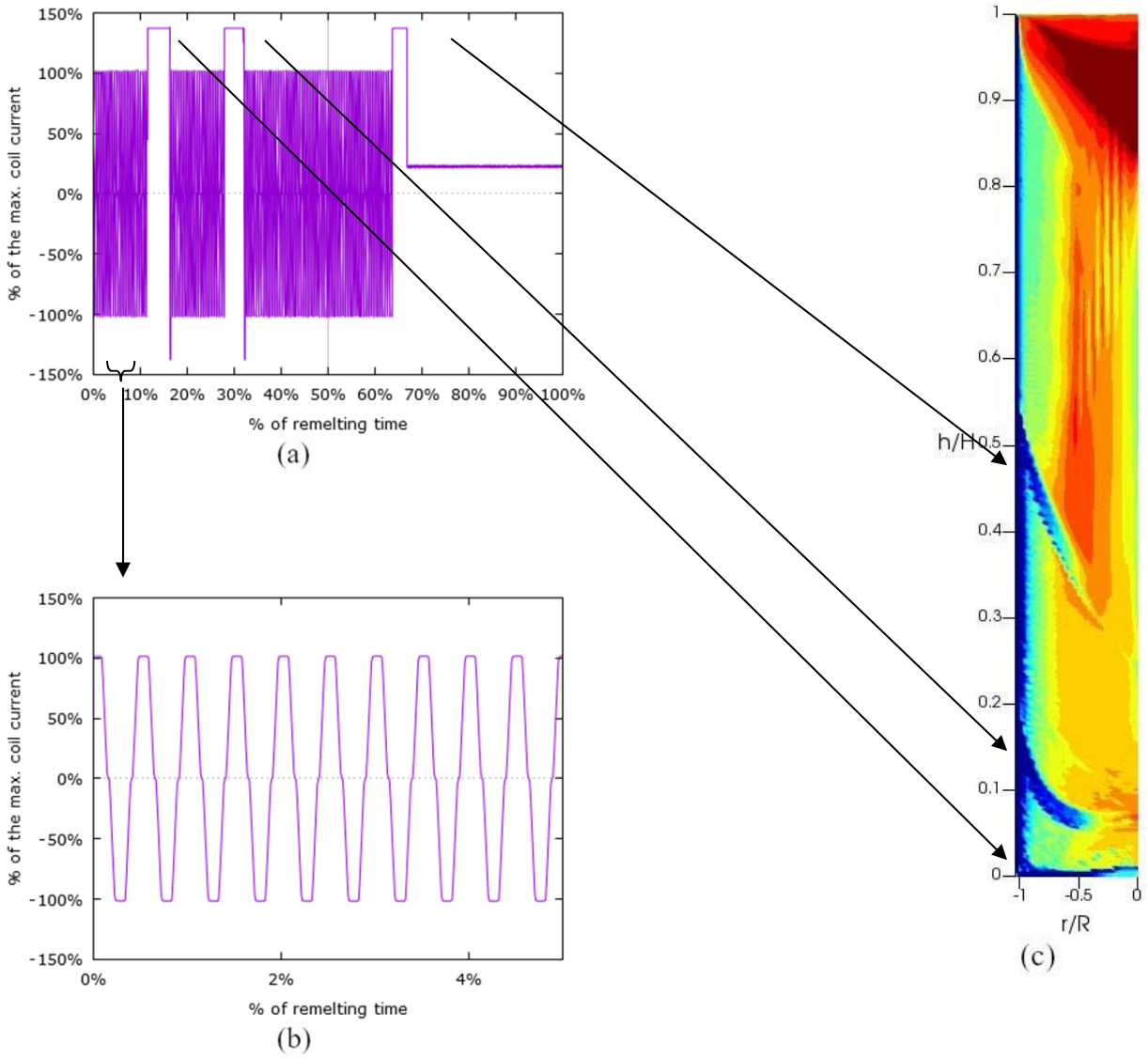

160 **Fig. 3**. Stirring sequence of the full-scale Zy4 remelting trial. (a) Coil current throughout the
161 melt. (b) Detailed alternating stirring sequence. (c) Example of a computed composition map (Zr
162 content), highlighting the melt pool markings in the remelted ingot.

163

164 The remelted ingot was cut longitudinally along its entire length in order to perform
165 chemical analyses and characterize the grain structure. Furthermore, chemical analyses were
166 carried out along several radii at different heights of the ingot, ranging from 0.25 H to 0.88 H,

where H is the total height of the ingot. These measurements are used in section 4 to validate the numerical results.

3 SOLAR model description

3.1 The CFD macromodel

As discussed in section 1, SOLAR is a 2D axisymmetric finite volume model of the VAR process, with the complete set of macroscopic equations presented in Table 1. At a macroscopic scale, the model (Eqs. (1 to 19)) takes into account the transport of heat and solutes coupled with the turbulent flow driven by the electromagnetic stirring, as well as thermal and solute natural convection.

The electromagnetic force $\boldsymbol{F}$ results from the interaction between the melting current $\boldsymbol{J}$, and the magnetic field $\boldsymbol{B}$**.** The latter includes the self-induced magnetic field $B_\theta \boldsymbol{e}_\theta$, and the magnetic field created by the external induction coils $B_{z,ext}\boldsymbol{e}_z$. The current density is in turn calculated from Laplace's conservation equation (Eq. 8) and Ohm's law (Eq. 11). It is important to note that the effect of EM stirring on the free surface dynamics is not considered here, in accordance with the results of Chapelle et al.[5], who show a second-order effect of EM stirring on the deformation of the melt pool free surface. Thermal buoyancy and solutal buoyancy are taken into account by using a conventional Boussinesq approximation (Eq. 12) to describe the variations in density of the liquid phase in the gravity term of the momentum balance equation. In the mushy zone, the solid phase forms a porous matrix, modelled by a Darcy term in the momentum equation (Eq. 4). Permeability is estimated by the Blake-Kozeny law (Eq. 13), where the Asai and Muchi formula is used to describe the permeability constant K_0 (Eq. 17).

190

191 **Table 1.** Main constitutive equations of the CFD macromodel

Averaged total mass balance
$\frac{\partial}{\partial t}(\rho_m) + \nabla \cdot (\rho_l g_l \overline{\boldsymbol{u_l}}) = 0$ (1)
Averaged mass balance of the solid phase
$\frac{\partial}{\partial t}(\rho g_s) = \Gamma_s + \Phi_s\,, \qquad \rho = const$ (2)
Averaged total heat balance
$\frac{\partial}{\partial t}\left(\rho g_s \overline{h_s} + \rho g_l \overline{h_l}\right) + \nabla \cdot \left(\rho g_l \boldsymbol{u_l} \overline{h_l}\right) = \nabla \cdot [(\lambda + g_l \lambda_t) \nabla \bar{T}]$ (3)
Averaged momentum balance for the liquid phase: fluid flow
$\frac{\partial}{\partial t}(\rho g_l \overline{\boldsymbol{u_l}}) + \nabla \cdot (\rho g_l \overline{\boldsymbol{u_l}}\,\overline{\boldsymbol{u_l}}) = -g_l \nabla p^* + \nabla \cdot [(\mu + \mu_t) g_l (\nabla \overline{\boldsymbol{u_l}} + (\nabla \overline{\boldsymbol{u_l}})^T)] - \frac{g_l^2 \mu}{K} \overline{\boldsymbol{u_l}} + g_l \boldsymbol{g} \overline{\rho_l^b} + g_l \boldsymbol{F}_{\mathbf{el}}$ (4)
Averaged solute mass balance for species i in the solid phase
$\frac{\partial}{\partial t}\left(\rho g_s \overline{\omega_s^i}\right) = J_s^{j^i} + J_s^{\Gamma^i}$ (5)
Averaged solute mass balance for species i in the liquid phase
$\frac{\partial}{\partial t}\left(\rho g_l \overline{\omega_l^i}\right) + \nabla \cdot \left(\rho g_l \overline{\boldsymbol{u_l}}\,\overline{\omega_l^i}\right) = \nabla \cdot \left[\left(D_l^i + D_t\right) g_l \nabla \overline{\omega_l^i}\right] + J_l^{j^i} + J_l^{\Gamma^i}$ (6)
Averaged $k - \varepsilon$ turbulence model

$$\frac{\partial}{\partial t}(\rho g_l k) + \nabla \cdot (\rho g_l \boldsymbol{u_l} k) = \nabla \cdot \left[\left(\mu + \frac{\mu_t}{\sigma_k}\right) g_l \nabla k\right] + P_k + D_k + G_k^T + G_k^S - \rho g_l \varepsilon \tag{7}$$

$$\frac{\partial}{\partial t}(\rho g_l \varepsilon) + \nabla \cdot (\rho g_l \boldsymbol{u_l} \varepsilon)$$

$$= \nabla \cdot \left[\left(\mu + \frac{\mu_t}{\sigma_\varepsilon}\right) g_l \nabla \varepsilon\right] + \frac{\varepsilon}{k}[c_1 P_k + c_2 D_k + c_1 c_3 (G_k^T + G_k^S) - c_2 \rho g_l \varepsilon]$$

Laplace conservation equation

$$\nabla^2 \varphi = 0 \tag{8}$$

Mass balance equation at the solid-liquid interface

$$\Gamma_s + \Gamma_l = 0 \tag{9}$$

Solute mass balance at the solid-liquid interface

$$J_s^{j^i} + J_s^{\Gamma^i} + J_l^{j^i} + J_l^{\Gamma^i} = 0 \tag{10}$$

Ohm's law and Lorentz force

$$\boldsymbol{J} = -\sigma \nabla \varphi \qquad \boldsymbol{F_{el}} = \boldsymbol{J} \wedge \boldsymbol{B} = -J_z B_\theta \boldsymbol{e_r} + J_r B_{ext,z} \boldsymbol{e_\theta} + J_r B_\theta \boldsymbol{e_z} \tag{11}$$

Liquid density in the buoyancy force

$$\overline{\rho_l^b} = \rho_{ref}[1 - \beta_T(\overline{T} - T_{ref}) - \sum_i \beta_S^i(\overline{\omega_l^i} - \omega_{ref}^i)] \tag{12}$$

Permeability law

$$K = \frac{g_l^3}{(1 - g_l^2)} K_0 \tag{13}$$

Production rate P_k due to gradients of u_l and dissipation rate D_k due to liquid-solid interaction

$$P_k = -\rho g_l \overline{\boldsymbol{u_i'} \boldsymbol{u_j'}} \frac{\partial}{\partial x_j}(g_l \overline{u_i}) \qquad D_k = -\frac{2\mu g_l^2}{K} k \tag{14}$$

Generation rate due to thermal and solutal buoyancy

$$G_k^T = \beta_T g_l \frac{\mu_t}{Pr_t}\, \boldsymbol{g} \cdot \nabla \overline{T} \qquad G_k^S = \sum_i \beta_S^i g_l \frac{\mu_t}{Sc_t}\, \boldsymbol{g} \cdot \nabla \overline{\omega_l}^i \tag{15}$$

Macroscopic $k-\varepsilon$ model constants

$$Pr_t = 0.85 \quad \sigma_k = 1.0 \quad c_\mu = 0.09 \quad c_3 = \tanh\left(\frac{|\overline{\boldsymbol{u}_{l,z}}|}{\sqrt{\overline{\boldsymbol{u}_{l,\theta}}^2 + \overline{\boldsymbol{u}_{l,r}}^2}}\right) \tag{16}$$

$$Sc_t = 0.7 \quad \sigma_\varepsilon = 1.3 \quad c_1 = 1.44$$

$$c_2 = 1.92$$

Permeability constants of the model

$$K_0 = \frac{\lambda_{DAS}^2}{180} \tag{17}$$

Pressure

$$p^* = \overline{p}_l + \frac{2}{3}\rho k \tag{18}$$

Turbulent parameters

$$\mu_t = c_\mu \rho \frac{k^2}{\varepsilon} \qquad \lambda_t = \frac{c_p \mu}{Pr_t} \qquad D_t = \frac{\mu_t}{\rho Sc_t} \tag{19}$$

A macroscopic RANS two-equation $k-\varepsilon$ model (Eq. 7) is adopted to describe the turbulence of the liquid flow. The transport equations for the mean turbulent kinetic energy k and its corresponding mean dissipation rate ε include:

- turbulence production due to mean velocity gradients P_k (Eq. 14),
- dissipation of turbulence due to the liquid/solid interaction in the mushy zone D_k (Eq. 14),
- production or dissipation of turbulence caused by vertical thermal G_k^T and solute content G_k^S gradients (Eq. 15).

200 The constants used for closure (Eq. 16) correspond to the standard $k-\varepsilon$ model originally
201 developed by Launder and Spalding[8] for a fully liquid medium ($g_l = 1$, hence $K \to \infty$). This
202 approach is suitable for a wide variety of turbulent flows.

203 The closure of such model in the mushy zone, considered as a porous medium, is solved through
204 the formulation of the dissipation term D_k of the turbulence model [9–12]. Precisely, the Prescott
205 and Incropera approach was implemented in the model (eq. 14).

206 The model simulates the direct radiation of the electric arc by the implementation of a heat source
207 as well as a current density on the top face of the secondary ingot.

208 All boundary conditions are discussed in the PhD theses by Hans[13], Quatravaux[14] and Revil-
209 Baudard[15].

210 The mesh used for all simulations reported in this paper is a structured one. The number of cells
211 must increase during the simulation to follow the ingot growth, as the material input from the
212 electrode melting is modeled by an advection-like term, i.e. a cell split and growth method. The
213 resulting mesh is scalable, both in size and number of cells, describing at each time step the ingot
214 growth in a continuous way. More details are available in Quatravaux's Ph D thesis[14].

215 **3.2 The solidification micromodel**

216 The solidification micromodel is derived from the approach of Beckerman and
217 Viskanta[16]. They proposed a mathematical formulation for dendritic solidification in a binary
218 mixture. Their micro-model was based on a two-phase volume-averaged formulation and results
219 were compared to shadowgraph images of the experimental solidification of an ammonium
220 chloride solution in water. Although the numerical results were qualitatively close to

221 experimental measurements, the quantitative values for temperature and concentrations showed
222 considerable differences.

223 Lately, an improved model was presented by Wang and Beckerman[17]. They described
224 equiaxed dendritic solidification by considering the convection and solid phase transport. This
225 model accounts for the nucleation, grain growth and dendrite morphology by solving a set of
226 transport equations for solid, interdendritic, and extradendritic phases. However, the model was
227 only validated at the laboratory scale.

228 A similar approach, based on decoupling physical phenomena according to the micro and
229 macro time-scale, was presented by Zaloznik and Combeau[18] for a real industrial size ingot. The
230 constitutive equations of the models were obtained by introducing a Representative Elementary
231 Volume (REV), averaging the transport equations of heat, mass, and momentum over the
232 individual (liquid, solid) phases. The process model considers mass transfer, turbulent fluid flow,
233 heat transfer, electromagnetism and phase change using the following main assumptions:
234 - the local thermal equilibrium is assumed in each mesh cell, which behaves as a REV;
235 - the solidification shrinkage is not considered, because the densities of both phases are equal and
236 constant, except for the buoyancy terms where the Boussinesq approximation is applied;
237 - the solid phase is considered rigid and fixed;
238 - the thermophysical properties of all alloys are constant; in particular, partition coefficients and
239 liquidus slopes are independent of the temperature and composition.

240 An operator splitting scheme, described in detail in Založnik and Combeau[18], was used
241 to define the transport and growth stages. In the first one, the convective/diffusive macroscopic
242 transport partial differential equations were solved globally by neglecting nucleation and growth
243 terms, while in the second one, the contributions of nucleation and growth were solved locally
244 and initialized from the transport stage. The grain growth model was highly nonlinear and

therefore required special attention. The advantage of this approach was the decoupling of macro and micro time scales, which allows the grain growth model to be solved separately.

The microscopic terms that described the grain nucleation and growth were treated locally within each mesh cell where the interfacial chemical and thermal equilibrium were assumed to be reached: $T_s = T_l = T$ and $\omega_s^{i^*} = k_p \omega_l^{i^*}$. The interfacial compositions and temperatures are correlated by considering a simplified multicomponent phase diagram, where the liquidus temperature is described with a linear dependence on all alloy components. Both the liquidus slopes m_l^i and partition coefficient k_p^i are constant. Therefore, the solidification process starts when the enthalpy of a cell falls below the liquidus enthalpy h_{liq},

$$h_{liq} = c_p\left(T_m + \sum_{i=1}^{n_{sol}} m_L^i \omega_l^i\right) + L_f \tag{20}$$

and stops when the temperature drops below a fixed temperature T_{sol0} or when the solid fraction reaches $g_s = 1$ due to the primary growth as explained by Založnik and Combeau[18].

In the solidification interval, where the liquid and solid phases co-exist in the same REV ($0 < g_s < 1$), the solidification micromodel takes into account finite solute diffusion in both phases and considers two separate regions: the solid phase and the extra-dendritic liquid. In the mushy zone, grains are assumed to be spherical, the velocity of the extra-dendritic phase to be equal to the averaged velocity of the liquid, and the diffusivity of each solute to be constant in each phase. Grain generation is modelled by an instantaneous nucleation model, which assumes that a predefined number of grains per unit volume N_g with an initial radius R^* nucleate when the local temperature becomes lower than the local liquidus temperature (see Eq. 25 in Table 2). The

transfer of the interfacial solute due to the phase change (solidification or melting) is given in Eq. 21:

$$\left(k_p^i - 1\right)\omega_l^{i*}\frac{\Gamma_s}{\rho} + \omega_l^{i*}\left(\frac{S_v D_l^n}{\delta_l} + k_p^n\frac{S_v D_s^n}{\delta_s}\right) = \omega_l^i\frac{S_v D_l^n}{\delta_l} + \omega_s^i\frac{S_v D_s^n}{\delta_s}. \quad (21)$$

During primary solidification, the diffusion flux at the solid/liquid interface is described by a simplified model: solute gradients are calculated by dividing the difference of the solute mass fraction at the interface $\omega_k^{*,i}$ and the average mass fraction ω_k^i, by a diffusion length δ_k. An approximation is used to estimate the boundary layer thickness in the solid phase while a stagnant film model is used to describe the boundary layer thickness in the liquid phase. This solidification micromodel, whose main equations are given in Table 2 (Eqs. 22-28), is described in detail by Tveito et al.[19]. It must be stated here that its implementation in SOLAR software represents an innovative approach over the previous versions used to simulate the VAR process.

Table 2. Main equations of the solidification micromodel.

Geometrical relations and surface area
$R^* = \left(\frac{3g_s}{4\pi N_g}\right)^{\frac{1}{3}}$ $\quad R_f = \left(\frac{3}{4\pi N_g}\right)^{\frac{1}{3}}$ $\quad S_v^* = 4\pi R^{*2} N_g$ (22)
Dendrite tip kinetics
$\Omega_i = \frac{\omega_l^{*,i} - \left[<\omega_s^i>^e\right]^{gr}}{\omega_l^{*,i}\left(1 - k_p^i\right)}$ $\quad V = \frac{\partial R^*}{\partial t}$ $\quad \Gamma_s = \rho_s S_v^* V$ (23)
Boundary layer thickness

$$\delta_i^l = \frac{d_i}{\left(\frac{d_i}{R^*} - \frac{f(R^*,\Delta_i)+g(R_f,R^*,\Delta_i)}{d_i(R^*+d_i-(R^*-\Delta_i+d_i)exp^{-\frac{\Delta_i}{d_i}})-f(R^*,\Delta_i)+(exp^{-\frac{\Delta_i}{d_i}}-1)g(R_f,R^*,\Delta_i)}\right)} \quad (24)$$

$$\delta_i^s = \frac{R^*}{5} \qquad g\left(R_f,R^*,\Delta_i\right) = \frac{R_f^3-(R^*+\Delta_i)^3}{3(R^*+\Delta_i)} \qquad d_i = \frac{D_l^i}{V}$$

$$Sh_i = \frac{2}{3(1-g_s)} Sc_i^{\frac{1}{3}} Re^{n(Re)} \qquad f(R^*,\Delta_i) = \frac{1}{2}((R^*+\Delta_i)^2-(R^*)^2) \qquad \Delta_i = \frac{2R^*}{Sh_i}$$

$$Re = \frac{\rho_l(1-g_s)2R^*}{\mu_l}|\overline{\boldsymbol{u_l}}| \qquad n(Re) = \frac{2Re^{0.28}+4.65}{3(Re^{0.28}+4.65)} \qquad Sc_i = \frac{\mu_l}{\rho_l D_l^i}$$

Thermodynamics

$$\omega_{s-d}^{*,i} = \omega_l^{*,i} k_p^i \qquad T_l = T_m + \sum_i m_l^i \omega_l^{*,i} \quad (25)$$

Nucleation

$$\Phi_s = \begin{cases} \rho \frac{\pi R^{*3}}{6} N_g \delta(t-t_0); \text{ if } T_l < T_m + \sum_i m_l^i \omega_l^{*,i} \text{ and } g_s = 0 \\ 0; \text{ else} \end{cases} \qquad \Phi_s = -\Phi_l \quad (26)$$

Solute fluxes due to phase change

$$J_s^{\Gamma^i} = \omega_s^{*,i}\Gamma_s \qquad J_l^{\Gamma^i} = \omega_l^{*,i}\Gamma_l \qquad \omega_s^{*,i} = k_p^i \omega_l^{*,i} \quad (27)$$

Solute fluxes due to diffusion

$$J_s^{j,i} = \frac{S_v^* \rho_s D_s^i}{\delta_s}(\omega_s^{*,i} - \omega_s^i) \qquad J_l^{j,i} = \frac{S_v^* \rho_l D_l^i}{\delta_l}(\omega_l^{*,i} - \omega_l^i) \quad (28)$$

4 Numerical results and discussion

The full-scale melt of a Zy4 electrode (see Section 2) was simulated using the model fully described in Section 3. A complete set of process operating parameters (melting rate, arc voltage, melting current and current in the external induction coils) was previously recorded during the

282 industrial trial to feed all simulations presented in this section. The operating parameters were
283 entered by means of data files containing these records (see Figures 2 and 3).

284 The thermophysical properties of Zy4 used in the simulations are given in Table 3. Note
285 that the solidification properties (partition coefficients and liquidus slopes) have been extracted
286 from the binary phase diagrams for Zr-X alloys[20]. Unless otherwise specified, the values of β_S^{Sn}
287 and λ_{DAS} used in the simulations (default values) are also reported in Table 3.

288

289

290 **Table 3.** Thermophysical properties of Zy4 used in the simulations

Nominal compositions	Sn	ω_0^{Sn}	[wt%]	1.3
	Fe	ω_0^{Fe}	[wt%]	0.2
	O	ω_0^{O}	[wt%]	0.1
	Cr	ω_0^{Cr}	[wt%]	0.1
Melting temperature of pure Zr		T_m	[°C]	1855
Liquidus slopes	Sn	m_l^{Sn}	[°C(wt%)$^{-1}$]	-11
	Fe	m_L^{Fe}	[°C(wt%)$^{-1}$]	-57
	O	m_L^{O}	[°C(wt%)$^{-1}$]	147
	Cr	m_L^{Cr}	[°C(wt%)$^{-1}$]	-26
Partition Coefficients	Sn	k_p^{Sn}	[-]	0.27
	Fe	k_p^{Fe}	[-]	0.25
	O	k_p^{O}	[-]	2.32

	Cr	k_p^{Cr}	[-]	0.15
Diffusion coefficients in the liquid	Sn	D_l^{Sn}	[$m^2.s^{-1}$]	$1 \cdot 10^{-8}$
	Fe	D_l^{Fe}	[$m^2.s^{-1}$]	$1 \cdot 10^{-8}$
	O	D_l^{O}	[$m^2.s^{-1}$]	$1 \cdot 10^{-8}$
	Cr	D_l^{Cr}	[$m^2.s^{-1}$]	$1 \cdot 10^{-8}$
Diffusion coefficients in the solid	Sn	D_s^{Sn}	[$m^2.s^{-1}$]	$4.9 \cdot 10^{-11}$
	Fe	D_s^{Fe}	[$m^2.s^{-1}$]	$1.5 \cdot 10^{-9}$
	O	D_s^{O}	[$m^2.s^{-1}$]	$3.8 \cdot 10^{-9}$
	Cr	D_s^{Cr}	[$m^2.s^{-1}$]	$1.3 \cdot 10^{-9}$
Temp. of end of solidification		T_{sol}	[°C]	1592
Latent heat		L_f	[$J.kg^{-1}$]	$2.42 \cdot 10^{5}$
Reference density		ρ_0	[$kg.m^{-3}$]	6210
Dynamic viscosity		μ	[Pa.s]	$4.59 \cdot 10^{-3}$
Thermal conductivity		λ	[$W.m^{-1}.°C^{-1}$]	36.5
Thermal expansion coefficient		β_T	[$°C^{-1}$]	$4 \cdot 10^{-5}$
Specific heat		c_p	[$J.kg^{-1}.°C^{-1}$]	435
Electric conductivity		σ	[$m^{-1}.\Omega^{-1}$]	$6.8 \cdot 10^{5}$
Solute expansion coefficients	Sn	β_S^{Sn}	[$(wt\%)^{-1}$]	$3 \cdot 10^{-2}$
	Fe	β_S^{Fe}	[$(wt\%)^{-1}$]	0
	O	β_S^{O}	[$(wt\%)^{-1}$]	0
	Cr	β_S^{Cr}	[$(wt\%)^{-1}$]	0
Characteristic length of the		λ_{DAS}	[m]	$134 \cdot 10^{-6}$

dendritic structures

For all simulations reported in the present paper, the average cell size was approximately 9 mm wide and 6 mm height. Mesh refinement was applied with a geometrical reason of 0.8 on the five nodes closest to the mold as well as to the free surface. The time-step was fixed to 0.025 s.

The computational time required for simulating a full melt depends on the computer. In the IJL facility, the total CPU time was around 72 hours.

In several previous publications [2,21–23], the authors have detailed some CFD macromodel results when applied to various remelting situations. In this paper, the attention will be focused on the fluid flow in the liquid pool and the mushy zone, as well as the resulting macrosegregation.

4.1 Hydrodynamics in the liquid metal pool

The purpose of this section is to numerically study the influence of the thermal and solutal buoyancy forces on the flow in the liquid bath during remelting. Mean velocity field, turbulence generation are therefore investigated. Only the effect of local Sn content on solutal buoyancy was considered, as the concentrations in all other alloying elements are negligible.

4.1.1. Assumptions on the thermal and solutal buoyancy forces

During solidification, a buoyancy driving force can be generated either by the thermal or solutal buoyancy effects, that can be collaborating or opposing [24]. Both buoyancy effects are modelled by the Boussinesq approximation (Eq. 12), therefore both the thermal and the solutal expansion coefficients had to be estimated.

Unfortunately, values for the solutal and thermal expansion coefficient for Zy-4 alloy and its alloying elements are not readily available in the literature.

The thermal expansion has been estimated from values measured by Paradis and Rhim[25] on pure Zr. Moreover, other pertaining physical properties, such as reference density, come from this reference.

Figures 4 and 5 below show the evolution of Zr density and Sn density with the temperature.

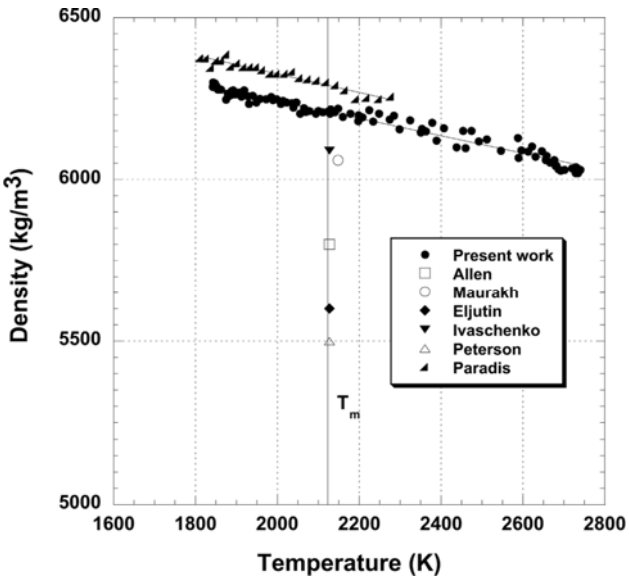

Fig. 4. Density of Zr as a function of temperature, from [26] (the vertical bar corresponds to Zr melting point).

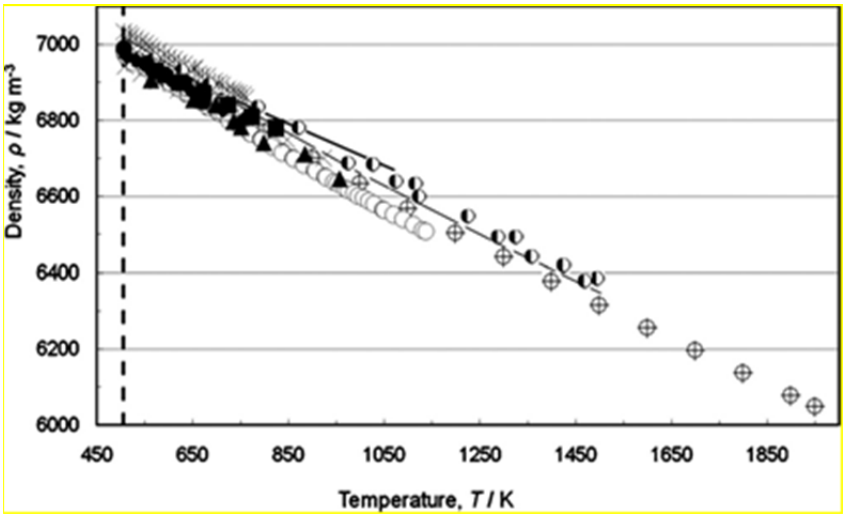

Fig. 5. Density of Sn as a function of temperature, from [27] (the vertical bar corresponds to Sn melting point).

From these figures, it is not possible to decide with a great confidence whether Sn should be considered as heavier or lighter than Zr at high temperature, around 2128 K, i.e. Zr melting temperature. Clearly, the value of the solutal expansion coefficient cannot be readily given.

In order to examine the influence of thermo-solutal convection, four simulations have been run, as shown in Table 4. In Case A, both buoyancy terms were null, which means that the flow is only driven by the forced convection generated by the electromagnetic field. In case B, thermal expansion coefficient for pure Zr has been used, while no solutal buoyancy was applied. Cases C and D take into account solutal buoyancy, with a negative (case C) and positive (case D) value of the Sn expansion coefficient. The negative coefficient $\beta_S^{Sn} = -1 \cdot 10^{-2}(wt\%)^{-1}$, defined in case C, was chosen to investigate on the consequences of cooperating buoyancy forces. On the contrary, the positive value in case D implies opposing buoyancy forces.

Table 4. Definition of the four simulations run to study the effect of thermo-solute convection

case	$\beta_T\ [°C^{-1}\ ]$	$\beta_S^{Sn}[wt\%^{-1}]$
A	0	0
B	$4 \cdot 10^{-5}$	0
C	$4 \cdot 10^{-5}$	$-1 \cdot 10^{-2}$
D	$4 \cdot 10^{-5}$	$3 \cdot 10^{-2}$

339

340 **4.1.2 Characteristics of the liquid metal pool**

341 The metal flow in the melt pool and mushy zone has been investigated at instants
342 corresponding to alternated or continuous stirring periods applied during the melt. In the latter
343 case, the hydrodynamics in the (r, z) plane is quite stationary, whereas in the former one, two
344 different moments have been considered during the stirring sequence:

345 - time t_1 is characterized by a low azimuthal velocity of the liquid, hence a low centrifugal force

346 - time t_2 is characterized by a high azimuthal velocity of the liquid, hence a high centrifugal force.

347 Flows during the continuous stirring stage (time t_3) and at time t_2 are similar, since the
348 azimuthal velocity in both cases is high (see Fig. 6). However, as can be seen in Fig. 6,
349 the transition from alternated to continuous stirring changes the depth and shape of the
350 liquid pool as well as the size of the mushy zone. In the case of alternated stirring, the
351 liquid pool is shallower and more parabolic in shape, whereas in the case of continuous
352 stirring, the pool is deeper and cone-shaped, with a larger mushy zone.

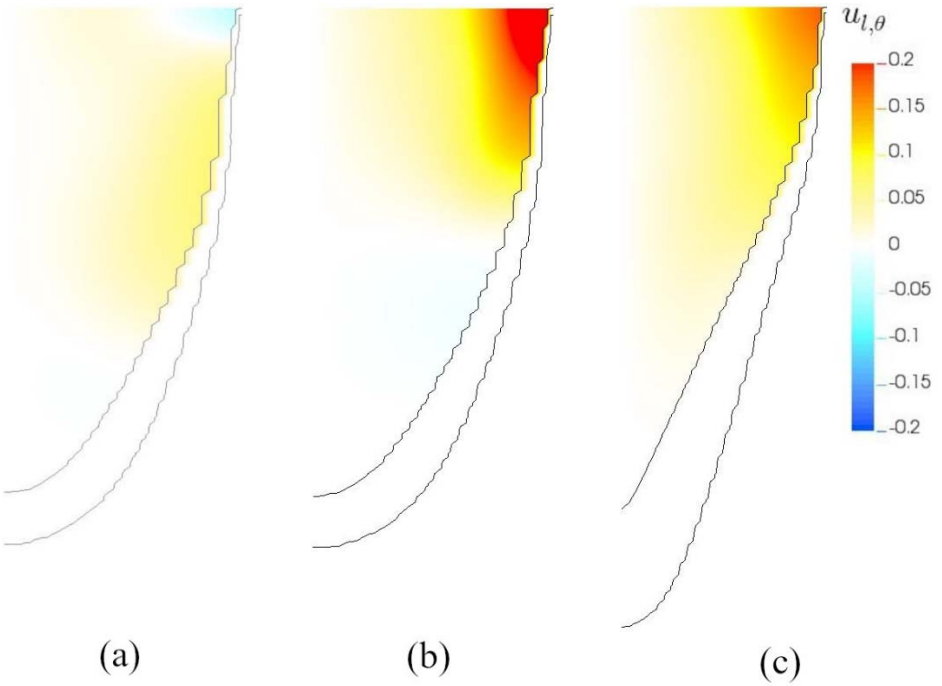

Fig. 6. Case A – Computed pool profile and azimuthal velocity (m.s^{-1}) map in the melt pool at 3 different moments during the melt. (a) Time t_1 - alternated stirring, low azimuthal velocity. (b) Time t_2 - alternated stirring, high azimuthal velocity. (c) Time t_3 - continuous stirring, high azimuthal velocity.

The hydrodynamic behavior at time t_1 (low azimuthal velocity) is the object of Fig. 7. The turbulence intensity is represented by the μ_t/μ viscosity ratio and the velocity field by velocity vectors in the upper part of the melt pool where velocities are high and by streamlines in the lower part of the melt pool and in the mushy zone, where velocities are significantly lower.

Without any buoyancy phenomena, the electromagnetic force causes two recirculation loops (Fig. 7 (a)). The interaction between the melting current and the self-induced magnetic field generates centripetal forces localized in the near-surface region, at the origin of a counter-

365 clockwise recirculation flow of the liquid metal in the upper part of the pool. In the mid-height
366 zone of the pool, stirring centrifugal forces prevail, reinforcing the upper recirculation flow and
367 creating a second clockwise loop in the lower part of the pool.

368 When thermal buoyancy is added (case B), it can be seen in fig. 7(b) that the two
369 recirculation loops remain qualitatively identical. The major modification is a strong decrease in
370 the turbulence intensity in the near-surface region, as the high vertical thermal stratification
371 strongly dissipates turbulence (eq. 15).

372 Turbulence characteristics of the flow is almost identical to case B when solute buoyancy
373 is added (cases C and D).

374 The collaborating solute buoyancy has a negligible impact on the “two recirculation
375 loops” system observed for cases A and B. However, in case D, the opposing solute buoyancy
376 leads to the apparition of a third counter-clockwise recirculation flow in the bottom of the pool
377 and in the mushy zone. As Sn partition ratio is lower than unity, solute redistribution during
378 solidification causes a liquid enrichment in solute in the mushy zone. This enrichment causes a
379 decrease in liquid density due to the positive solutal expansion coefficient. Finally, the resulting
380 solutal buoyancy force, localized in the mushy zone, promotes an upward flow along the
381 solidification front, inducing the observed third bottom loop.
382

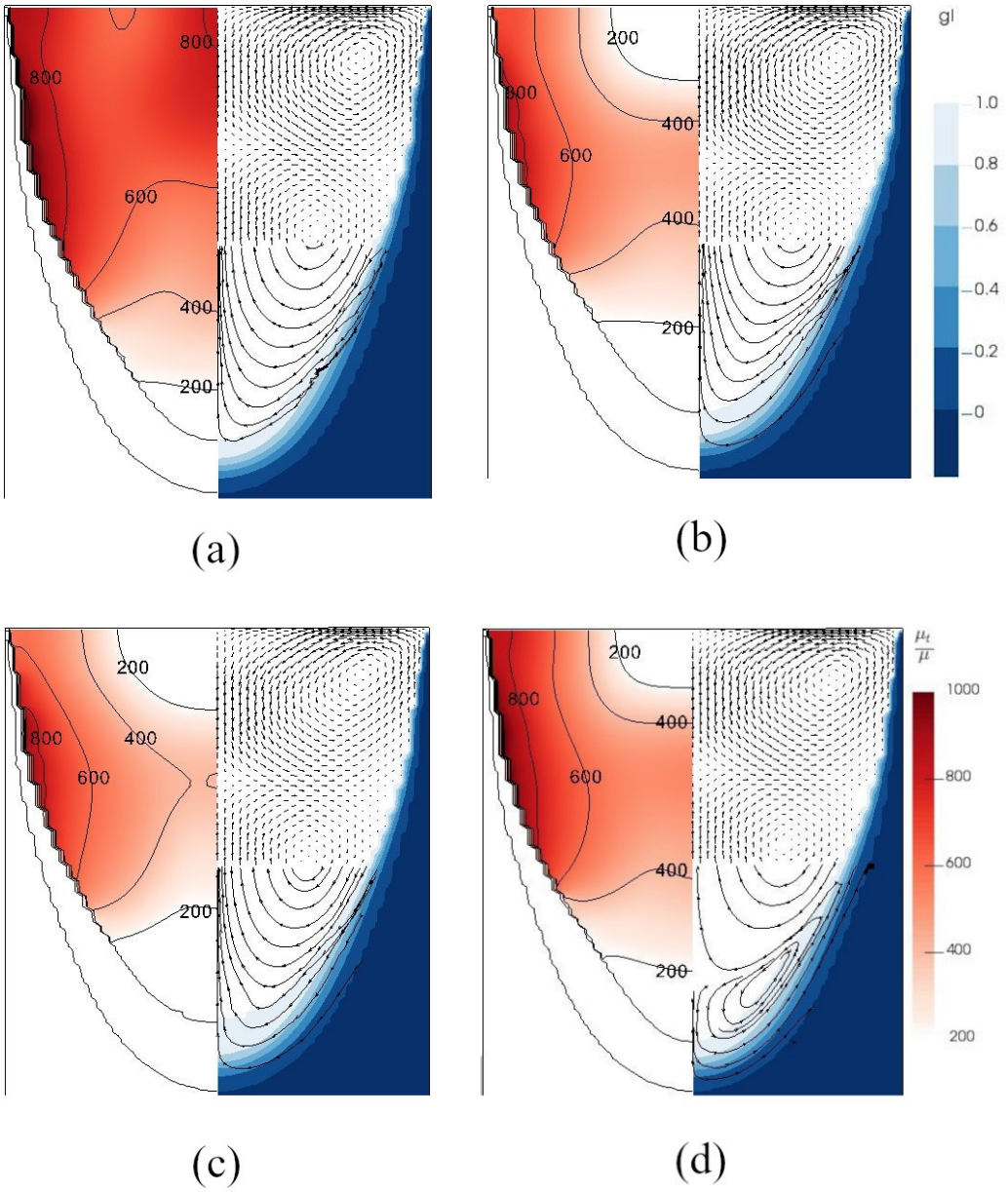

383 **Fig. 7**. Computed flow in the melt pool and mushy zone at time t_l (alternated stirring, low
384 azimuthal velocity). Left side is the turbulence intensity and right side is the mean flow
385 represented by vectors (pool upper part) or streamlines (pool lower part and mushy zone) and the
386 liquid fraction map. (a) Case A: $\beta_T = 0$, $\beta_S^{Sn} = 0$, $v_{max} = 2.03\ cm.s^{-1}$. (b) Case B: $\beta_T = 4 \cdot$
387 $10^{-5}\ °C^{-1}$, $\beta_S^{Sn} = 0$, $v_{max} = 1.60\ cm.s^{-1}$. (c) Case C: $\beta_T = 4 \cdot 10^{-5}\ °C^{-1}$, $\beta_S^{Sn} = -1 \cdot$

388 10^{-2} $wt\%^{-1}$, $v_{max} = 1.82$ $cm.s^{-1}$. (d) Case D: $\beta_T = 4 \cdot 10^{-5}$ $°C^{-1}$, $\beta_S^{Sn} = 3 \cdot 10^{-2}$ $wt\%^{-1}$,

389 $v_{max} = 1.61$ $cm.s^{-1}$.

390

391 The influence of a high azimuthal velocity on the in-plane velocity field and turbulence

392 intensity in the melt pool and mushy zone is shown in Figs. 8 and 9, for instants t_2 during the

393 alternated stirring and t_3 during the continuous stirring.

394 Compared to the previous case, azimuthal velocity generated by the stirring is 60 %

395 higher, implying an increase in centrifugal forces of 156 %. Therefore, the self-induced forces

396 become of second order and, thus, the circulation counter-clockwise loop in the near surface

397 region disappears.

398 Similar to previous simulations, the introduction of thermal buoyancy forces considerably

399 reduces the intensity of turbulence in the near-surface area (cases B, C and D).

400 A collaborative solutal buoyancy slightly decreases turbulence intensity in the bottom of

401 the pool in case C in the frame of a strong alternated stirring (Fig. 8(c)). This is due to the local

402 vertical solute stratification, in the same way as the effects of thermal buoyancy near the free

403 surface.

404 Finally, an opposite solutal buoyancy generates an additional recirculation loop in the

405 bottom of the pool for all stirring conditions (Fig. 8(d) and Fig. 9(d)).

406

407

408

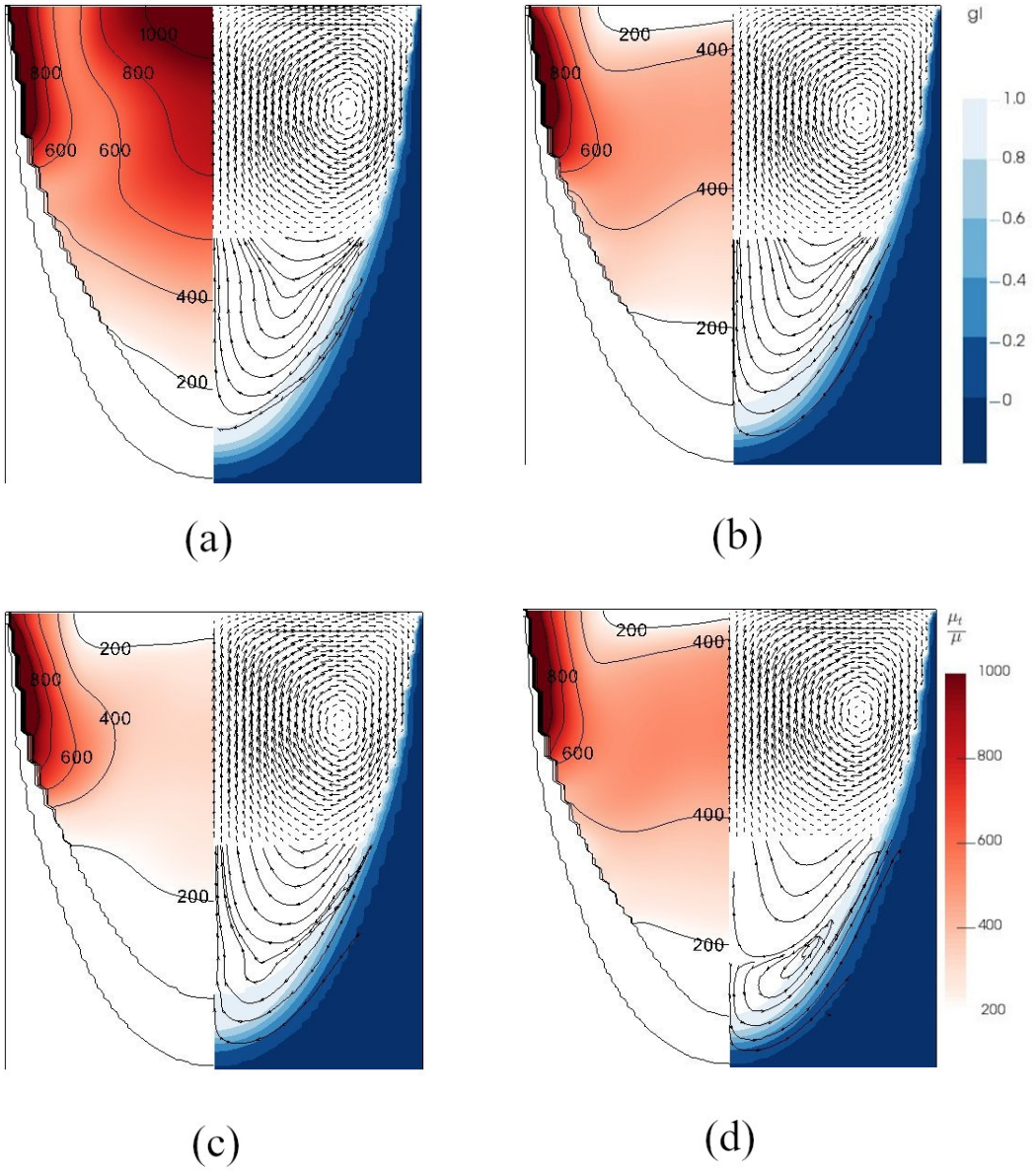

409 **Fig. 8**. Computed flow in the melt pool and mushy zone at time t_2 (alternated stirring, high
410 azimuthal velocity). Left side is the turbulence intensity and right side is the mean flow
411 represented by vectors (pool upper part) or streamlines (pool lower part and mushy zone) and the
412 liquid fraction map. (a) Case A: $\beta_T = 0$, $\beta_S^{Sn} = 0$, $v_{max} = 2.53$ cm.s^{-1}. (b) Case B: $\beta_T = 4 \cdot$
413 10^{-5} °C^{-1}, $\beta_S^{Sn} = 0$, $v_{max} = 2.53$ cm.s^{-1}. (c) Case C: $\beta_T = 4 \cdot 10^{-5}$ °C^{-1}, $\beta_S^{Sn} = -1 \cdot$

414 10^{-2} wt%$^{-1}$, $v_{max} = 2.50$ cm.s^{-1}. (d) Case D: $\beta_T = 4 \cdot 10^{-5}$ °C^{-1}, $\beta_S^{Sn} = 3 \cdot 10^{-2}$ wt%$^{-1}$,

415 $v_{max} = 2.51$ cm.s^{-1}.

416

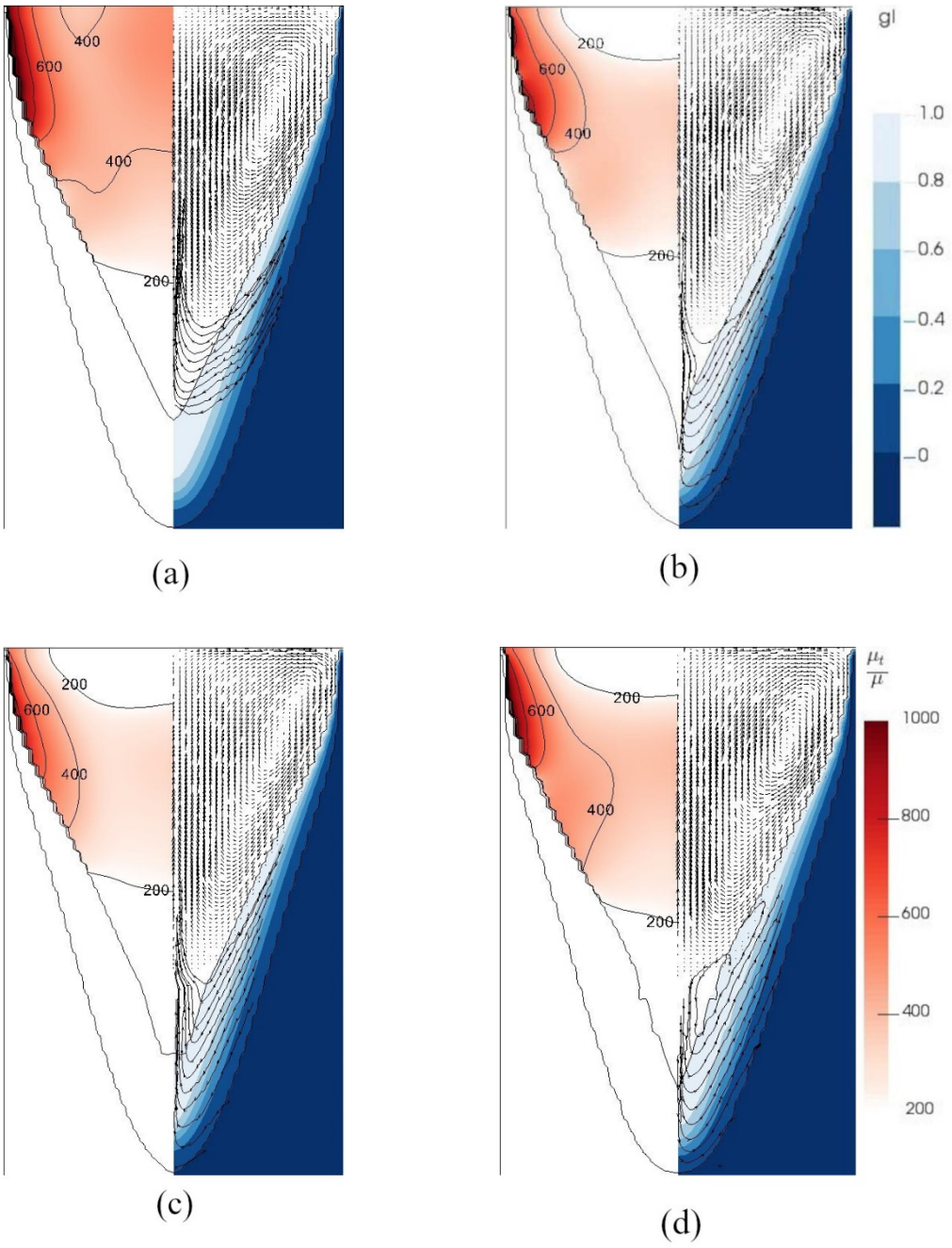

417 **Fig. 9**. Computed flow in the melt pool and mushy zone at time t_3 (continuous stirring, high

418 azimuthal velocity). Left side is the turbulence intensity and right side is the mean flow

represented by vectors (pool upper part) or streamlines (pool lower part and mushy zone) and the liquid fraction map. (a) Case A: $\beta_T = 0$, $\beta_S^{Sn} = 0$, $v_{max} = 2.02$ cm.s^{-1}. (b) Case B: $\beta_T = 4 \cdot 10^{-5}$ °C^{-1}, $\beta_S^{Sn} = 0$, $v_{max} = 1.93$ cm.s^{-1}. (c) Case C: $\beta_T = 4 \cdot 10^{-5}$ °C^{-1}, $\beta_S^{Sn} = -1 \cdot 10^{-2}$ wt%$^{-1}$, $v_{max} = 1.83$ cm.s^{-1}. (d) Case D: $\beta_T = 4 \cdot 10^{-5}$ °C^{-1}, $\beta_S^{Sn} = 3 \cdot 10^{-2}$ wt%$^{-1}$, $v_{max} = 2.00$ cm.s^{-1}.

4.2. Macrosegregation

Macrosegregation behaviour of the remelted product is now numerically investigated. Particular attention is paid to the influence of the thermophysical properties defined in the macromodel, such as thermal and solutal buoyancy forces, as well as the solidification properties implemented in the micromodel, such as dendrite arm spacing and grain growth kinetics.

As computed results differed only slightly from previous calculations[28], where a simplified solidification model assumed complete diffusion of all solutes in both liquid and solid phases (i.e. lever rule), it appears that the use of a detailed solidification micromodel confirmed the trends which had been highlighted with a simplified lever-rule based model.

4.2.1. Influence of the thermo-solutal convection

The computed maps of Sn content in the final ingot are shown in Fig. 10. As discussed previously, the two declined Sn-depleted bands are a consequence of the strong electromagnetic stirring (see Fig. 3 (b)) that was applied to mark the melt pool profile in the ingot macrostructure. The average concentration of Sn in the liquid pool increases as the ingot grows because the

partition coefficient k_p^{Sn} is lower than 1. Solidification of the last liquid pool causes a local enrichment at the top of the ingot. A strong negative segregation is predicted at the lateral surface and at the bottom of the ingot. However, results at the periphery must be handled with care because the segregation calculated there is very sensitive to mesh size.

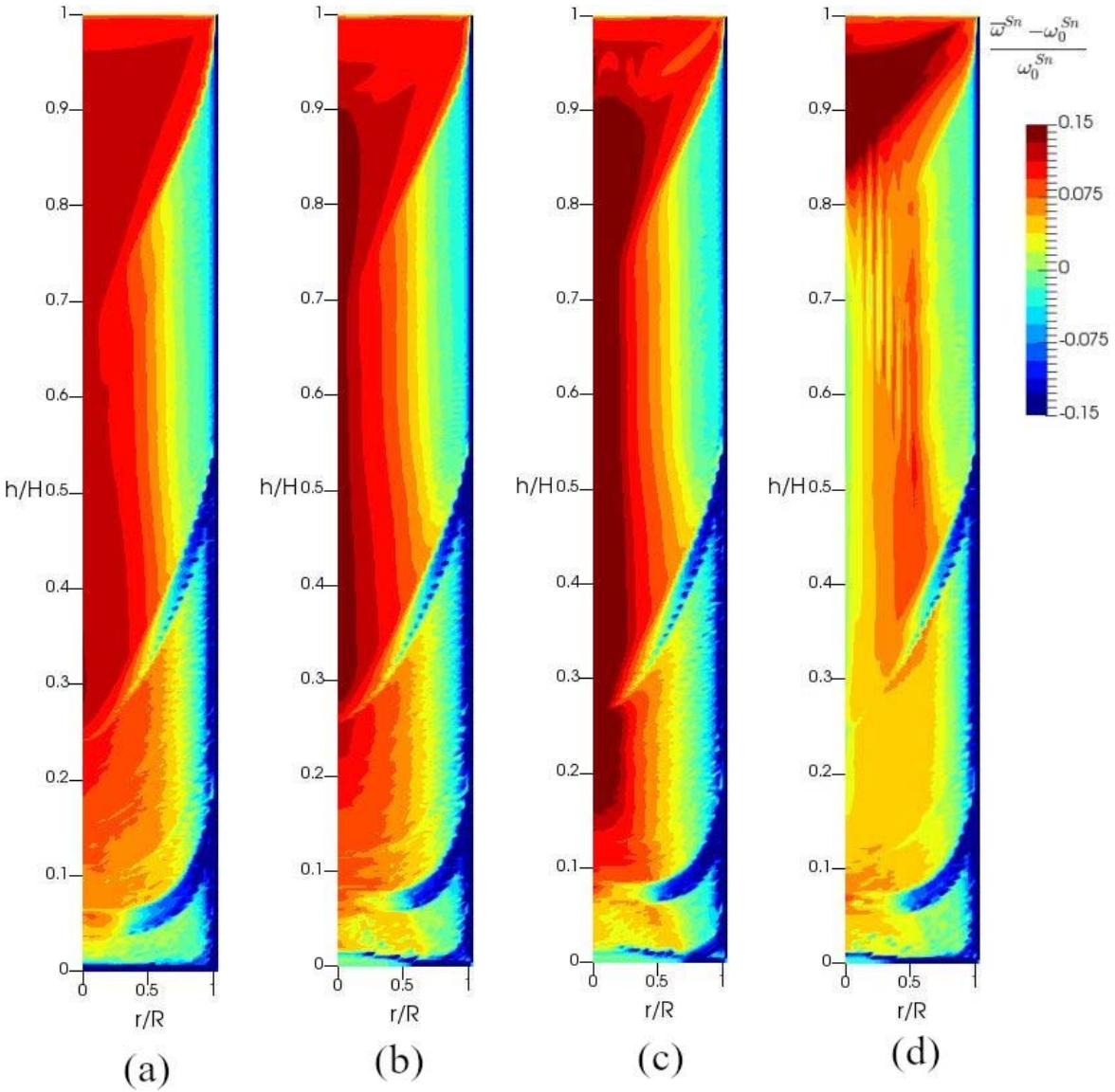

Fig. 10. Computed Sn content map in the remelted ingot. (a) Case A: $\beta_T = 0$, $\beta_S^{Sn} = 0$. (b) Case B: $\beta_T = 4 \cdot 10^{-5}\ °C^{-1}$, $\beta_S^{Sn} = 0$. (c) Case C: $\beta_T = 4 \cdot 10^{-5}\ °C^{-1}$, $\beta_S^{Sn} = -1 \cdot\ 10^{-2}\ wt\%^{-1}$. (d) Case D: $\beta_T = 4 \cdot 10^{-5}\ °C^{-1}$, $\beta_S^{Sn} = 3 \cdot 10^{-2}\ wt\%^{-1}$.

In the absence of buoyancy (case A), the model predicts a Sn enrichment in the ingot centre for the two stirring regimes used during the melt. This is the result of the clockwise flow measurement cell discussed in the previous section. The liquid flows down along the solidification front. As a result, the liquid enriched in Sn piles up in the mushy zone and at the bottom of the melt pool, resulting in a positive segregation on the axis of symmetry. As shown in Fig. 10, radial macrosegregation is weaker with alternating stirring than with continuous stirring.

The addition of thermal convection (case B) slightly increases the radial macrosegregation for both stirring sequences. The centrifugal force is reinforced by thermal buoyancy, which causes more intense circulation in the mushy zone and greater transport of enriched liquid to the central axis.

The convection effects induced by the solutal buoyancy are presented in Figs. 10 (c) and 10 (d). They prevail in the central part of the mushy zone and have an impact on segregation. In case C, the segregation at the central axis is notably amplified by the cooperation of solutal and thermal buoyancy. The opposite effect is observed in case D, where the effects of solutal and thermal buoyancy are opposed: the segregation at the central axis is considerably reduced, due to the upward flow in the mushy region. A positive segregation band is therefore located at $r/R \sim 0.5$.

Moreover, in case D, during the continuous stirring sequence, a series of vertical channels appear in the enriched segregation part. Fig. 11 details this effect. The Sn-enriched liquid

accumulated near the centerline is transported outward under the influence of solutal convection. This transport of solute is effective for a liquid fraction $g_l > 0.6$. When $g_l < 0.6$, the permeability of the porous media decreases rapidly as the drag forces dominate inertial and buoyancy forces and macrosegregation evolution is stopped.

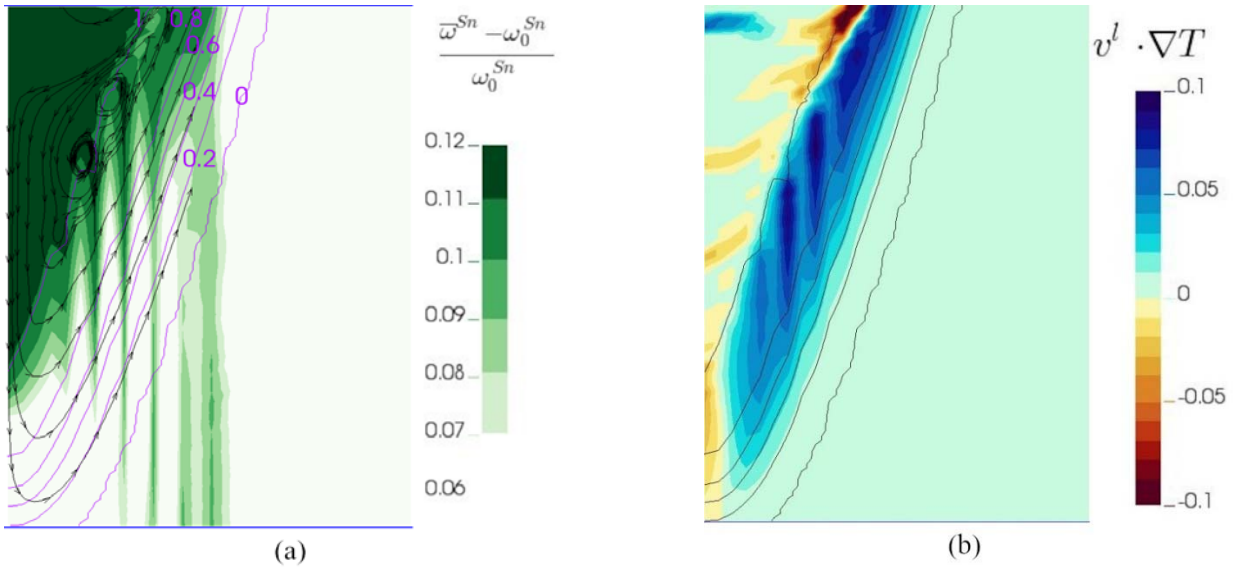

Fig. 11. Zoom visualization of the influence of solute-driven convection at time t_3 - continuous stirring, high azimuthal velocity. Case D - $\beta_T = 4 \cdot 10^{-5}\ °C^{-1}$, $\beta_S^{Sn} = 3 \cdot 10^{-2}\ wt\%^{-1}$. (a) Liquid fraction, streamlines and Sn content. (b) Liquid fraction and convective $v^l.\nabla T$ term.

In Fig. 12, the predicted radial Sn segregation profiles are plotted at two different heights and compared to experimental measurements. Those heights are representative for the alternated stirring ($h/H = 0.25$) and continuous stirring ($h/H = 0.75$) stages. Comparison of the simulation results with the experimental measurements confirms the importance of solutal convection in the mushy zone. At $h/H = 0.75$, the measured Sn concentration continuously increases in the inner part of the ingot until it reaches its maximum at $r/R = 0.5$. The simulated results show the same tendency only in case D, where solutal convection is opposed to thermal

481 one. Among the calculations, case D, where the solute coefficient $\beta_S^{Sn} = 3 \cdot 10^{-2}(wt\%)^{-1}$, has
482 the best fit to the measured data and was therefore chosen for subsequent simulations.

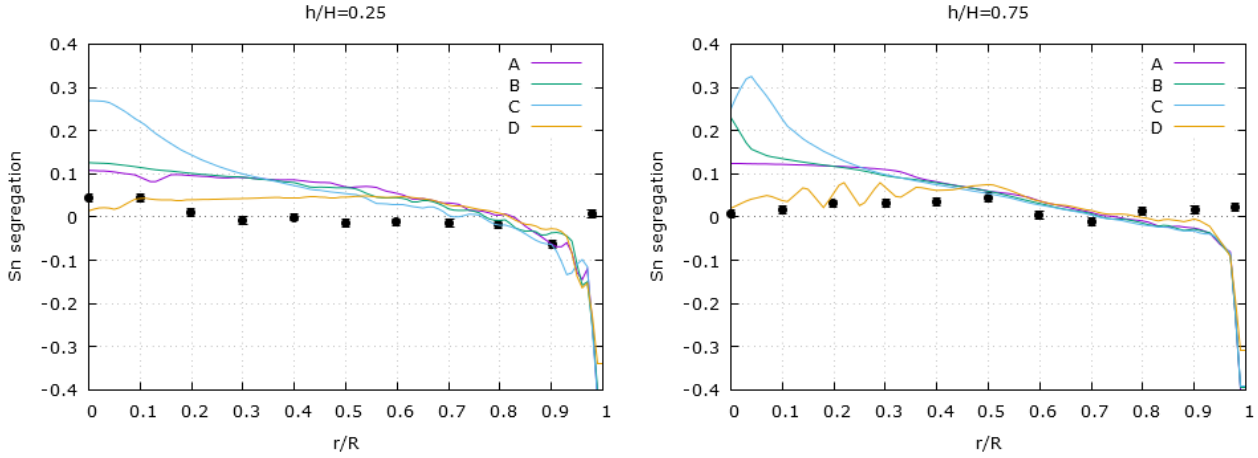

483 **Fig. 12**. Radial profiles of Sn segregation $(\overline{\omega}^{Sn} - \omega_0^{Sn})/\omega_0^{Sn}$ at 2 heights in the remelted ingot.
484 Experimental (•) and model (-) results. Letters A, B, C, D correspond to cases listed in Table 4.

485

486 The computed profiles of the radially averaged longitudinal Sn content are shown in
487 Fig. 13. Thermo-solutal convection has no significant effect on the overall longitudinal
488 segregation. Although the comparison of simulated results with experimental measurements
489 should be interpreted with caution, due to the limited number of measurements along the ingot
490 height, the results show a fairly good agreement.

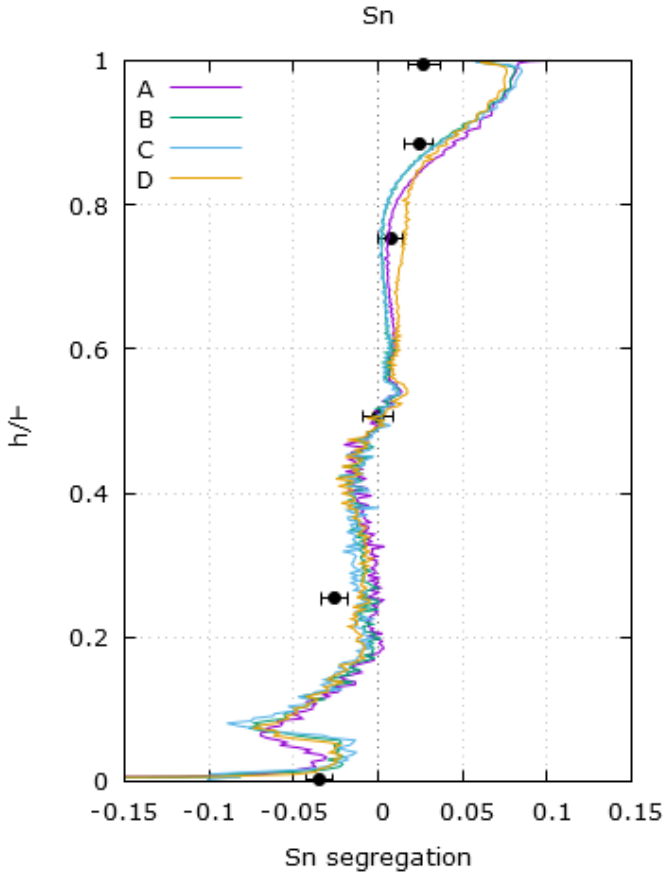

491 **Fig. 13.** Radially-averaged longitudinal profiles of Sn segregation $(\overline{\omega}^{Sn} - \omega_0^{Sn})/\omega_0^{Sn}$ in the
492 remelted ingot. Experimental (•) and model (-) results. Letters A, B, C, D correspond to cases
493 listed in Table 4.

494 For a given thermo-solutal convection (case D), Fig. 14 shows the longitudinal content
495 profiles for Sn and other alloying elements, namely Fe, O and Cr. The results for all elements are
496 quite similar (it must be stated that the oxygen partition coefficient k_O is larger than 1) and in
497 fairly good agreement with measurements, except in the bottom part of the ingot. At this location,
498 in addition to a possible effect of dendrite arm spacing (see section 4.2), it could be argued that
499 the discrepancy between the measured chemistry and the predicted segregation is related to the
500 motion of equiaxed grains. [7] showed that the sedimentation of free floating equiaxed grains can

501 significantly affect macrosegregation. Decantation of these grains in the bottom of the melt pool
502 during its solidification could balance the macrosegregation induced by thermo-solutal
503 convection, resulting in a flat segregation profile.

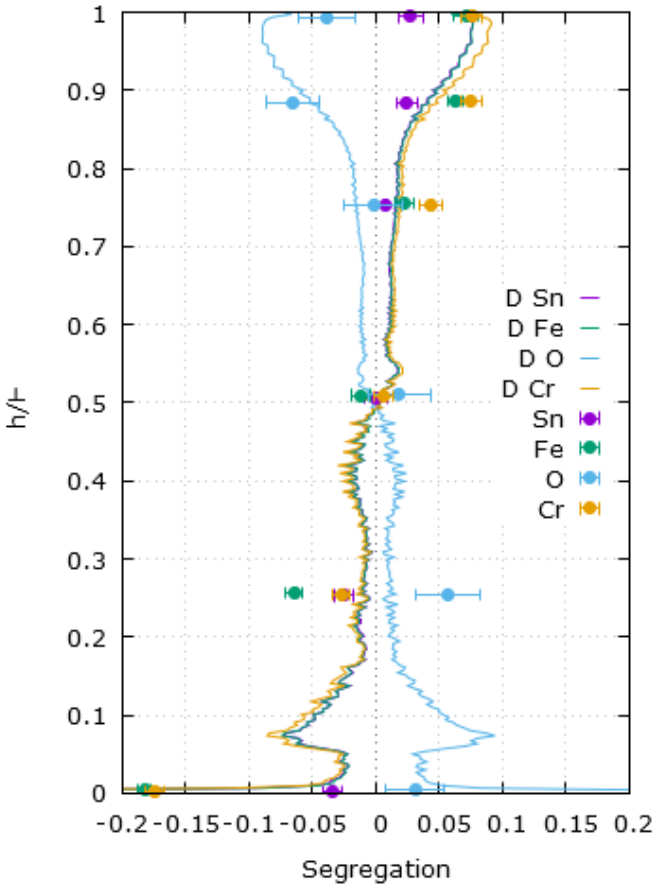

504 **Fig. 14**. Radially-averaged longitudinal profiles of chemical segregation $(\overline{\omega}^{n} - \omega_0^{n})/\omega_0^{n}$ in the
505 remelted ingot for elements Sn, Fe, O and Cr. Experimental (•) and model (-) results. Case D -
506 $\beta_T = 4 \cdot 10^{-5}\ °C^{-1}$, $\beta_S^{Sn} = 3 \cdot 10^{-2}\ wt\%^{-1}$.

507

508 **4.2.2. Influence of the dendrite arm spacing**

509 As discussed in section 3, the solidifying mushy zone is modelled as a porous medium
510 and is characterized by its local permeability which depends on the liquid volume fraction g_l and

511 the dendrite arm spacing λ_{DAS} (Eqs.13 and 17 in Table 1). Unfortunately, it is very difficult to
512 obtain a true value of λ_{DAS} from a conventional metallographic analysis due to the solid state
513 transformation $\beta(\mathrm{cc}) \rightarrow \alpha(\mathrm{hcp})$ that occurs during the cooling of Zirconium alloys. In order to
514 assess the role of the permeability in macrosegregation prediction, three cases were tested for
515 each of the solidification models and are presented in Table 5. The value
516 $\beta_S^{Sn} = 3 \cdot 10^{-2}(wt\%)^{-1}$ (corresponding to case D, see above) was adopted for all calculations.
517

518 **Table 5.** Definition of the three simulations run to study the effect of dendrite arm spacing.

case	λ_{DAS} [μm]	$K_0[\mathrm{m}^2]$
D'	67	$2.5 \cdot 10^{-11}$
D	134	10^{-10}
D''	268	$4 \cdot 10^{-10}$

519

520 The computed Sn macrosegregation maps are shown in Fig. 15. It can be observed that
521 the intensity of macrosegregation increases with λ_{DAS}. To explain this phenomenon, the
522 amplitude of the liquid velocity in the mushy zone during the continuous stirring stage (time t_3) is
523 plotted in Fig. 16 as a function of the liquid fraction. It is obvious that a large λ_{DAS} increases the
524 velocity of the interdendritic liquid flow, thus promoting macrosegregation.

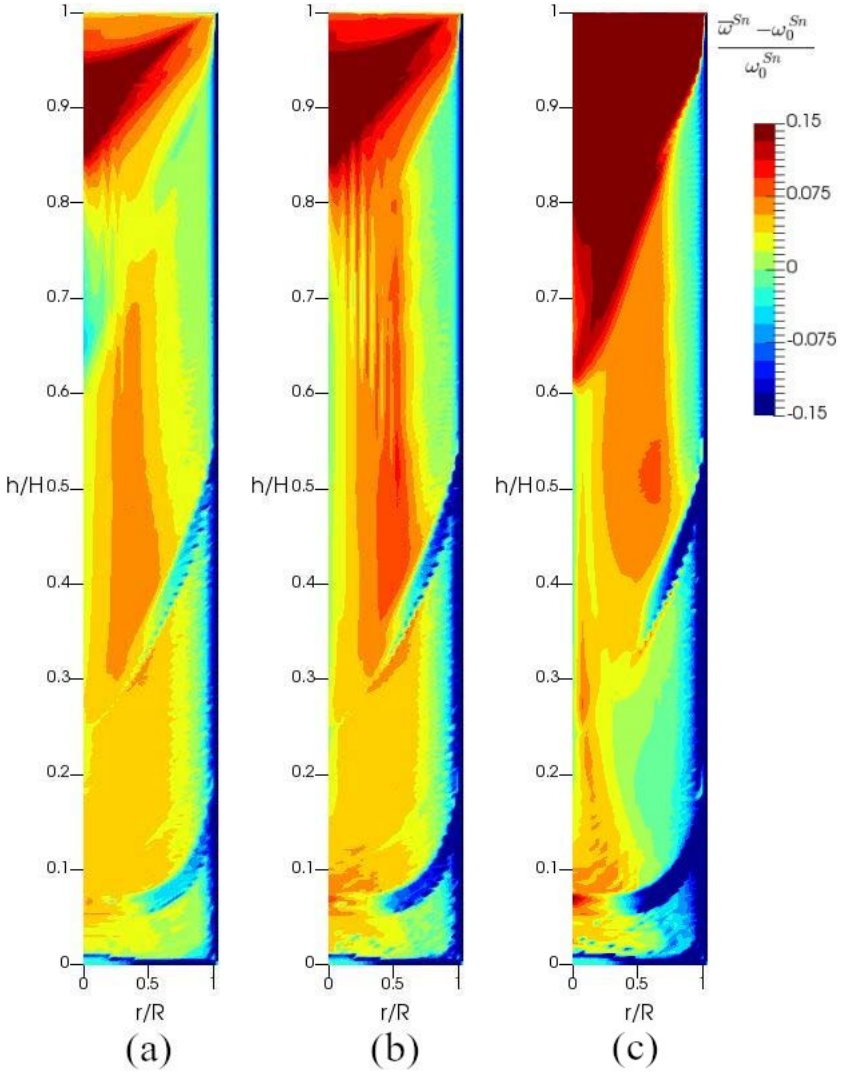

a) b) c)

525 **Fig. 15**. Influence of the dendrite arm spacing λ_{DAS} on the computed Sn macrosegregation map in
526 the remelted ingot. (a) Case D': $\lambda_{DAS} = 67$ µm. (b) Case D: $\lambda_{DAS} = 134$ µm. (c) Case D'':
527 $\lambda_{DAS} = 268$ µm.

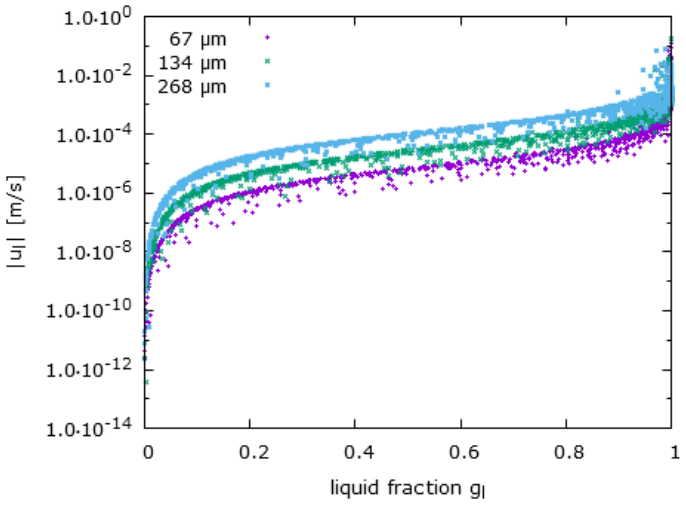

528

529 **Fig. 16**. Magnitude of the liquid velocity in the mushy zone as a function of liquid fraction at
530 time t3 (continuous stirring stage).

531 In Fig. 17, the simulated macrosegregation of Sn is compared to experimental
532 measurements at two different heights ($h/H = 0.25$) and ($h/H = 0.75$). The profiles calculated
533 for $\lambda_{DAS} = 67$ µm and $\lambda_{DAS} = 134$ µm are similar at $h/H = 0.25$. These profiles are quite flat
534 up to $r/R = 0.6$, after which point the Sn concentration gradually decreases. Although the
535 difference between the simulated results and the experimental measurements is not high, it should
536 be noted that the predicted segregation in the mid-radius zone is positive while the experimental
537 segregation is negative. The agreement is much better when λ_{DAS} is increased to 268 µm, because
538 the predictions for this case anticipate the negative Sn segregation values from $r/R = 0.5$ on. At
539 $h/H = 0.75$, on the contrary, a better agreement was found when λ_{DAS} was reduced (case D').

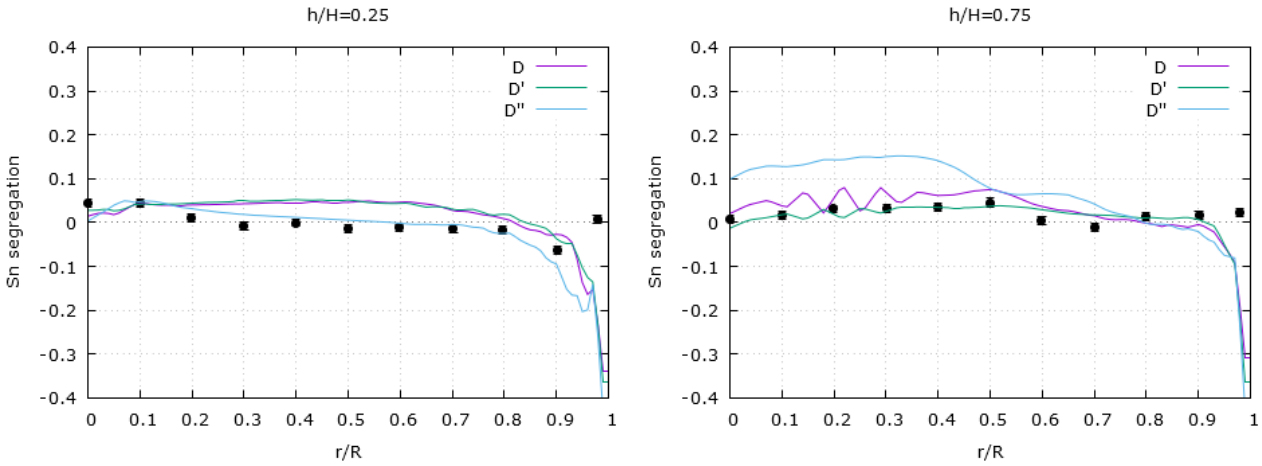

Fig. 17. Radial profiles of Sn segregation $(\overline{\omega}^{Sn} - \omega_0^{Sn})/\omega_0^{Sn}$ at 2 heights in the remelted ingot. Experimental (•) and model results. Letters D, D' and D'' correspond to cases listed in Table 5.

4.2.3. Influence of the grain growth kinetics

The effect of grain growth kinetics on macrosegregation was investigated numerically by examining four different cases listed in Table 6. The default values presented in Table 3 were used for the diffusion coefficients of alloy elements, thermal and solutal expansion coefficients, nucleat+ion density, and secondary dendrite arm spacing, unless otherwise specified. Case D, as usual, represents the case with default values. In case E, the nucleation density N_0 was increased to 10^{12} m^{-3}. In cases F and G, the diffusion coefficient of Sn in the solid phase was reduced to $4.9 \cdot 10^{-15}$ m^2/s for a nucleation density equal to 10^{12} m^{-3} and 10^{10} m^{-3}, respectively.

Table 6. Definition of the four simulations run to study the effect of grain growth kinetics

case	N_0 [m^{-3}]	D_S^{Sn}[m^2/s]

D	10^{10}	$4.9 \cdot 10^{-11}$
E	10^{12}	$4.9 \cdot 10^{-11}$
F	10^{12}	$4.9 \cdot 10^{-15}$
G	10^{10}	$4.9 \cdot 10^{-15}$

553

554 Fig. 18 shows the final macrosegregation maps of Sn computed in all four cases.
555 Although the solidification process differs quantitatively, the comparison of the maps reveals
556 only small differences in the calculated macrosegregation. As apparent from Fig. 18, nucleation
557 density and solute diffusivity did not seem to play an important role in the chemistry of the
558 remelted ingot. Nevertheless, it can be noted that the macrosegregation was slightly less intense
559 in case E.

560 The small differences observed between these different cases can be explained by
561 studying the value of the Fourier number in order to characterize the diffusion of solute in the
562 solid and liquid phases in the central part of the ingot. The Fourier number associated to a given
563 phase (solid or liquid) is defined as the ratio $o = \frac{D \cdot t_{ls}}{R_g^2}$. In this relationship, D is the solute
564 diffusion coefficient in the considered phase, t_s is the local solidification time, and R_g is the final
565 average grain radius as defined in equation (22) in Table 2. As it can be seen in this equation, the
566 final grain radius is only dependent of the grain density which is an input of the model. If the
567 value of the Fourier number is greater than 1 the composition profile of the alloying element can
568 be considered as uniform in the phase, while if it is smaller than 1 the composition profile is non
569 uniform. The values of the Fourier numbers for the liquid and solid phases are reported in Table 7
570 considering two local solidification times (t_{ls}), respectively 10 and 1260 s. The first value
571 corresponds to the solidification time at a point close to the skin while the second one stands for a

location in the central part of the ingot. These points have been chosen along a line at mid-height of the ingot. They are considered to be representative of extreme values of the Fourier numbers in the solid and liquid phases.

Table 7. Values of the Fourier number in the liquid and solid phases for the four cases (D, E, F, G). These Fourier numbers are estimated for two local solidification times (10 s and 1260 s). These values correspond to points located close to the skin of the ingot and for the second one to a point located at the center of the ingot. Both of them are considered at mid-height of the ingot.

	t_{ls} = 10 s		t_{ls} = 1260 s)	
	Fo_l^{Sn}	Fo_S^{Sn}	Fo_l^{Sn}	Fo_S^{Sn}
D	1.2	0.006	150	0.75
E	2.6	0.127	3270	16
F	2.6	10^{-5}	3270	0.0016
G	1.2	$6\ 10^{-7}$	150	$7.5\ 10^{-5}$

For the two points and all 4 cases, the Fourier number values in the liquid phase are greater than 1, thus the solute profile at the microscopic scale was uniform in the liquid phase during almost all the solidification. Considering the point close to the skin, the Fourier number in the solid phase is lower than 1 in all cases. This means that there is no diffusion of solute in the solid phase at the microscopic scale in all cases for the point close to the skin. The skin is thus a region for which all cases correspond to the same situation at the microscopic scale: perfect diffusion of solute in the liquid and no diffusion of solute in the solid. This is why the macrosegregation is very similar for all the cases in the region of the skin of the ingot.

Considering the point located at mid-height in the center of the ingot, for cases D, F and G, the Fourier number value in the solid phase is lower than 1 while it is greater than 1 for case E. These results show that for cases D, F and G, solidification proceeds in such a way that the solute diffuses perfectly in the liquid phase and very little in the solid phase. For case E, the diffusion of the solute is perfect in the solid and liquid phases. For all cases, the diffusion is perfect in the liquid phase, only the diffusion of the solute in the solid phase is different. It has already been shown that solute diffusion in the solid phase has very little influence on macrosegregation[29]. This can explain why cases D, E, F, G lead to similar macrosegregation.

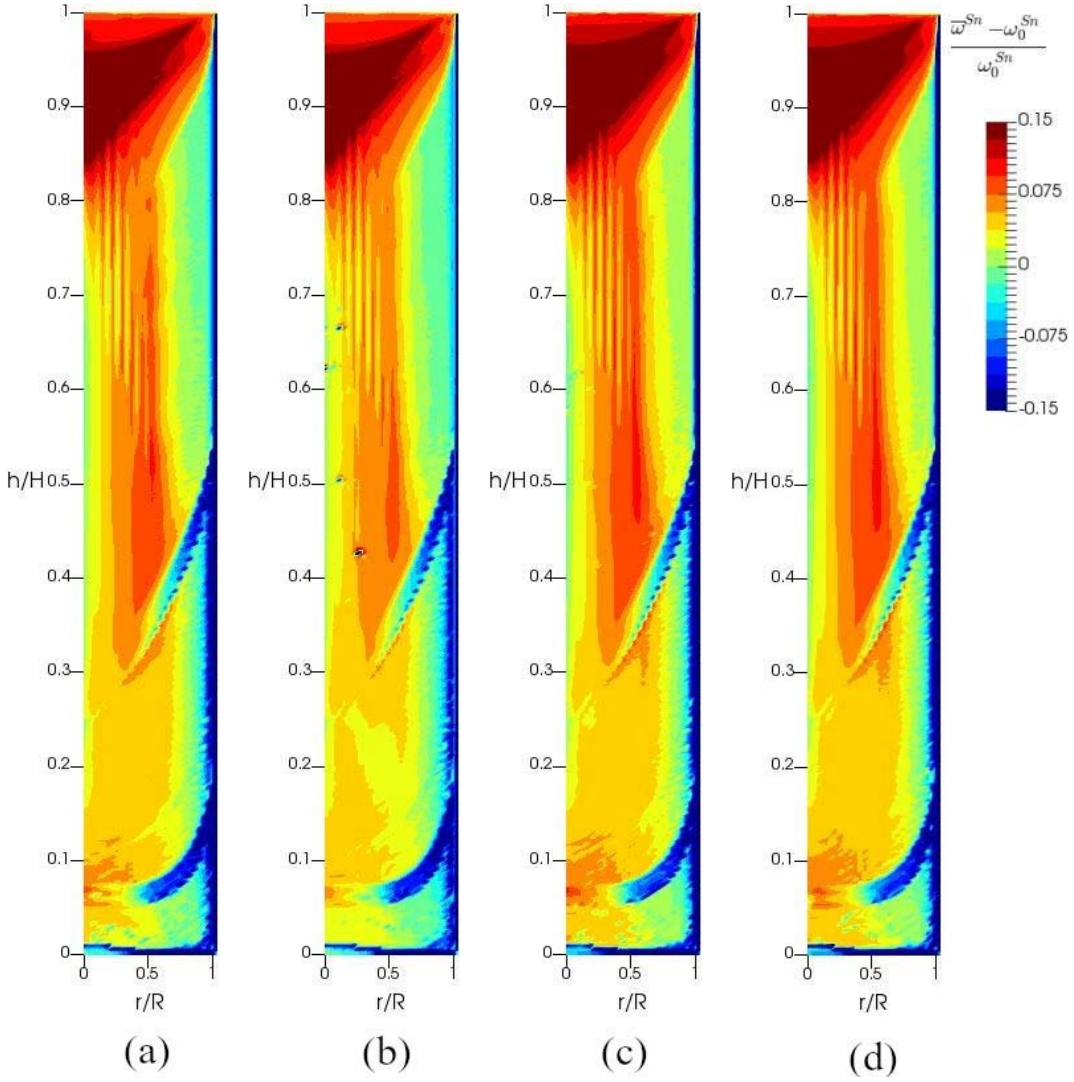

597 **Fig. 18**. Computed Sn content map in the remelted ingot, (a) case D, (b) case E, (c) case F and (d)
598 case G. Letters D, E, F, G correspond to cases listed in Table 6.

599

600 **5 Conclusions and prospects**

601 A two-scale model was used to simulate the solidification of the remelting of an
602 experimental chemically homogeneous Zy-4 electrode in a production furnace. The effects of
603 thermal and solutal convection on ingot macrosegregation, as well as the influence of dendrite
604 arm spacing (i.e. the permeability of the mushy region) were studied and analyzed. In addition,
605 the influence of grain growth kinetics was investigated numerically.

606 The results show that it is necessary to take into account the thermal and solutal buoyancy
607 forces in order to obtain an accurate simulation of hydrodynamics and consequently the
608 macrosegregation in VAR ingots. Comparing the experimental measurements with the simulated
609 results, it is concluded that solutal-driven convection may promote an upward flow along the
610 solidification front in the mushy zone and thus be partially responsible for macrosegregation in
611 the central part of the ingot. Furthermore, the simulations have shown that the macrosegregation
612 predicted by the model depends on the dendrite arm spacing value used to calculate local
613 permeability in the mushy zone. However, the model is still unable to predict some of the trends
614 observed in experimental measurements.

615 In future work, the transport of free-floating grains and the flow induced by the
616 solidification shrinkage will be implemented in the SOLAR code. Such additions could
617 significantly affect the predicted hydrodynamic behaviour, resulting in macrosegregation.

618

Acknowledgments

As a part of the OPERAS (Optimizing Processes based on Electrode Remelting with Arc or Slag) Project, this work has been partly supported by the French National Research Agency (ANR-08-MAPR-0006-04).

Conflict of interest

On behalf of all authors, the corresponding author states that there is no conflict of interest.

References

1 A. Jardy and D. Ablitzer: *Xiyou Jinshu Cailiao Yu GongchengRare Met. Mater. Eng.*, 2006, vol. 35, pp. 119–122.
2 A. Jardy and D. Ablitzer: *Mater. Sci. Technol.*, 2009, vol. 25, pp. 163–9.
3 A. Wilson and A. Jardy: in *A numerical study of the influence of stirring parameters on titanium ingot quality using SOLAR v4.2*, vol. 1, The Japan Institute of Metals, Kyoto, Japan, 2007.
4 V. Venkatesh, A. Wilson, M. Kamal, M. Thomas, and D. Lambert: *JOM*, 2009, vol. 61, pp. 45–50.
5 P. Chapelle, A. Jardy, J.P. Bellot, and M. Minvielle: *J. Mater. Sci.*, 2008, vol. 43, pp. 5734–46.
6 M. Revil-Baudard, A. Jardy, F. Leclerc, M. Zaloznik, V. Rebeyrolle, and H. Combeau: in *CFD Modeling and Simulation in Materials Processing*, John Wiley & Sons, Ltd, 2012, pp. 107–14.
7 H. Combeau, M. Založnik, S. Hans, and P.E. Richy: *Metall. Mater. Trans. B*, 2009, vol. 40, pp. 289–304.
8 B.E. Launder and D.B. Spalding: *Comput. Methods Appl. Mech. Eng.*, 1974, vol. 3, pp. 269–89.
9 P.J. Prescott and F.P. Incropera: *J. Heat Transf.*, 1995, vol. 117, pp. 716–24.
10 B.V. Antohe and J.L. Lage: *Int. J. Heat Mass Transf.*, 1997, vol. 40, pp. 3013–24.
11 A. Nakayama and F. Kuwahara: *J. Fluids Eng.*, 1999, vol. 121, pp. 427–33.
12 M.H.J. Pedras and M.J.S. de Lemos: *Int. J. Heat Mass Transf.*, 2001, vol. 44, pp. 1081–93.
13 S. Hans: PhD thesis (in French), Institut National Polytechnique de Lorraine, 1995.
14 T. Quatravaux: PhD thesis (in French), Institut National Polytechnique de Lorraine, 2004.
15 M. Revil-Baudard: PhD thesis (in French), Université de Lorraine, 2012.
16 C. Beckermann and R. Viskanta: *Physicochem. Hydrodyn.*, 1988, vol. 10, pp. 195–213.
17 C.Y. Wang and C. Beckermann: *Metall. Mater. Trans. A*, 1996, vol. 27, pp. 2754–64.
18 M. Založnik and H. Combeau: *Comput. Mater. Sci.*, 2010, vol. 48, pp. 1–10.
19 K. Tveito, M. Bedel, M. Založnik, H. Combeau, and M. M'Hamdi: vol. 27, IOP Publishing, 2012, p. 012040.
20 T.B. Massalski, H. Okamoto, P. Subramanian, L. Kacprzak, and W.W. Scott: *Binary Alloy Phase Diagrams*, vol. 1, American society for metals Metals Park, OH, 1986.
21 T. Quatravaux, S. Ryberon, S. Hans, A. Jardy, B. Lusson, P.E. Richy, and D. Ablitzer: *J. Mater. Sci.*, 2004, vol. 39, pp. 7183–91.
22 G. Ghazal, A. Jardy, P. Chapelle, and Y. Millet: *Metall. Mater. Trans. B*, 2010, vol. 41, pp. 646–59.

23 A. Jardy, F. Leclerc, M. Revil-Baudard, P. Guerin, H. Combeau, and V. Rebeyrolle: *J. ASTM Intern.*, DOI:10.1520/JAI102992.
24 M. Založnik and H. Combeau: *Int. J. Therm. Sci.*, 2010, vol. 49, pp. 1500–9.
25 P.-F. Paradis and W.-K. Rhim: *J. Mater. Res.*, 1999, vol. 14, pp. 3713–9.
26 T. Ishikawa and P.-F. Paradis: *J. Electron. Mater.*, 2005, vol. 34, pp. 1526–32.
27 M.J. Assael, A.E. Kalyva, K.D. Antoniadis, R. Michael Banish, I. Egry, J. Wu, E. Kaschnitz, and W.A. Wakeham: *J. Phys. Chem. Ref. Data*, 2010, vol. 39, p. 033105.
28 M. Revil-Baudard, A. Jardy, H. Combeau, F. Leclerc, and V. Rebeyrolle: *Metall. Mater. Trans. B*, 2014, vol. 45, pp. 51–7.
29 M.C. Schneider and C. Beckermann: *Int. J. Heat Mass Transf.*, 1995, vol. 38, pp. 3455–73.

List of figures

List of tables